AD NUMBER
ADB001011
NEW LIMITATION CHANGE

TO

Approved for public release, distribution unlimited

FROM

Distribution authorized to U.S. Gov't. agencies only; test and evaluation; Nov 1974. Other requests shall be referred to AFML/LPO, Wright-Patterson Air Force Base, Ohio 45433.

AUTHORITY

AFWAL notice, 3 Nov 1983

ADB001011

RESEARCH ON YB$_{66}$

FOR MICROWAVE ACOUSTIC CRYSTALS

FINAL TECHNICAL REPORT

Period Covered: 03 May 1971 through 30 June 1974

G.A. Slack, J.D. Young, W.S. Knapp,
D.W. Oliver, and G.D. Brower
Solid State and Electronics Laboratory
Corporate Research and Development
General Electric Company
Schenectady, New York 12301

AIR FORCE MATERIALS LABORATORY
AIR FORCE SYSTEMS COMMAND
WRIGHT-PATTERSON AIR FORCE BASE, OHIO   45433

November 1974   SRD-74-124

NOTICE

When Government drawings, specifications, or other data are used for any purpose other than in connection with a definitely related Government procurement operation, the United States Government thereby incurs no responsibility nor any obligation whatsoever; and the fact that the Government may have formulated, furnished, or in any way supplied the said drawings, specifications, or other data is not to be regarded by implication or otherwise as in any manner licensing the holder or any other person or corporation, or conveying any rights or permission to manufacture, use, or sell any patented invention that may in any way be related thereto.

This final report was submitted by the General Electric Research and Development Center, Schenectady, NY, under contract F33615-71-C-1531, job order number 73710322, with the Air Force Materials Laboratory, Wright-Patterson Air Force Base, Ohio.

This technical report has been reviewed and is approved for publication.

Copies of this report should not be returned unless return is required by security considerations, contractual obligations, or notice on a specific document.

AD_ *B001011*

AUTHORITY: *AFWAL Notice 3 Nov 83*

REPORT DOCUMENTATION PAGE		READ INSTRUCTIONS BEFORE COMPLETING FORM
1 REPORT NUMBER AFML-TR-74-253	2. GOVT ACCESSION NO.	3. RECIPIENT'S CATALOG NUMBER
4. TITLE *(and Subtitle)* RESEARCH ON YB₆₆ FOR MICROWAVE ACOUSTIC CRYSTALS		5. TYPE OF REPORT & PERIOD COVERED Final Technical Report 3 May 1971 - 30 June 1974
		6 PERFORMING ORG. REPORT NUMBER SRD-74-124
7. AUTHOR(s) G.A. Slack D.W. Oliver J.D. Young G.D. Brower W.S. Knapp		8. CONTRACT OR GRANT NUMBER(s) F33615-71-C-1531
9. PERFORMING ORGANIZATION NAME AND ADDRESS Corporate Research and Development General Electric Company Schenectady, New York		10. PROGRAM ELEMENT, PROJECT, TASK AREA & WORK UNIT NUMBERS P.E. 62102F Project/Task 7371/03 Work Unit 73710322
11. CONTROLLING OFFICE NAME AND ADDRESS U.S. Air Force Materials Laboratory Attn: AFML/LPO Wright-Patterson Air Force Base, Ohio 45433		12. REPORT DATE November 1974
		13. NUMBER OF PAGES 104
14. MONITORING AGENCY NAME & ADDRESS(if different from Controlling Office)		15. SECURITY CLASS. (of this report) Unclassified
		15a. DECLASSIFICATION/DOWNGRADING SCHEDULE

16. DISTRIBUTION STATEMENT *(of this Report)*

Distribution limited to U.S. Government agencies because Test and Evaluation data is included. November 1974. Other requests for this document should be referred to Air Force Materials Laboratory/LPO

17. DISTRIBUTION STATEMENT *(of the abstract entered in Block 20, if different from Report)*

D D C

JAN 17 1975

18. SUPPLEMENTARY NOTES

19. KEY WORDS *(Continue on reverse side if necessary and identify by block number)*

Bulk acoustic delay line
Spinel
Lithium Niobate
Yttrium boride

20. ABSTRACT *(Continue on reverse side if necessary and identify by block number)*

This report summarizes the results of three years of work on the problems of producing crystals and crystal plus transducer assemblies for long memory time, microwave ultrasonic delay lines. Information on sapphire, spinel, yttrium aluminum garnet, and yttrium boride is presented. At present, magnesium aluminate spinel appears to be the best available material for delay lines. It has low acoustic attenuation and low diffraction losses. Transverse acoustic waves are required in spinel in order to take advantage of its low-loss

DD FORM 1473   1 JAN 73   EDITION OF 1 NOV 65 IS OBSOLETE

characteristics. Shear mode transducers of X-cut lithium niobate are suitable for generating these waves. Calculations show that losses in the transducer-to-delay line bond can be held to a minimum by using an alloy of gold, paladium, and silver. This was not verified experimentally. The borides of yttrium are not suitable at present for delay lines because of problems with crystal growth and an anomalous acoustic attenuation that appears to be closely associated with the crystal chemistry.

TABLE OF CONTENTS

TABLE OF CONTENTS (Cont'd)

LIST OF ILLUSTRATIONS

iv

LIST OF ILLUSTRATIONS (Cont'd)

LIST OF TABLES

LIST OF TABLES (Cont'd)

Section 1

INTRODUCTION

Delay lines employing microwave frequency acoustic waves are being used in radar signal processing applications. These devices, however, have generally been found practical only for delay times up to a few tens of microseconds. The principal factor limiting the development of long memory time (milliseconds) applications has been the attenuation of the acoustic waves in the crystals used as the delay line media. In general this attenuation is substantially reduced at low temperatures, and thus longer delay time applications may become feasible if the additional cryogenic equipment can be justified. As advances in cryogenic equipment occur, tradeoff calculations for cryogenic delay lines in practical systems will have to be updated. Ambient temperature operation is always preferred, however, and is imperative in most cases. It has been the objective, therefore, of a continuing program at the General Electric Research and Development Center, supported by U. S. Air Force contracts, to develop crystals with low microwave acoustic attenuation at ambient temperature.

Throughout the prior work at General Electric emphasis has been given to a systematic approach to the development of useful crystals. Very briefly, the theory of microwave frequency sound attenuation was put in a form which permitted correlation of attenuation data near room temperature for various crystals, making it possible to define a figure of merit for candidate crystals. The value of this figure of merit could then be calculated from known properties or from the results of relatively simple thermal measurements. The figure of merit is applicable in the high temperature regime, including room temperature, where the attenuation is caused by the scattering of sound waves by thermal phonons. Theory also exists for the temperature region in which a rapid falloff in attenuation occurs. This theory can be put in a form which will provide a figure of merit for materials at cryogenic temperatures. At very low temperatures, observed sound attenuation is dominated by scattering due to crystal imperfections of various kinds. In highly perfect specimens the attenuation can be very small at sufficiently low temperatures, and is determined mainly by diffraction losses.

Many crystal systems have been investigated, both as potential practical materials and to verify the figure of merit theory. The lowest known room temperature attenuation coefficients which have been reliably measured are for shear waves in $MgAl_2O_4$ (spinel) and $Y_3 Al_5 O_{12}$ (garnet), and for longitudinal waves in β-rhombohedral boron and Al_2O_3 (sapphire). At present, delay lines are constructed principally from sapphire, using longitudinal acoustic waves, or from spinel, using shear waves.

The need for broad bandwidth in delay lines does not significantly limit the choice of crystal media because sound dispersion is negligible in the fre-

quency range of interest for almost all crystals. Bandwidth enters most importantly in the design of transducers and the transducer coupling circuits. The transducer design, electrode materials, and the coupling circuits also have very important effects on the performance of delay lines made from materials such as spinel. Shear mode transducers require improvements in the electrode materials used, in the types of bonds employed with bonded crystal plates, and in reproducible fabrication of deposited thin film transducers.

In Section 2 of this report, "Design of Delay Lines," the practical design is discussed thoroughly. The treatment includes those factors which are under the designers control: attenuation in transducer, electrodes, and propagating medium; transducer efficiency and bandwidth; diffraction of the acoustic wave; and beam steering due to elastic anisotropy. The results give appropriate criteria for transducer design, show the effects of transducer design upon performance, and show the relative performance capabilities for sapphire, yttrium aluminum garnet, and spinel. The calculations give a reasonable upper limit to performance, since such factors as crystalline imperfections and the limits of polishing and fabrication methods cannot be predicted theoretically.

The implications of matched filtering by means of silicon clocked analog delay devices (bucket brigade or charge coupled devices) and surface acoustic wave devices are examined and related to the capabilities of silicon clocked analog delay (CLAD) devices, passive surface acoustic wave (SAW) delay lines, and bulk acoustic wave delay lines used as memory elements. With this information as a background, the effect of acoustic impedance mismatch between delay line and transducer is examined. The problem is treated as a multipath problem in a form applicable to arbitrary coding of the input signal which is to be stored in the delay line. Simple criteria are developed to describe the effects of acoustic impedance mismatch on both the coded signal and the matched filter output for that signal.

In Section 3, "Delay Line Fabrication," particular attention is paid to the problem of attaching piezoelectric crystals to delay line crystals by means of an intermediate metallic bond. The properties of such bonds are discussed and those metals appropriate to spinel and lithium niobate are indicated. A scheme for fabricating these bonds has been developed, and methods and equipment for the subsequent thinning of the transducer crystals are discussed.

In Section 4, "Growth and Characterization," the whole development of YB_{66} crystals for delay lines is discussed. Particular attention is paid to crystal purity, stoichiometry, and perfection. Stoichiometric crystals appear to have a composition of YB_{66}, while the congruent melting composition is $YB_{61.7}$. Material with low acoustic loss may be YB_{34}. This knowledge combined with acoustic loss measurements on actual samples shows that, at present, these crystals are not suitable for low loss delay lines.

In Section 5, "Iron Doped Spinel Crystals," synthetic crystals of iron doped spinel are analyzed for their suitability for delay lines. In Section 6,

2

"Sound Attenuation and Diffraction Loss," measurements of acoustic attenuation at low temperature and low frequency are compared with the calculated diffraction loss. Good agreement is found.

Section 2

DESIGN OF DELAY LINES

A. BACKGROUND

In this section the design of acoustic delay lines for long reverberation times is considered. Delay time is limited by material choice. Calculations are made here for practical delay devices in order to establish which combinations of transducer, electrode material, and delay medium will provide the longest delay time and the longest delay time-bandwidth product. The calculations include the major factors which affect delay time: attenuation in the delay medium, attenuation in the metal electrodes, conversion of acoustic energy to electrical energy by the transducer, diffraction, and acoustic beam steering due to the elastic anisotropy of a crystal medium. The calculations are a performance upper limit in the sense that a number of small and unpredictable effects (nonparallelism of end surfaces, surface damage from polishing, internal strain due to crystal growth, local imperfections) are not included in the calculations. The results for sapphire, however, correspond reasonably well with experiment. It is shown that other materials, particularly $MgAl_2O_4$ spinel, can provide substantial improvement in performance over Al_2O_3.

Attenuation in the electrodes and the delay medium increases quadratically with frequency, and diffraction losses vary inversely with frequency. At low frequencies delay time is limited by diffraction; at high frequencies, by attenuation. Delay time and delay-time bandwidth product each go through a maximum at intermediate frequencies. For delay line approximately 3/8 of an inch in diameter these maxima occur between 200 MHz and 1 GHz. The bandwidth of the devices is approximately one-half the operating frequency, or from 100 MHz to 500 MHz in the 0.2 to 1.0 GHz range. Since these bandwidths are adequate for most applications and signals can be readily heterodyned to this frequency range, calculations have been carried out in the frequency interval of 0.2 to 1.0 GHz. Delay times can be increased by considering delay lines of larger diameter, but the improvement comes at lower frequencies, where diffraction limits the delay time. At the delay time maximum, the operating frequency is proportional to $D^{-1/2}$ and the maximum delay time is proportional to $D^{9/8}$ where D is the transducer diameter.

To calculate a delay time, assumptions must be made about the initial signal level and receiver sensitivity. These assumptions do not affect the relative performance of delay lines fabricated from different combinations of materials. The relative performance shown by these calculations will be valid for a variety of applications. To show the magnitude of delay which may be expected, a set of typical system parameters -- drive power, receiver sen-

5

sitivity, interpulse period -- were chosen. The total delay time in a specific application will differ from these calculated values if the system parameters are different. That is, this calculation gives the relative performance under a variety of system parameters and several delay line material combinations, but the calculated total delay times are typical values valid for a specific set of system parameters. A simple system will be assumed, with an input of +40 dBm (10 watts peak) into the delay line and a low-noise amplifier on the output with a sensitivity of -70 dBm. The system thus has a dynamic range of 110 dB with a good signal-to-noise ratio which will remain constant for all cases discussed. Three delay line configurations will be analyzed: the double-end (DE) delay line, with transducers on both input and output; the single-end (SE) delay line, which requires a circulator; and the switched impedance delay line, which requires an electronic switch and two impedance transformers. The delay line materials will be the lowest loss materials known that are readily available in large size -- longitudinal propagation in sapphire (Al_2O_3) and shear propagation in YAG ($Y_3Al_8O_{12}$) and spinel ($MgAl_2O_4$).

The transducer thickness in the frequency range 0.2 to 1 GHz varies from 5 to 11 μm, depending on the transducer material used. Either bonded plate transducers, thinned after bonding, or deposited transducers can be used. The low loss acoustic modes are shear waves and require shear transducers. New bonding methods are required for the use of bonded plate transducers with low acoustic loss metals for electrodes. Deposited shear mode transducers have never been deposited reproducibly. Transducer development will be required in implementing long delay time devices with either type of transducer.

The properties of transducer materials, electrode materials, and delay line materials needed for the loss calculations are listed in the following subsection. Next, the expression for the total loss in a reverberating delay line is derived, as well as the basic equations necessary to calculate the acoustic conversion loss, the electrode loss, the material loss, and the acoustic diffraction loss. A series of graphs compares the total delay time versus insertion loss (IL) and frequency and the IL versus frequency for several delay line configurations and materials.

B. TRANSDUCER, ELECTRODE, AND DELAY MEDIA PROPERTIES

The material properties of transducers, electrode, and propagation media needed to calculate the acoustic loss are listed in Tables 1 through 3.

The data in Table 1 are from Reeder and Winslow (Ref. 1). All these materials can be cut into thin transducer plates. The longitudinal mode ZnO transducer can also be sputtered with reduced coupling coefficient k_t = 0.22 to 0.25.

All the data in Table 2 were experimentally determined by Larson and Winslow (Ref. 2) by fitting parameters to insertion loss versus frequency data for delay lines, using thin films of these metals as electrodes. The propagation

6

Table 1

PROPERTIES OF TRANSDUCER MATERIALS

Material	Cut	Mode	Coupling Coefficient k	Dielectric Constant ϵ_r	Velocity V_1 (10^5 cm/sec)	Acoustic Impedance Z_1 (10^5 g/s cm²)
Quartz, SiO_2	Y	Shear	$k_{12} = 0.14$	4.5	3.80	10.1
Cadmium sulfide, CdS	Z	Long	$k_t = 0.15$	9.5	4.46	21.5
Zinc oxide, ZnO	Z	Long	$k_t = 0.28$	8.8	6.33	36.0
Zinc oxide, ZnO	X	Shear	$k_{15} = 0.32$	8.3	2.72	15.5
Lithium niobate, $LiNbO_3$	X	Shear	$k = 0.68$	44.0	4.80	22.6

Table 2

PROPERTIES OF ELECTRODE MATERIALS

Material	Propagation Direction	Mode	V_s (10^5 cm/sec)	Acoustic Impedance Z_s (10^5 g/s cm²)	Attenuation dB/cm at 1 GHz
Indium	[101]	Long.	2.25	16.4	80,000
Indium	[101]	Shear	0.91	6.4	60,000
Silver	[111]	Long.	3.96	41.5	250
Silver	[111]	Shear	1.56	16.5	--
Gold	[111]	Long.	3.40	65.5	200
Gold	[111]	Shear	0.93	17.4	1,000

Table 3

PROPERTIES OF DELAY MEDIA

Material	Propagation Direction	Mode	Velocity V_D (10^5 cm/sec)	Acoustic Impedance Z (10^5 g/s cm²)	Attenuation (dB/μs at 1 GHz)
Sapphire Al_2O_3	Z	Long.	11.1	44.3	0.2
YAG $Y_3Al_5O_{12}$	[100]	Shear	5.03	22.9	0.09
Spinel $MgAl_2O_4$	[100]	Shear	6.54	23.4	0.04

directions listed are the orientations usually obtained with vapor-deposited metal films. The velocities are slightly different from the values published for bulk materials. The attenuation values are normalized to 1 GHz and have a frequency squared dependence; thus the attenuation values listed at 1 GHz will be reduced by a factor of 25 at a frequency of 200 MHz. The shear attenuation values are always higher than the longitudinal attenuation values. Indium is not a good bond material for reverberating delay lines because of its excessively high loss. Delay line performance is calculated for devices made with gold electrodes and for delay lines in which the attenuation in the

electrode is negligible. These calculations will show the desirability of re-
placing gold with a lower loss metal in the case of the best combination of trans-
ducers and delay media.

The attenuation values listed in Table 3 are taken from the authors' acous-
tic attenuation measurements and those in the literature at 1 GHz. The at-
tenuation constants for these materials are proportional to frequency squared
over the range of measurement of 10 GHz to 500 MHz. From 500 MHz to 200
MHz the attenuation values are extrapolated with the quadratic frequency de-
pendence. The three materials considered have the lowest known losses for
commercially available crystals prepared in large size. The attenuation data
for spinel were obtained on small flux grown samples. Large, high-quality
Czochralski boules are now available, but it has not yet been shown that this
material has the perfection required for low acoustic losses.

C. TOTAL ACOUSTIC LOSS

The delay time of a delay line is determined by the loss characteristics
of the line and the dynamic range of the system in which it is used.

Dynamic Range = Transducer Insertion Loss (loss in converting input
electrical signal into acoustic energy and back into
an electrical signal)

+

Acoustic Conversion Loss (acoustic energy converted
to an electrical signal every time the acoustic pulse
strikes the transducer)

+

Electrode Attenuation (acoustic energy loss in the metal
electrodes)

+

Propagation Medium Attenuation

+

Diffraction Loss (diffraction causes the acoustic pulse
to spread in size as it propagates; thus a decreasing
fraction of it strikes the transducer)

If the transducer is made 100 percent efficient in converting the in-
put energy into acoustic energy, insertion loss = 0; if it is not electrically

8

switched to change its efficiency, then the first acoustic "echo" to strike the transducer is completely converted back to an electrical signal and the total delay time is very small. If the transducer is made very inefficient the acoustic conversion loss will be small and very little of the acoustic energy will be converted to electrical energy by the transducer; however, very little acoustic energy will be obtained from the input electrical signal and total delay time will suffer. A broad optimum of the insertion loss exists, so that a balance is struck between converting the initial electrical signal to acoustic energy and the conversio of acoustic energy when the acoustic pulse strikes the transducer. In the calculations which follow, the optimum insertion loss is found, and the total delay time is then calculated from the dynamic range of the system, the insertion loss value, and the attenuation and diffraction constants of the materials used in the delay line.

The origin of these losses will become apparent as the DE delay line shown in Figure 1 is analyzed.
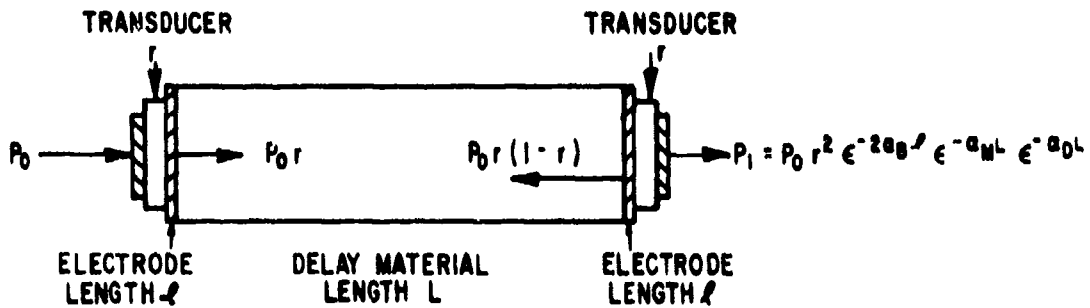
Figure 1. Output Power of the First Reflection of a DE Delay Line

Assume an electrical input power to the transducer P_0. The transducer converts a fraction r of P_0 into acoustic power, which propagates through the delay material. At the second transducer a fraction r of $P_0 r$ is converted to electrical power and (1-r) of $P_0 r$ is reflected.

The electrical power output at the first reflection, P_1, is $P_0 r^2$ exp $(-2\alpha_B \ell - \alpha_M L - \alpha_D L)$, where $2\alpha_B \ell$ is the acoustic loss of two passes through the electrodes, $\alpha_M L$ is the acoustic propagation loss through the delay material, and $\alpha_D L$ is the acoustic diffraction loss. The next series of reflections is shown in Figure 2.
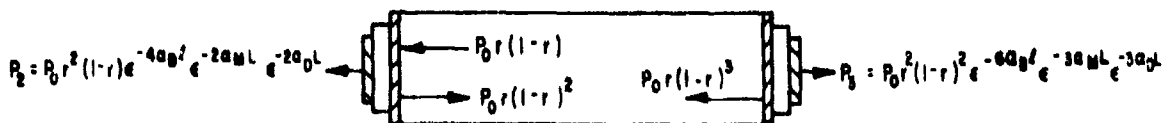
Figure 2. Output Power of the Second and Third Reflections
of a DE Delay Line

The general expression for the Nth reflection can be written and the terms identified:

$$P_0 r^2 (1-r)^{N-1} \exp(-2N\alpha_e \ell -N\alpha_M L - N\alpha_D L) = P_N \quad (N=1,2,3,\dots) \qquad (1)$$

The r^2 term is the transducer insertion loss $IL = 10 \log_{10} r^2$ (dB); the $(1-r)^{N-1}$ term is the acoustic conversion loss due to the transducer, Γ_t; and the three exponential terms are the electrode loss Γ_E, the material loss Γ_M, and the diffraction loss Γ_D. The calculation procedure is now straightforward; assumed values for IL will be subtracted from the constant dynamic range (110 dB), and the result will be called the available power. All the loss terms will be calculated on a decibel per reflection basis and summed. This number will be divided into the available power to calculate the total number of reflections and then multiplied by the travel time per reflection to give the total delay time. Since loss will be calculated for a large number of reflections (N = 100 to 1000), the $(1-r)$ loss will be included in the first reflection and the calculation will be slightly on the conservative side because $(1-r)^N$ is being used rather than the $(1-r)^{N-1}$ in Equation 1. The total acoustic loss in a SE delay line is similar to Equation 1 with one important difference (see Figure 3).

TRANSDUCER

ELECTRODE
LENGTH ℓ

DELAY MATERIAL
LENGTH L

$$P_1 = P_0 r^2 \epsilon^{-2\alpha_e \ell} \epsilon^{-2\alpha_M L} \epsilon^{-2\alpha_D L}$$

$$P_2 = P_0 r^2 (1-r) \epsilon^{-4\alpha_e \ell} \epsilon^{-4\alpha_M L} \epsilon^{-4\alpha_D L}$$
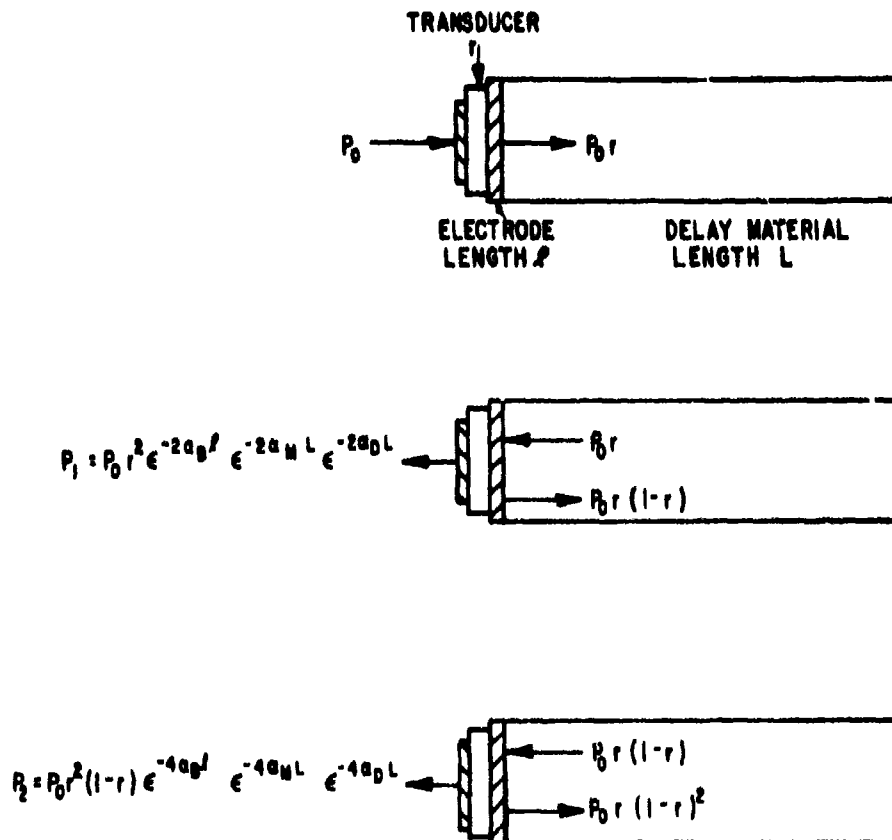
Figure 3. Output Power of the First and Second Reflections
of a SE Delay Line

10

The general expression for the Nth reflection of a SE delay line is:

$$P_0 r^2 (1-r)^{N-1} \exp(-2N\alpha_s \ell - 2N\alpha_M L - 2N\alpha_D L) = P_N \quad (N = 1, 2, 3 \ldots) \qquad (2)$$

The SE and DE cases must be compared at the same delay time: N detected echos and 2N, respectively. The material loss and the diffraction loss are the same. However, since the number of reflections is less than in the DE case the acoustic conversion loss and the electrode loss are reduced in the SE line. Thus, as will be seen later, the number of reflections for the SE case is always greater than one-half the reflections for the DE case, and hence the total delay time is greater for the SE delay line. Notice the way in which the reflections are counted: a reflection is counted every time it passes through a transducer. This must be done in the DE case because the even-numbered transducers have acoustic conversion loss and electrode loss even though only the odd-numbered reflections are read out. All reflections are read out in the SE case.

In the electrically switched SE delay line configuration, the driving resistance is switched from a low value with an efficient transducer conversion fraction of r_1 to a high value with an inefficient transducer conversion fraction of r_2 for readout. The general expression for the Nth reflection is:

$$P_0 r_1 r_2 (1-r_2)^{N-1} \exp(-2N\alpha_s \ell - 2N\alpha_M L - 2N\alpha_D L) = P_N \quad (N = 1, 2, 3 \ldots) \qquad (3)$$

The advantage of the switched configuration is that the input electrical pulse is efficiently converted to acoustic power but the transducer is then switched so that it abstracts little power from the acoustic pulse each time it strikes the transducer. Thus there is more available power to compensate for the acoustic conversion, electrode, material, and diffraction losses.

D. BASIC LOSS EQUATIONS

The basic equations necessary to calculate the insertion loss, acoustic conversion loss, electrode loss, material loss, and diffraction loss will now be derived.

Insertion Loss

In pulse-echo measurements transducer IL is defined as the ratio of output electric power (P_1) to the input electrical power (P_0) in the absence of attenuation and diffraction losses (see Figure 1). Thus IL is:

$$IL = 10 \log \frac{P_1}{P_0} = 10 \log r^2$$

with corrections for electrode loss, material loss, and diffraction of the first acoustic echo. The IL is then

$$IL = 20 \log r \text{ decibels} \qquad (4)$$

11

Equation 4 will be used to calculate r for assumed values of IL.

Acoustic Conversion Loss

The method of DeKlerk (Ref. 3) will be followed in calculating the acoustic conversion loss, which depends on the electromechanical coupling coefficient of the transducer. This acoustic conversion loss is the ratio of the reflected power to the incident power either on the electrical side of the transducer or the acoustic side. Referring to Figure 1, this ratio is $P_0(1-r)/P_0$ for the electrical side or $P_0 r(1-r)/P_0 r$ for the acoustic side. Since this loss occurs at every reflection, the acoustic conversion loss per reflection is

$$\Gamma_t = 10 \ \log(1-r) \ \text{dB/reflection} \tag{5}$$

Acoustic Electrode Loss

The electrode losses are calculated from the measured attenuation constants at 1 GHz with a frequency-squared frequency dependence (see values in Table 2). The electrode attenuation constant is:

$$\alpha_s = A \left(\frac{f}{1000}\right)^2 \ \text{dB/cm}$$

where

A = 200 dB/cm for longitudinal propagation through a gold electrode
  = 1000 dB/cm for shear propagation through a gold electrode
f = frequency (MHz)

Since the electrode losses are high, particularly for shear waves, only 1-μm-thick gold electrodes will be considered. There are two passes through the electrode per reflection; hence the acoustic electrode loss per reflection is

$$\Gamma_s = 2 \times 10^{-4} \times A \left(\frac{f}{1000}\right)^2 \ \text{dB/reflection} \tag{6}$$

Acoustic Material Loss

The material loss is calculated in a manner similar to that used for the electrode loss. Thus the material loss per reflection is

$$\Gamma_M = \tau \times B \left(\frac{f}{1000}\right)^2 \ \text{dB/reflection} \tag{7}$$

where

τ = travel time per reflection (L/V_0 for DE delay lines; 2L/V_0 for SE delay lines)
B = attenuation constant (dB/μsec) from Table 3
f = frequency (MHz)

12

Acoustic Diffraction Loss

Acoustic diffraction loss occurs because the cross-sectional area of the acoustic beam does not remain collimated for long travel distances but spreads out, becoming larger than the receiving transducer, and this represents an acoustic energy loss. This loss is difficult to calculate. Until recently authors (Ref. 4) considered only diffraction from circular-piston pressure sources radiating into fluid or elastic isotropic half-spaces. Papadakis (Ref. 5) extended this work to include longitudinal wave propagation in anisotropic materials. To the best of the authors' knowledge, no one has yet calculated diffraction of shear waves in anisotropic materials. Papadakis' results will be used here to estimate the diffraction loss for shear waves.

The calculation of diffraction for longitudinal wave in anisotropic materials is done in two steps: 1) finding the pressure and phase profiles at several distances from the input transducer, and 2) finding the response of the receiver to these profiles. Papadakis shows that the pressure at any point from the input transducer is given by

$$ P = \frac{j\omega\rho V_b}{2} \int_\sigma \frac{\exp j \{\omega t - \beta_0 |R|[1+b(1-2b)\,\theta^2]\}\, d\sigma}{|R|} $$

where

ω = angular frequency of the acoustic wave

ρ = density of the delay medium

V_b = velocity along the direction of propagation

β_0 = propagation vector which makes an angle with the transducer normal N

R = a vector lying along the Poynting vector of acoustic energy flux

σ = area of the transducer

b = a coefficient which measures the elastic anisotropy of the material

The second integration is performed over the receiver area σ', using the radial coordinate on the receiving transducer p'. Because the receiver is a pressure- and phase-sensitive detector its signal is proportional to the maximum over one cycle of the integral

$$ P_M = \int_{\sigma'} C(p')\cos[t-\delta(p')]d\sigma' \Big|_{max} $$

where $C(p')$ and $\delta(p')$ are the amplitude and phase of the pressure profile given above. The diffraction loss is then computed from

$$ dB = 20 \log (|P_{M'}| / |P_M|) $$

13

where P_M' is the pressure at some initial location. Papadakis has calculated the diffraction loss in terms of normalized distance S so that the data for all wave lengths and transducer radii (r) can be reduced to one curve for any given anisotropy. His curves for b = -1.0 to b = 0.4 are shown in Figure 4. The diffraction loss curves are all similar in shape for different values of b. The loss fluctuates with peaks (A = peak) and valleys in the Fresnel region before monotonically increasing for large values of normalized distance S. The diffraction loss will be calculated from the slope of these curves for large values of S. The magnitude of the diffraction loss is a strong function of material anisotropy factor b. To minimize the diffraction loss the value of b should be positive (0 to 0.4), because these curves have the minimum slope.
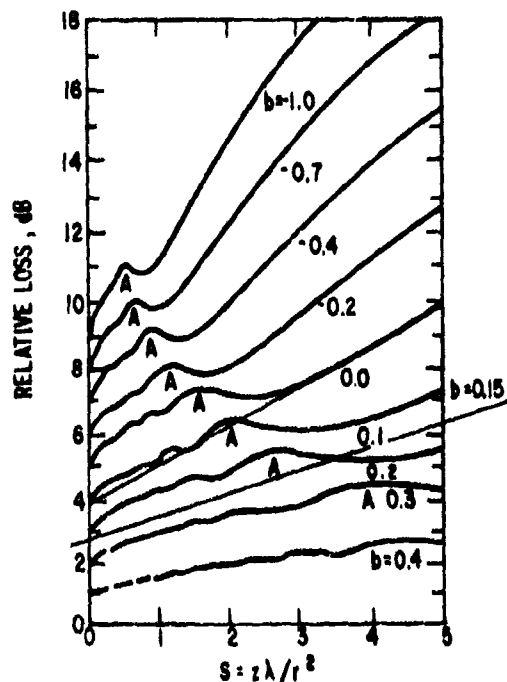
Figure 4. Acoustic Diffraction Loss Versus Normalized Distance
for Values of Anisotropy Parameter b

The b paramater is calculated from

$$b = -\frac{\Delta V}{V\theta^2}$$

where V is the velocity of the propagating acoustic wave and θ is the angle between the propagation vector β and the transducer normal N. If b is negative, the energy propagation vector R_v (Poynting vector) makes a larger angle with the transducer normal than does the propagation vector. The acoustic energy surface spreads more rapidly than does the phase surface, the acoustic beam spreading is greater, and the diffraction loss is higher. If b = 0, the material is elastically isotropic and vectors β, R, and N are colinear.

14

If b is positive, vector R lies between vector β and the transducer normal N, the acoustic energy is focused toward the transducer normal direction, and beam spreading and hence diffraction loss is reduced. In surface wave devices this effect has been called beam steering. Papadakis has shown that physical reasons exist (Ref. 6) to limit b to less than 0.5.

The b parameter is calculated from $\Delta V/V$, which can be written in terms of the elastic constants of the delay material. Papadakis has calculated b for longitudinal propagation along the threefold axis for trigonal crystals (Z propagation in Al_2O_3) as

$$b = \frac{(C_{33}-C_{13}-2C_{44})(C_{33}+C_{13})}{2C_{33}(C_{33}-C_{44})} \tag{8}$$

where $C_{13} = 1130$, $C_{33} = 4902$, and $C_{44} = 1454$ for Al_2O_3. Using these values, b is calculated for Al_2O_3 as $b = 0.154$. Since no one has calculated the acoustic diffraction for shear waves, the diffraction loss will be estimated by calculating the b parameter from the $\Delta V/V$ for shear waves given by Waterman (Ref. 7) and the diffraction loss curves shown in Figure 4. In this case the beam spreading is not conical, and a complete numerical calculation would have to include asymmetric diffraction with N, R, and β no longer coplanar. For shear waves along the [100] in cubic materials ($MgAl_2O_4$ and YAG) the shear waves are degenerate with a velocity $(C_{44}/\rho)^{1/2}$. The three vectors β, R, and N are not coplanar but depend on the angles θ and φ (Ref. 7). The b parameter in terms of elastic constants is

$$b(\phi) = \frac{-K_1}{4C_{44}} \left\{ K_2 \pm [K_2^2 - \sin^2 2\phi\,(2K_2-1)]^{1/2} \right\} \tag{9}$$

where

$$K_1 = C_{11} - C_{12} - 2C_{44}$$

$$K_2 = \frac{K_1}{C_{44}-C_{11}} + 2$$

For $MgAl_2O_4$, $C_{11} = 2.79$, $C_{12} = 1.53$, $C_{44} = 1.53$; for YAG, $C_{11} = 3.33$, $C_{12} = 1.11$, $C_{44} = 1.15$. Since the angle φ is not specified, b was calculated for $\sin^2 2\varphi = 0$ and $\sin^2 2\varphi = 1$ and the results were averaged. Equation 9 gives two values of b. Using the elastic constants for $MgAl_2O_4$, $b = 2.02$ and $b = 0$ for $\sin^2 2\varphi = 0$, and $b = 1.72$ and $b = 0.294$ for $\sin^2 2\varphi = 1$. Since b values greater than 0.5 are not allowed, b varies between 0 and 0.294. An average value of $b = 0.15$ was used for shear waves along the [100] axis in $MgAl_2O_4$. Similarly for YAG, $b = 0.071$ and $b = 0$ for $\sin^2 2\varphi = 0$ and $b = 0.054$ and 0.174 for $\sin^2 2\varphi = 1$. A value of $b = 0$ was used for shear waves along the [100] axis in YAG, which is almost an elastically isotropic material.

From the b parameter values for longitudinal and shear waves in the delay materials of interest, one can calculate the acoustic diffraction from the curves given by Papadakis and shown in Figure 4.

Relative loss, R_L, is plotted there as a function of normalized propagation distance S for several values of the anisotropy parameter b. At the origin successive curves have been offset by 1 decibel for clarity; all curves have an actual value of 0 decibels at the origin. The normalized propagation distance S is related to the actual propagation distance z by

$$S = z \lambda / r^2 \tag{10}$$

where λ is the wavelength of the sound wave and r is the transducer radius. In dealing with delay lines of length L, one can observe signal outputs only for propagation distances which are integral multiples of L. For a double ended delay line the nth observable pulse occurs for a sound wave which has traveled

$$z = nL, \text{ or } S_n = nL\lambda / r^2 \tag{11}$$

and for a single-ended delay line the nth observable pulse has traveled

$$z = 2nL, \text{ or } S_n = 2nL\lambda / r^2 \tag{12}$$

The propagation distance X between observable pulses is $x = 2L$ for single-ended lines and $X = L$ for double-ended lines. In this study only long delay times which correspond to large S values are of interest. The attenuation due to diffraction, α_D, is estimated by fitting a straight line to the appropriate diffraction curve in Figure 4 as is shown for the curve $b = 0.0$.

$$\alpha_D = \frac{R_L(n) - R_L(m)}{z(n) - z(m)} \tag{13}$$

The attenuation per reflection due to diffraction, Γ_D, is

$$\Gamma_D = \frac{R_L(n) - R_L(m)}{n-m} \tag{14}$$

Using Equations 12 and 14, Γ_D may be rewritten

$$\Gamma_D = \frac{\delta L \lambda}{r^2} \left[\frac{R_L(n) - R_L(m)}{S_n - S_m} \right] \quad \delta = 1 \text{ for DE line; } \delta = 2 \text{ for SE line} \tag{15}$$

where the constant in brackets is the slope of a line fit at large S to the appropriate diffraction curve of Figure 4. The linear fit to the actual diffraction loss ignores the fluctuations which occur in the Fresnel region and extrapolates at the origin to a value which is in error by a few decibels. This intercept error is small in comparison to the total diffraction loss of the last observable pulses and has little effect on the calculation. Even so, it is taken into con-

16

sideration as a small correction in these calculations by adding it, with appropriate sign, to the insertion loss. For low diffraction loss a delay material should have low sound velocity, a large, positive b value, and should be available in large size so that transducers of as large a diameter as possible can be used. The diffraction loss will decrease as the frequency increases. When the delay material is specified and the transducer diameter is chosen, Equation 15 can be normalized to a convenient frequency (200 MHz). Then the diffraction loss per reflection can be written as

$$\Gamma_b = C \frac{200}{f} \text{ dB/ reflection} \tag{16}$$

where f is the frequency in MHz and C is a constant.

E. DELAY LINE DESIGN

The design of long reverberation time delay lines can be approached in two ways. One way is to select the materials from Tables 1, 2, and 3 and to decide on the thickness of the top electrode, transducer, and bond electrode; the clamped capacitance of the transducer; and the driving and load resistance. Then using the parameters from the tables with an equivalent circuit, as described in Reference 1, calculate the IL versus frequency response. Having the IL, calculate the losses as described above under "Basic Loss Equations" and divide the losses per reflection into the available power, to obtain the number of reflections and hence the total delay time.

The other approach is to select only the delay line material and the electrode material, assume values for the IL, and calculate the losses and total delay time at one frequency. Plot the results and find the IL that gives the maximum delay time; then design the transducer to have that IL using the equivalent circuit computer program. The second approach will be followed here, since it appears to be more straightforward. Because the delay line materials to be compared have different velocities of propagation, the only fair comparison is on the basis of a fixed interpulse period. It is assumed that all the delay lines have an interpulse period of 6 μs.

Longitudinal Waves in Al_2O_3 at 200 MHz

Consider a DE delay line with Al_2O_3 as the delay material and gold electrodes. The travel time per reflection is 3 μs even though every other echo is read out. The delay line length is $L = \tau' V_0 = 3.33$ cm long. Assuming values of IL from 30 to 60 decibels, calculating r from Equation 4 and using these values for r, one can calculate the acoustic conversion loss per reflection from Equation 5. These acoustic conversion loss values will be used for all the delay lines to be considered.

The electrical skin depth for gold at 200 MHz is 4.5 μm. For good electrical isolation a gold bond electrode about 5 μm thick should be used. How-

17

ever, the acoustic loss is excessive for shear waves in 5-μm-thick gold electrodes and some IL variation is evident in the transducer pass band due to this thick gold electrode. The electrical resistance of a 1-μm-thick gold electrode 0.4 inch in diameter is only 0.00078 ohm, so extra series resistance is not a detrimental factor. Transducers can be bonded with electrodes of 1 μm thickness; therefore only 1-μm-thick gold electrodes will be considered for all the delay line designs. The acoustic loss per reflection in a 1-μm-thick gold electrode is given by Equation 6, with A = 200 dB/cm at 1 GHz for longitudinal propagation:

$$\Gamma_B = 0.04 \left(\frac{f}{1000}\right)^2, \text{ or } 0.0016 \text{ dB/reflection at } 200 \text{ MHz}$$

The transducer material loss is so low that its contribution to the total loss can be neglected, as this calculation will show. The transducer material with the highest loss is quartz (3 dB/cm at 1 GHz). The maximum thickness of the transducer is 10 μm and there are two passes through the transducer per reflection. Thus the transducer material loss is 2.4×10^{-4} dB per reflection at 200 MHz. Even with 1000 reflections this loss is only 0.24 dB, which is insignificant compared to the other losses. (See Table 4 for conversion loss in transducers.)

Table 4

ACOUSTIC CONVERSION LOSS PER REFLECTION
IN TRANSDUCERS

IL dB	r	Γ_t dB/reflection
-30	0.03162	0.1395
-35	0.01778	0.0780
-40	0.01000	0.0436
-45	0.005623	0.0244
-50	0.003162	0.0139
-55	0.001778	0.0078
-60	0.001000	0.0043

The material loss of Al_2O_3 is calculated from Equation 7, with $\tau' = 3\mu s$ per reflection and B = 0.2 dB/μs. Then the material loss per reflection is

$$\Gamma_M = 0.6 \left(\frac{f}{1000}\right)^2, \text{ or } 0.024 \text{ dB/reflection at } 200 \text{ MHz}$$

The acoustic diffraction loss is expected to dominate at 200 MHz for long reverberation time delay lines. It is therefore important to decide what is the maximum possible crystal diameter for the delay material. Good acoustic quality crystals of Al_2O_3, of YAG, and possibly of $MgAl_2O_4$ can be obtained up to a diameter of 0.4 inch. The maximum diameter of 0.328 inch was chosen

for the top transducer electrode for these calculations. The b parameter was previously calculated for Al_2O_3 by Equation 8 as b = 0.154. The slope of the diffraction loss curve for b = 0.15 in Figure 4 gives the following values: $R_t(n)$ = 6.31 decibels, $R_t(m)$ = 4.87 decibels, S_n = 5, and S_a = 3. Inserting these values in Equation 10 along with L = 3.33 cm, V_0 = 11.1 $\times 10^5$ cm/s, a^2 = 0.694 cm^2, and f = 200 MHz the diffraction loss is calculated to be

$$\Gamma_D = 0.0767 \frac{200}{f}, \text{ or } 0.0767 \text{ dB/reflection at 200 MHz}$$

This loss is rather high because the crystal is long and the velocity is high for Al_2O_3 even though the b parameter is in the favorable range.

With all the losses now calculated, the total delay time can be determined. At an IL of -30 decibels the available power is 80 decibels (110 dB dynamic range less the IL) to compensate for the losses. The total losses at 200 MHz are acoustic conversion loss (0.1395) plus electrode loss (0.0016) plus material loss (0.0240) plus diffraction loss (0.767) which equals 0.2418 decibel per reflection. Dividing the total loss into the available power gives the total number of reflections: 80 ÷ 0.2418 = 331 reflections. Multiplying the total number of reflections by the travel time per reflection (3 μs per reflection) gives the total delay time of 993 μs. For the next IL (-35 dB) the available power is 75 decibels and all the losses remain the same except the acoustic conversion loss, which decreases to 0.078 decibel per reflection. The total loss becomes 0.1803 decibel per reflection, and the total delay time is 1248 μ seconds. These calculations are repeated for the other IL values and the results plotted as curve 1 of Figure 5.

This curve for a DE line shows several interesting points. The maximum total delay time (1.55 ms) occurs at an IL of 50 decibels. Thus, to design long reverberation time delay lines the IL must be rather high. At 50 decibels IL the acoustic loss is dominated by diffraction and material loss, which limits the total delay time. The curve is rather flat from 40 to 55 decibels IL.

Next consider a SE delay line with Al_2O_3 as the delay material and a gold electrode. The travel time per reflection is 6 μs, and every echo is read out. The acoustic conversion loss and the electrode loss are the same as in the DE case. The material loss and the diffraction loss are both doubled. At an IL of -30 decibels the available power is 80 decibels. The total losses at 200 MHz are acoustic conversion loss (0.1395) plus electrode loss (0.0016) plus material loss (0.0480) plus diffraction loss (0.1534), which equals 0.3425 decibel per reflection: 80 ÷ 0.3425 = 233 reflections, and multiplying by 6 μs per reflection gives a total delay time of 1398 μs. The total delay time is calculated for the other IL values and the results plotted as curve 2 in Figure 5. The curve is similar to curve 1 except that the maximum total delay time is 1.72 ms and occurs at an IL of 45 decibels. The SE delay line always has a greater total delay time than the DE delay line, because the total number of reflections is less and thus the acoustic conversion and the electrode losses are less compared to the DE delay line.
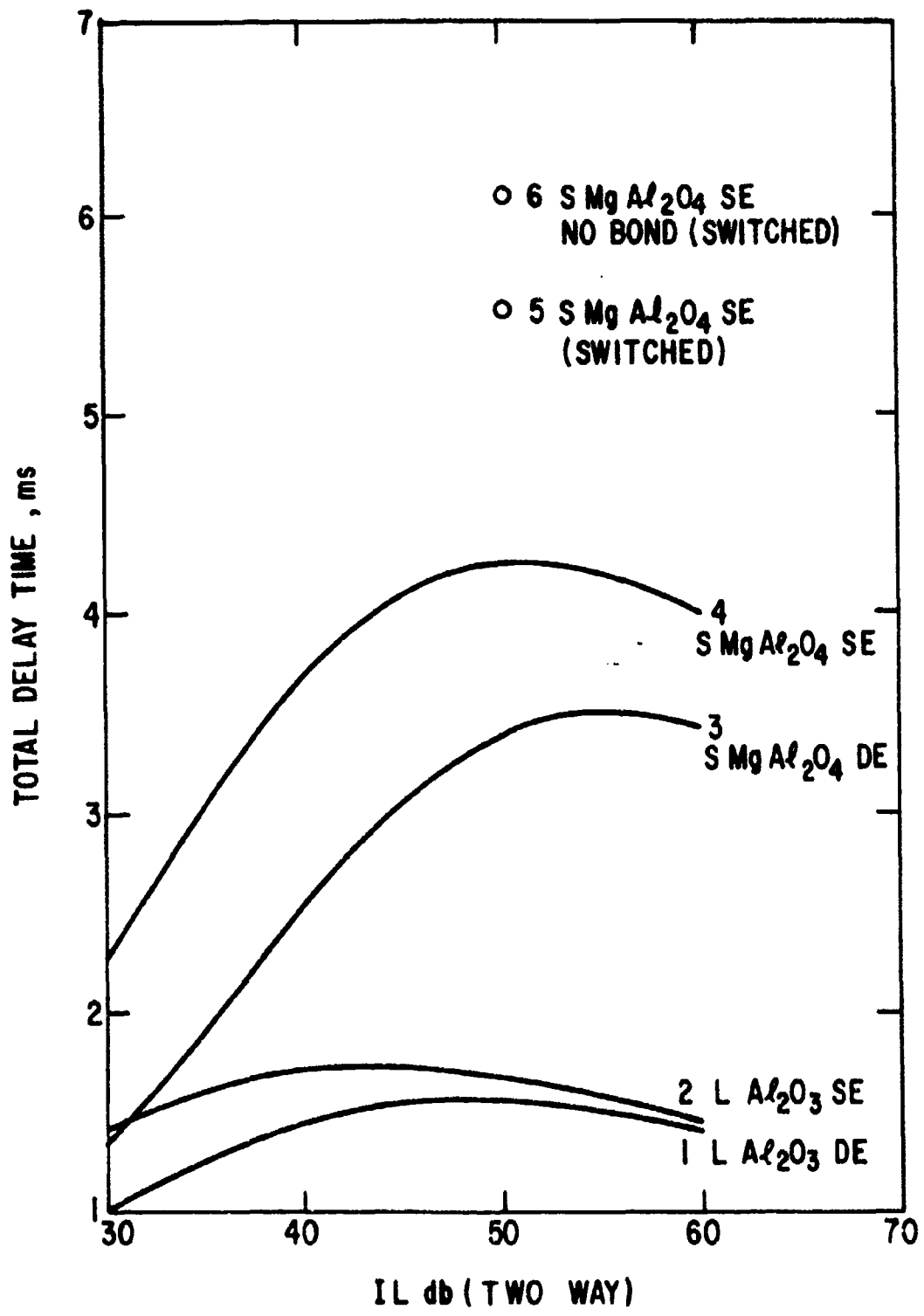
Figure 5. Total Delay Time Versus Insertion Loss at 200 MHz

20

It can now be seen that the transducer should be designed to have an IL of from 40 to 55 decibels for maximum total delay time. The equivalent circuit computer program will be used to design two transducers (longitudinal mode ZnO and CdS) on Al_2O_3 to show how the IL varies with frequency and how the designer can change the response to achieve the desired IL. Consider longitudinal mode ZnO, which has a good acoustic impedance match to Al_2O_3 (ratio $Z_0/Z_1 = 1.23$). The transducer thickness is given by $t = V_1/2f_0$, where V_1 is the longitudinal mode velocity for ZnO from Table 1 and f_0 is the desired center frequency. For $f_0 = 200$ MHz the transducer thickness is 15.8 μm. The maximum transducer bandwidth is obtained when the transducer is electrically matched to the driving and load resistance ($R_0 = 50$ ohms) (Ref. 8). This occurs when $\omega C_0 R_0 = 1$; thus the clamped capacitance of the transducer is $C_0 = 15.9$ pf at 200 MHz.

The top electrode thickness was selected to be 1000Å of gold, the bond electrode thickness 1 μm of gold, and the velocity, acoustic impedance, and coupling coefficient were taken from Tables 1, 2, and 3. The two-way IL was computed for these parameters from 60 to 340 MHz and the results are shown as curve 1 of Figure 6. A single minimum IL occurs at 140 MHz, which is characteristic of acoustically matched transducer-propagation material. The minimum IL does not occur at 200 MHz because the transducer is mechanically loaded by the delay line material. The minimum IL can be moved to 200 MHz by decreasing the transducer thickness to 10.5 μm, which increases the transducer f_0 to 300 MHz. The results are shown in curve 2 of Figure 6. The minimum IL has shifted to 200 MHz and has a value of 16.5 decibels, which is less than before because this is also the electrical matching frequency for a $C_0 = 15.9$ pf. This is the minimum IL that can be expected for this transducer with a $k_t = 0.22$. The 3-decibel bandwidth is 47 percent.
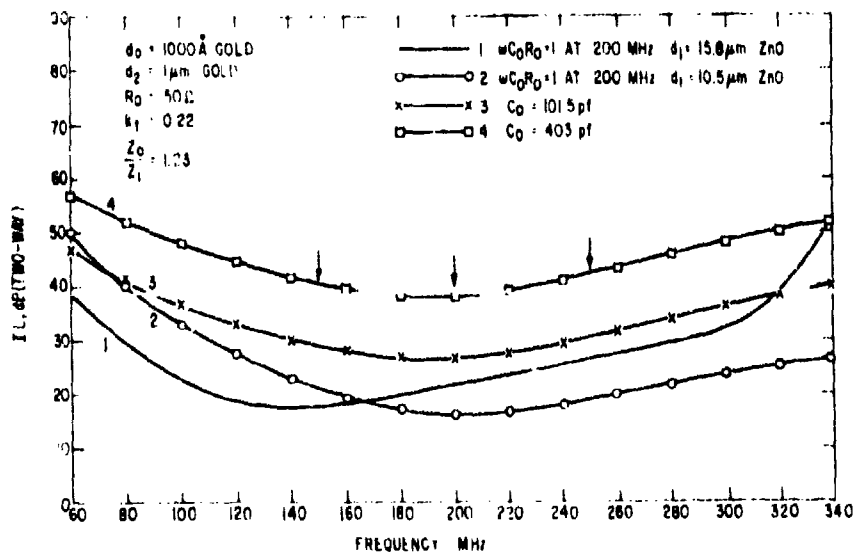
Figure 6. Insertion Loss Versus Frequency for ZnO-L on Al_2O_3

The transducer response of curve 2 is not a good design to use for long reverberation time delay lines. The IL is too low; this would limit the total delay time because of high acoustic conversion loss. Furthermore, for a 10.5-μm-thick ZnO transducer the top electrode diameter is 0.065 inch for a clamped capacitance of 15.9 pf; this would result in an enormous acoustic diffraction loss. The only parameter the designer can change at this point is the clamped capacitance C_0. With an increase in the top electrode diameter to 0.164 inch, the C_0 becomes 101.5 pf and the IL versus frequency response is shown as curve 3 in Figure 6. The minimum IL at 200 MHz has increased 10 decibels but so has the VSWR of the device. These devices in general will all have a high VSWR. Increasing the top electrode diameter to 0.328 inch, the value used for the loss calculations, raises the C_0 to 403 pf; the results are shown as curve 4 in Figure 6. The minimum IL at 200 MHz is 38 decibels and the IL varies 4.5 decibels over the desired bandwidth from 150 to 250 MHz. By varying the transducer thickness, the IL can be made to decrease, remain flat (as shown in curve 4), or increase as a function of frequency over the desired bandwidth. The authors consider the IL response of curve 4 to be an adequate transducer design for a long reverberation time delay line.

The second transducer design is longitudinal mode CdS, which has an acoustic impedance mismatch to Al_2O_3 (ratio $Z_0/Z_1 = 2.06$). The CdS transducer thickness for $f_0 = 200$ MHz is 11.15 μm. The same parameters were used as in the previous transducer design: $C_0 = 15.9$ pf, $R_0 = 50$ ohms for $\omega C_0 R_0 = 1$ at 200 MHz, top electrode thickness 1000Å of gold, the bond electrode thickness 1μm of gold, and the appropriate velocity, acoustic impedance, and coupling coefficient from Tables 1, 2, and 3. The results are shown in curve 1 of Figure 7. The IL response now has a double minimum at 110 MHz and 290 MHz, which is characteristic of acoustically mismatched transducer-propagation
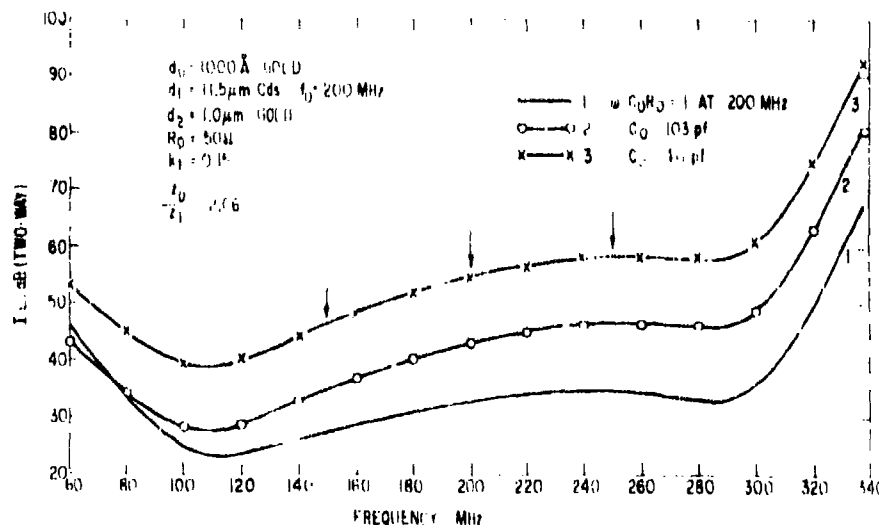
Figure 7.   Insertion Loss Versus Frequency For CdS-L On Al_2O_3

22

material. The IL of CdS transducers is higher than ZnO transducers because of the lower value of k_t for CdS. Increasing the top electrode diameter to 0.164 inch, C becomes 103 pf and again the IL has increased 10 decibels, as shown in curve 2 of Figure 7. By increasing the top electrode diameter to 0.328 inch, the value used for the loss calculations, $C_0 = 411$ pf and the IL is 55 decibels at 200 MHz, as shown in curve 3 of Figure 7. The IL variation of curve 3 is 12 decibels from 150 to 250 MHz. This IL variation could be reduced by changing the transducer thickness, but that will not be necessary, as will be seen when the total delay time variation across the transducer band-width is calculated.

The next step is to go back and recalculate the SE delay line losses, using the actual values for the IL at several frequencies across the transducer band width, to recalculate the acoustic conversion loss using the computer calculated values of IL, and to account for the frequency squared variation of electrode and material losses and the reciprocal frequency variation of the diffraction loss. At the frequencies marked on curve 4 in Figure 6 for the ZnO-L Al_2O_3 SE delay line, the total delay time variation is as shown in curve 1 of Figure 8. The total delay time variation is 13.8 percent. At the frequencies marked on curve 3 in Figure 7 for the CdS-L Al_2O_3 SE delay line, the total delay time variation is shown as curve 2 in Figure 8. There the total delay time variation is only 4.4 percent. The IL variation in this case has conveniently compensated for the frequency variation of the electrode material and diffraction losses. Other methods of total delay time compensation such as variable system gain could be considered, but that involves system details which are better left to the system designer. The point to be stressed here is that there is considerable flexibility in the transducer design, depending on what one wants to design for.

Shear Waves in $MgAl_2O_4$ at 200 MHz

Consider a DE delay line with $MgAl_2O_4$ as the delay material and gold electrodes. The travel time per reflection is 3 μs, even though every other echo is read out. The delay line length is $\tau'V_b = 1.96$ cm. Values are again assumed for IL, and r calculated from Equation 4 and the acoustic conversion loss from Equation 5 as before.

The acoustic loss per reflection in a 1-μm-thick gold electrode is given by Equation 6 with A = 1000dB/cm at 1 GHz for shear propagation

$$\Gamma_E = 0.2 \left(\frac{f}{1000}\right)^2, \text{ or } 0.0080 \text{ dB/reflection at 200 MHz}$$

The material loss of $MgAl_2O_4$ is calculated from Equation 7, with $\tau' = 3\mu s$ per reflection and B = 0.04 dB/μs. The material loss per reflection is

$$\Gamma_M = 0.12 \left(\frac{f}{1000}\right)^2, \text{ or } 0.0048 \text{ dB/reflection at 200 MHz}$$

23
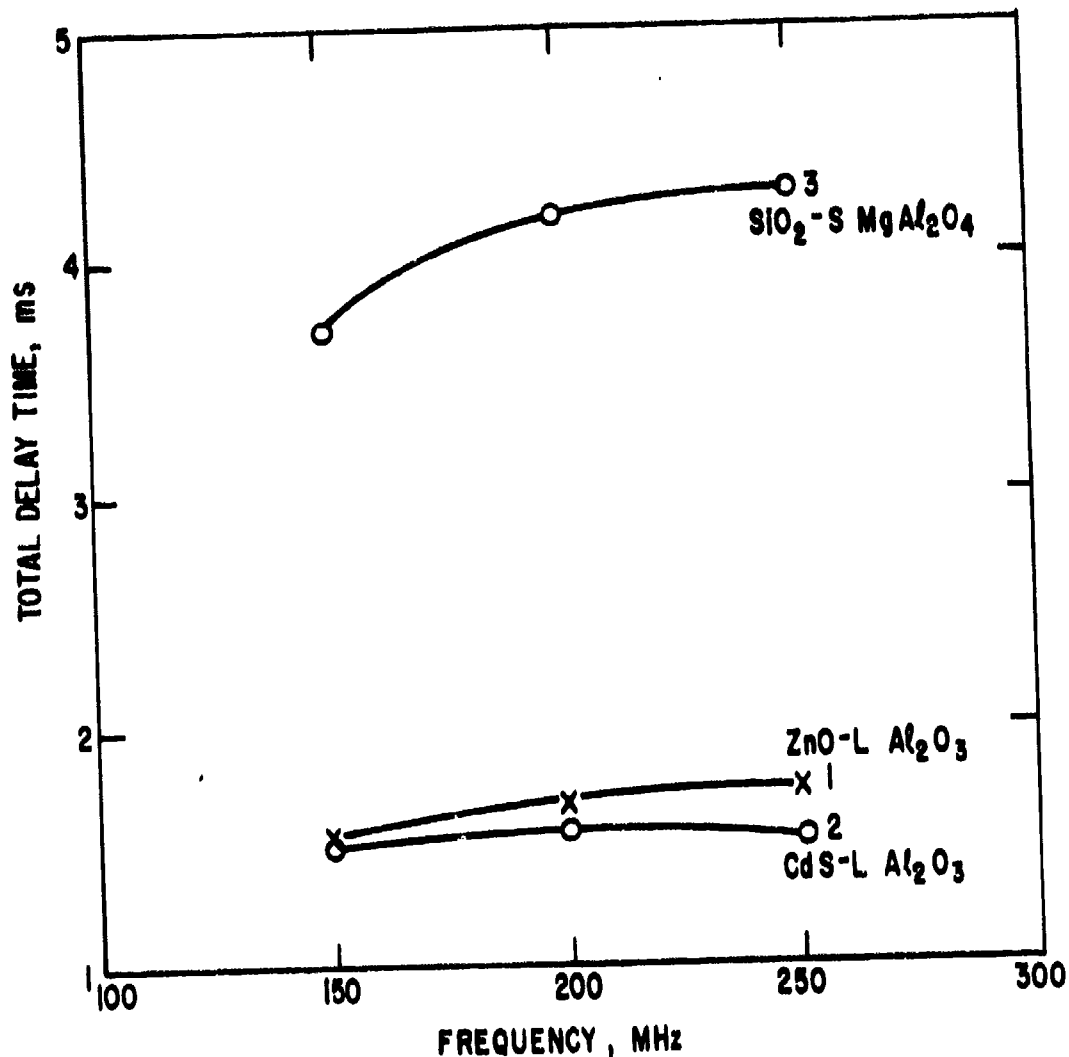
Figure 8. Total Delay Time Variation Across Transducer Bandwidth in SE Delay Lines

The acoustic diffraction loss parameter, b, was previously calculated for $MgAl_2O_4$ using Equation 9 as b = 0 to 0.204. An average value of b = 0.15 was estimated for shear wave propagation along the [100] direction in $MgAl_2O_4$. The slope of the diffraction loss curve for b = 0.15 in Figure 4 is the same as for Al_2O_3; inserting those values in Equation 10 along with L = 1.96 cm, V_D = 6.54 × 10⁵ cm/sec, a^2 = 0.694 cm², and f = 200 MHz, the diffraction loss is calculated to be

$$\Gamma_D = 0.0266\left(\frac{200}{f}\right), \text{ or } 0.0266 \text{ dB/reflection at 200 MHz}$$

This loss is a factor of three less than the diffraction loss for Al_2O_3, even though both materials have the same b parameter, because (1) the crystal is shorter for the same travel time and (2) the velocity is lower.

24

With all the losses calculated, the four losses are summed and the total delay time calculated as before. The results are plotted as curve 3 in Figure 5. The maximum total delay time is 3.5 ms and occurs at an IL of 55 decibels. At 55 decibels IL the acoustic loss is dominated entirely by diffraction loss. The rapid increase in the total delay time at low values of IL is caused by a similar rapid decrease in the acoustic conversion loss as the IL increases.

The SE delay line with $MgAl_2O_4$ delay material is calculated as previously described, with a travel time of 6 μs per reflection and the acoustic conversion and electrode losses remaining constant while the material and diffraction losses are both doubled. The results are shown as curve 4 in Figure 5. Again it is seen that the SE delay line has a greater total delay time than the DE case. The maximum total delay time is 4.25 ms and occurs at an IL of 50 decibels. The difference in total delay time is greater between curves 3 and 4 than between curves 1 and 2 because the material and diffraction losses are so much lower in shear propagating $MgAl_2O_4$ than in longitudinal propagating Al_2O_3. Again the transducer IL should be 45 to 55 decibels for maximum total delay time.

Since a high IL is desired, a transducer material with only a modest coupling coefficient will be selected. Y-cut SiO_2 has an acoustic impedance mismatch for shear wave propagation in $MgAl_2O_4$ (ratio $Z_b/Z_1 = 2.32$) and will be entirely satisfactory as a transducer material. The shear wave polarization direction in Y-cut SiO_2 must be aligned with the shear wave polarization in $MgAl_2O_4$, but this can be done with careful x-ray alignment techniques. The transducer $f_0 = 250$ MHz has been set to flatten the IL response and the transducer thickness is 7.6 μm. The same parameters were used as in the previous transducer designs: $C_0 = 15.9$ pf, $R_0 = 50$ ohms for $\omega C_0 R_0 = 1$ at 200 MHz, top electrode thickness 1000Å of gold, the bond electrode thickness 1 μm of gold, and the appropriate velocity, acoustic impedance, and coupling coefficient from Tables 1, 2, and 3. The computer results are shown in curve 1 of Figure 9. The IL is 28 decibels and is flat, with a 3-decibel bandwidth from 98 to 262 MHz. Increasing the top electrode diameter to 0.328 inch, the value used for the loss calculations, $C_0 = 286$ pf and the IL is 47 decibels at 200 MHz, as shown in curve 2 of Figure 9. The C_0 of the SiO_2 transducer is less than the C_0 of the ZnO or CdS transducers, because the dielectric constant of SiO_2 is 4.5 while it is approximately 9 for ZnO and CdS. The IL variation of curve 2 is 5.5 decibels from 150 to 250 MHz.

At the frequency points marked in curve 2 of Figure 9 the IL values were used to recalculate the acoustic conversion loss. The frequency variation of the bond, material, and diffraction losses were accounted for and the total delay time calculated as before. The results are shown as curve 3 of Figure 8. The total delay time variation is 15.7 percent across the transducer bandwidth for a shear wave SiO_2 transducer on $MgAl_2O_4$. The lower total delay time at 150 MHz is caused by the dominating diffraction loss, which is not reduced by the decrease in material and electrode losses because they are only a small fraction of the total losses. The IL response should have a negative slope
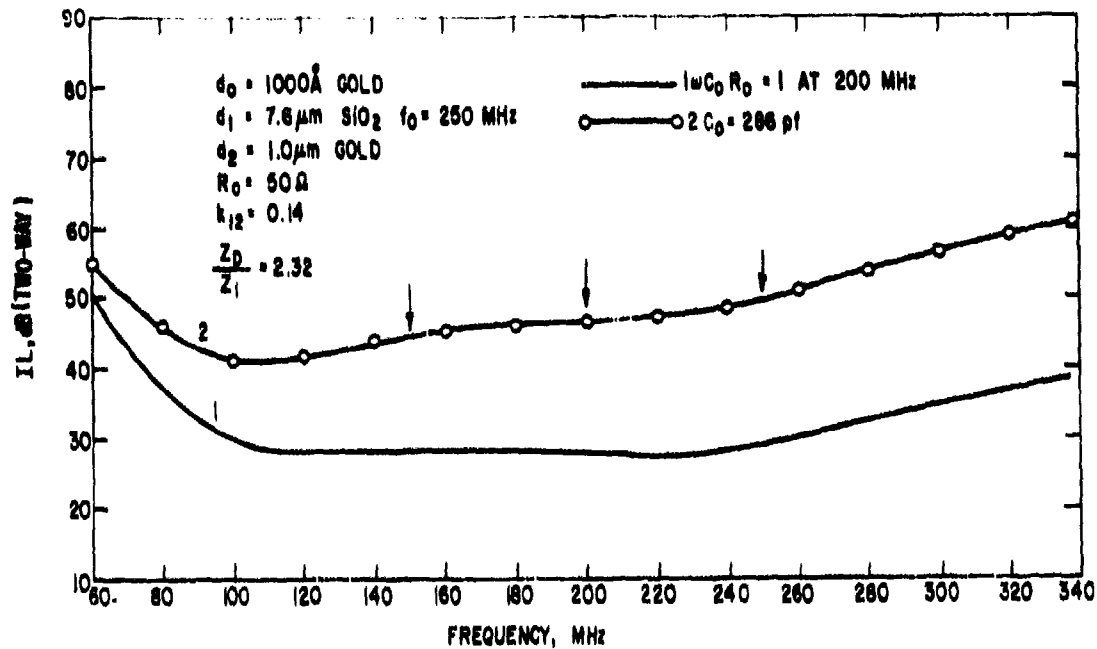
Figure 9. Insertion Loss Versus Frequency For SiO_2-S On $MgAl_2O_4$

across the transducer bandwidth to help flatten the total delay time variation. No further attempt was made to modify the transducer response in order to improve the total delay time variation.

The IL response with a SiO_2-S transducer on YAG is almost identical to the IL response with $MgAl_2O_4$ delay material, because the acoustic impedances of YAG and $MgAl_2O_4$ are so similar. Other transducer materials were also tried (ZnO-S and $LiNbO_3$-S), but because of the high dielectric constant of these materials the C_0 was very high, and thus they did not match well with the 50-ohm driving and load resistance.

Shear Waves in $MgAl_2O_4$ SE Delay Line with a Switched Impedance Transducer at 200 MHz

All the acoustic losses for shear waves in a $MgAl_2O_4$ SE delay line having been calculated, the problem remaining is the transducer design for a switched impedance delay line. The idea here is to have a transducer with a low IL to drive the delay line (two-way IL of 10 to 20 dB), then switch the transducer to a high IL for readout (two-way IL of 45 to 55 dB). A transducer material with a high coupling coefficient is needed to drive the delay line. Consider a shear mode ZnO on $MgAl_2O_4$ as the SE switched delay line. The transducer f_0 is increased to 250 MHz to flatten the IL response at 200 MHz. The transducer thickness is given by $t = V_1/2f_0$, where V_1 is the shear wave velocity in ZnO from Table 1 and f_0 is the transducer resonant frequency 250 MHz in this case. The transducer thickness is 5.44 μm. The clamped capacitance is calculated from

$$C_0 = \frac{8.854 \times 10^{-14} \times \epsilon_r \times \pi \times a^2}{4 \times t}$$

where

ϵ_r = relative dielectric constant of ZnO
a = top electrode diameter (0.833 cm)
t = transducer thickness (cm)

The clamped capacitance C_0 = 736 pf and the capacity reactance at 200 MHz is 1.08 ohms. The transducer will have a minimum IL when $\omega C_0 R_0$ = 1 at 200 MHz, which is the electrical matching condition. Thus R_0 should be 1.08 ohms for minimum IL. A driving resistance of 2 ohms can be used with only a small increase in IL. The stepdown impedance transformer has an impedance ratio of 25:1.

The remaining parameters are the same as before: top electrode thickness, 1000Å of gold; the bond electrode thickness, 1 μm of gold; and the appropriate velocity, acoustic impedance, and coupling coefficient from Tables 1, 2, and 3. The computed two-way IL is shown as curve 1 of Figure 10.
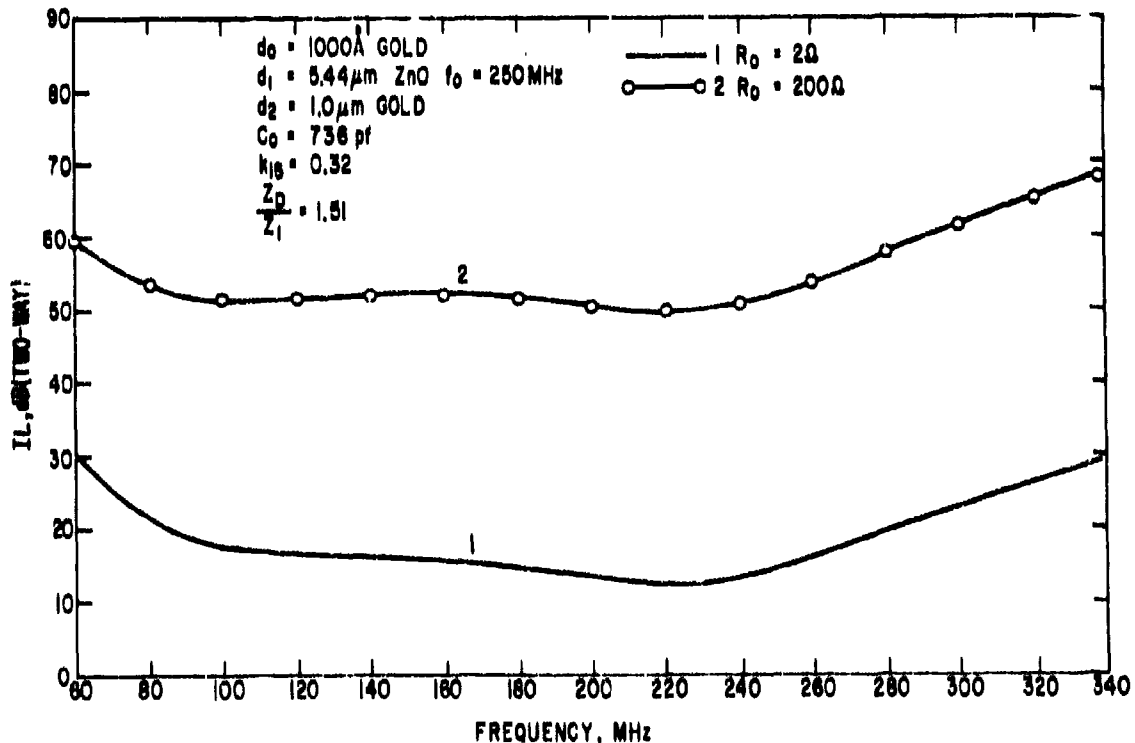
Figure 10.   Insertion Loss   Versus Frequency For ZnO-S On
MgAl$_2$O$_4$ Switched Impedance Delay Line

The IL is 13.5 decibels at 200 MHz, with a 3-decibel bandwidth of 45 percent. If the driving and load resistance is switched to 200 ohms, the IL response is as shown in curve 2 of Figure 10. The IL is now 50.5 decibels at 200 MHz, with a very flat IL response. The stepup impedance transformer required has an impedance ratio of 4:1 for a 50-ohm system. The IL for the switched SE delay line was shown in Equation 3 to be r_1r_2, which can be calculated from the computer two-way IL curves as $1/2$ $(IL)_{R=5}$ + $1/2$ $(IL)_{R=500}$ = 32 decibels at 200 MHz. Thus the available power is 78 decibels for the SE switched delay line, as compared to 60 decibels for the nonswitched SE delay line. With 18 decibels more power to compensate for the losses, the total delay time for the SE switched delay line is 5.5 ms, as shown at point 5 in Figure 5, an increase of 2.3 ms over a similar nonswitched SE delay line. If the bond electrode loss could be eliminated, the total delay time would increase to 6.1 ms (point 6 in Figure 5). The advantage of the switched SE delay line is its lower overall IL, and thus higher available power for acoustic loss compensation. The required impedance transformers are realizable, and it should be possible to build a practical switched SE delay line using this concept. A S-LiNbO$_3$ transducer on MgAl$_2$O$_4$ was also simulated in the switched configuration, but the C$_0$ value is so high that electrical impedance matching becomes impractical.

Figure 11 shows a comparison of all the materials considered, in the form of curves of total delay time versus frequency for SE delay lines. Only the results for SE delay lines were plotted, because that configuration gives the maximum delay time. These curves were computed on the assumption of constant IL for all frequencies, using the IL value that gave the maximum total delay time at 200 MHz (45 dB IL for longitudinal and 50 dB IL for shear waves). Transducers could be designed to obtain these IL values at the higher frequencies; it is felt, however, that the losses change with frequency and it is not certain that the total delay time will peak at these IL values for all frequencies. The electrode material and diffraction losses were all corrected for their frequency variation; only the acoustic conversion loss was assumed to be constant.

All the curves have a similar shape, with the total delay time decreasing as reciprocal frequency squared at high frequencies. This is not surprising, since electrode and material losses are proportional to frequency squared and these losses dominate at high frequencies. The diffraction loss can be neglected above 500 MHz for the transducer top electrode diameter used in these calculations. The maximum total delay times peak at low frequencies (200 to 300 MHz) and have a range of values from 1.7 ms for L-Al$_2$O$_3$ to 6.6 ms for S-MgAl$_2$O$_4$ (switched). The effect of electrode loss is clearly shown in the curves. If the electrode loss is eliminated, the total delay time will increase about 0.5 ms for YAG, 1.0 ms for MgAl$_2$O$_4$, and 1.5 ms for MgAl$_2$O$_4$ (switched). These increases are not constant but depend on frequency becoming less at high frequencies and greater at low frequencies. The ranking of the delay line materials is just what one would expect it to be. At 1 GHz the higher-material-loss L-Al$_2$O$_3$ has the lowest total delay time; lower-
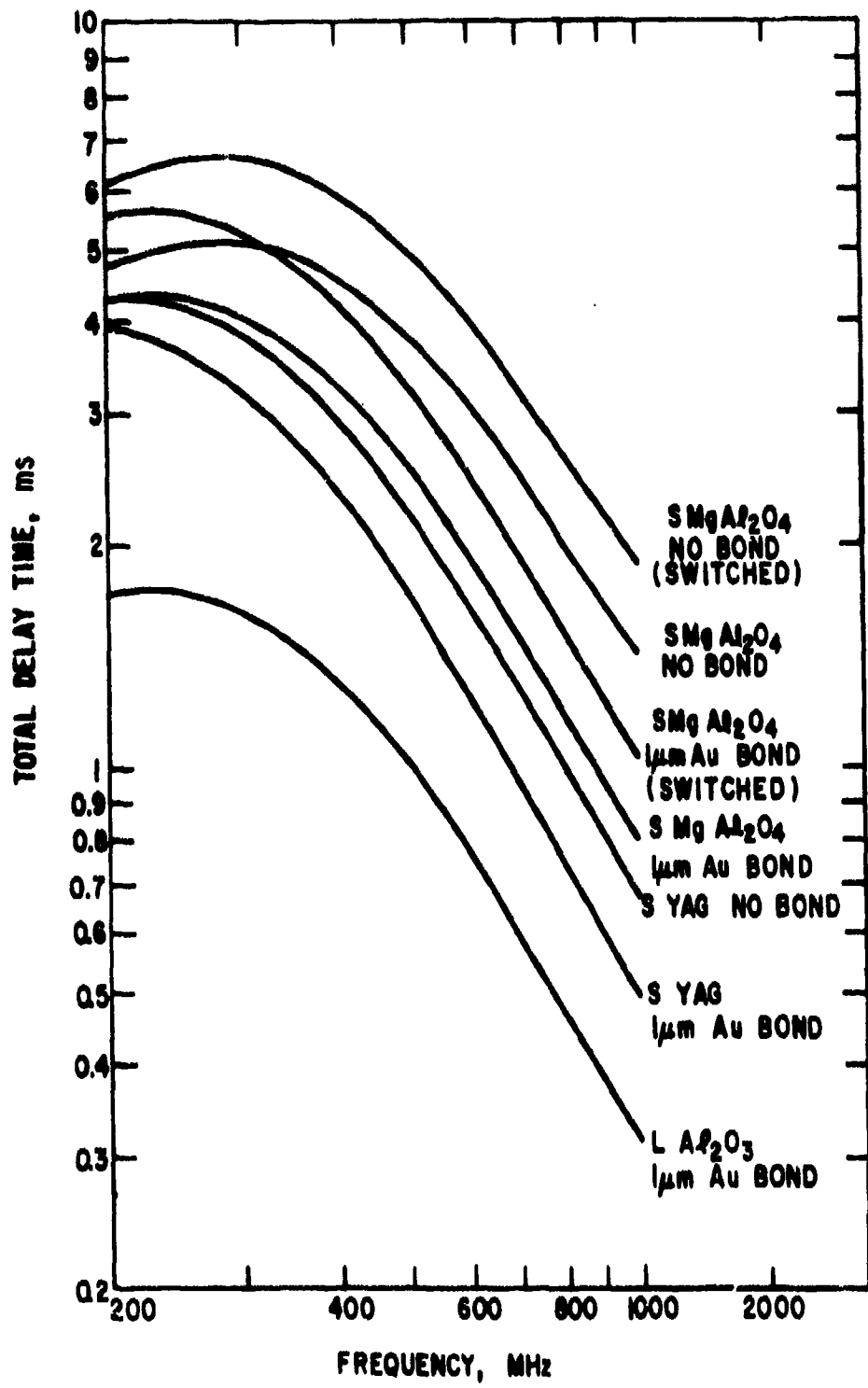
Figure 11. Total Delay Time Versus Frequency
For SE Delay Lines

29

loss S-YAG has a greater total delay time; and finally, lowest-loss S-MgAl$_2$O$_4$ has the highest total delay time.

In summary, the switched impedance SE delay line with a low-loss metal electrode, using shear waves propagating in MgAl$_2$O$_4$, will give the longest possible delay time. It appears possible to build a 1-ms delay line up to 1 GHz with the switched impedance configuration. If the system requires less total delay time, then the SE delay line can be used with less circuit complexity or the DE delay line can be used for greater electrical isolation. The acoustic loss calculations can be readily repeated for interpulse periods other than the one considered here (6μs).

The optimum IL for long reverberation time delay lines has been shown to be 45 to 55 decibels. The design of transducers with adequate bandwidth to obtain these IL's was discussed. The report also showed how the IL response of the transducer could be modified to obtain flat IL versus frequency or flat total delay time versus frequency.

Finally, it was shown that greater than 1 ms delay lines are possible with L-Al$_2$O$_3$ up to 500 MHz, with S-YAG up to 670 MHz, with S-MgAl$_2$O$_4$ up to 870 MHz, and with switched impedance S-MgAl$_2$O$_4$ up to 1000 MHz. Bond loss can be reduced by using other metals for electrodes so that these results can be obtained at even slightly higher frequencies. It will be necessary to determine if these results are experimentally achievable by constructing several types of delay lines.

It is interesting to note that the information handling capacity of a device is related to its delay time-bandwidth product. Since the bandwidths are nearly 50 percent, this parameter can be estimated by locating the frequency at which a line of slope unity, one decade decrease in τ for one decade increase in frequency, is tangent to the curves of Figure 11. This is the frequency of greatest delay time-bandwidth product. The frequency is near 400 MHz and the delay time-bandwidth product is near 10^6. The value of 10^6 is considerably higher than that of most other devices.

F. MEMORY DEVICES AND MATCHED FILTERS

In communication, radar, or sonar systems, it has been found useful to code signals which are transmitted and then to decode them with a matched filter (Refs. 9 and 10) that has the property of providing maximum signal-to-noise ratio in the presence of white noise. The signal may be coded to provide secure communication channels or to provide simultaneous range and velocity information. Signals may be coded by frequency, amplitude, or phase modulation or a combination of these. Examples of coded waveforms are described below mathematically.

30

Frequency Modulated Signal:

$$e(t) = [u(t_0) - u(t_0+\Delta)]\cos\left[2\pi\left(f_0t+\frac{1}{2}k_2t^2 + \frac{1}{3}k_3t^3 + \ldots\right)\right]$$ (17)

for which the instantaneous frequency f is time dependent

$$f = \frac{d}{dt}\left(f_0t + \frac{1}{2}k_2t^2 + \frac{1}{3}k_3t^3 + \ldots\right)$$ (18)

$$f = f_0 + k_2t + k_3t^2 + \ldots$$ (19)

The function u(t) is a unit step function at time t_0:

$$u(t_0) = 0 \qquad t < t_0$$
$$u(t_0) = 1 \qquad t > t_0$$ (20)

and the quantity $[u(t_0) - u(t_0+\Delta)]$ makes the frequency modulated signal a pulse of duration Δ beginning at time $t = t_0$.

Discrete Coded Signal:

$$e(t) = \sum_{n=1}^{N} A_n\,[u(t+(n-1)\Delta) - u(t+n\Delta)]\cos[(\omega_0+\omega_n)t + \theta_n]$$ (21)

which consists of N signal parts that may vary in amplitude, A_n; frequency,

$$\frac{1}{2\pi}(\omega_0 + \omega_n);$$

and phase, θ_n. Signals such as these are designed to meet specific system requirements, and this is generally carried out by examining the ambiguity or autocorrelation function of the signal (Refs. 9 and 10). A familiar example of the use of a coded waveform is that of linearly frequency modulated radar, chirp radar. The signal is given by Equation 17, with value $k_j = 0$ for $j > 2$. Upon reception, the modulated signal is sent through its matched filter, which has the property of being linearly dispersive and of delaying the frequency components of the signal by different amounts so that they catch up with one another to produce a short pulse of large amplitude. The signals must be designed to meet system requirements, since the performance of the system will be determined by the signal coding. Once the signal is specified, the matched filter is determined. If the signal is e(t) with a spectrum $E(\omega)$,

31

$$E(\omega) = \int_{-\infty}^{\infty} e(t)e^{j\omega t}dt \qquad (22)$$

The the matched filter is a filter network with impulse response h(t) proportional to the time inverse of the signal

$$h(t) = ke(-t) \qquad (23)$$

where k is a constant.

An equivalent definition of the matched filter is made from the matched filter transfer function, $H(\omega)$:

$$H(\omega) = kE^*(\omega)e^{-j T_d} \qquad (24)$$

where T_d is a delay constant, and where

$$H(\omega) = \int_{-\infty}^{\infty} h(t)e^{j\omega t}dt \qquad (25)$$

Design of the signal determines the system performance and specifies the matched filter. In practice one does not attempt to build a filter with sufficient bandwidth to accommodate all of the sidebands of $E(\omega)$ as specified by Equation 24. Filters actually used are approximations to Equations 23 and 24, with a finite number of stages and a finite bandwidth. In some applications it is more important to reduce the side. lobes of the filter output than to maintain maximum signal-to-noise ratio, and the filter characteristics are slightly modified for this purpose.

Summary of Matched Filters

With this brief introduction to matched filters as background, the purposes of this portion of this report can be summarized. The practical advantages of coded waveforms and matched filters imply that acoustic delay devices must be examined for their usefulness as memory elements for coded waveforms. Specification of delay time, bandwidth, and insertion loss is not sufficient. Distortion of a coded waveform must also be considered. In the remainder of this section the practical advantages of matched filtering will be listed. A parameter will be introduced to specify the quality or information handling capability of a matched filter. A description will be given of the ranges in frequency and bandwidth in which matched filters can be constructed with available technologies. An examination will be made of the applicability of bulk-wave acoustic delay lines and other devices as memory elements for coded signals. The relationship will be presented between the choice of materials for delay medium, bond, and transducer and the performance of bulk-wave delay lines as memory elements for coded signals.

The advantages of matched filtering include:

- Efficient use of available transmitter power.

- Improved system capability -- range and velocity resolution in radar or sonar, information density, and security in communications.

- Reduced interference by unwanted signals that do not have the properties of the coded waveform.

- Real time extraction of important parameters from the received signal.

Grant et al (Ref. 11) have recently described the value of matched filtering techniques in meeting the increasingly stringent requirements for communication, identification, and surveillance in air traffic control systems.

A useful parameter for specifying the information handling capability of a matched filter is the product of filter delay time and bandwidth, D, frequently called the pulse compression ratio in radar. It may be understood by reference to Figure 12. A sharp pulse of duration T_1 contains a wide spectrum of frequencies. When such a pulse is applied to a filter that delays the high-frequency components with respect to the low-frequency components, a time stretched signal, duration T_2, with frequency modulation is the output from the filter. This signal may be amplified and transmitted. On reception it can be compressed again by passing through a conjugate filter which delays low-frequency components with respect to high-frequency components. Bandwidth is required if a short pulse is to be handled, and time delay is required if the
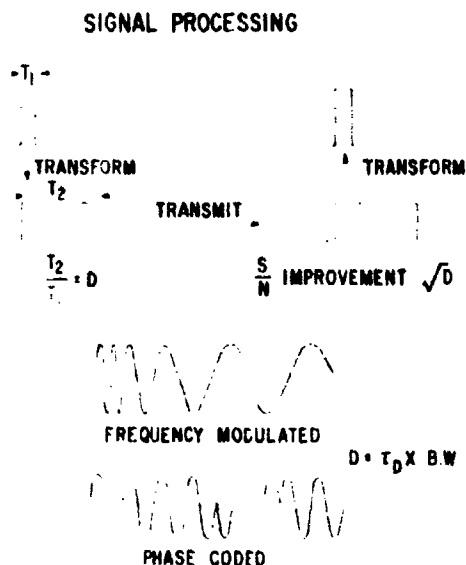
SIGNAL PROCESSING

Figure 12. Coded Wave Forms in Signal Processing

pulse is to be stretched and recompressed. The product of delay and band-width, D, is equal to the ratio of the durations of the stretched and compressed pulses, and is a measure of the information handling capability of the system.

An alternative way of thinking about D is to note that the range resolution of a radar system is inversely proportional to D. Early radar systems used a continuous signal for accurate velocity estimation, with no range information; and a sharp pulse for range estimation, with little velocity information. Such a system can be optimized to provide simultaneous range and velocity resolution by proper design of a coded signal and the fabrication of matched filters for that signal. The delay time-bandwidth product, D, is the parameter which relates to the product of range resolution and velocity resolution.

In recent years, two technologies have produced a new flexibility and operating range for matched filters that may be readily fabricated. These are the surface acoustic wave (SAW) technology and silicon technology. Figure 13 summarizes the capabilities of SAW technology today. The boundaries in-
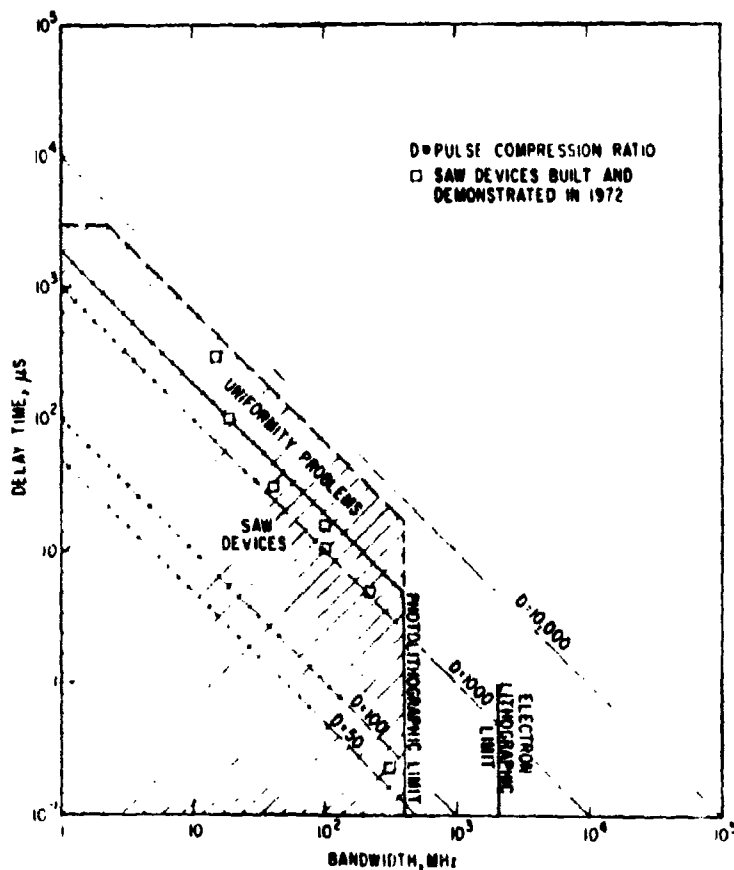
Figure 13. Delay Time Versus Bandwidth for Surface Acoustic Wave Devices

34

dicated will move as the technology improves. Plots similar to Figure 13 have been independently developed by Bell et al. (Ref. 12) and by Martin (Ref. 13). The horizontal and vertical axes of Figure 13 are bandwidth and delay time; consequently the dashed diagonal lines are lines of constant pulse compression ratio D, and several such lines are drawn in and labeled. The shaded region bounded by a solid line indicates the region in which SAW devices can be fabricated today. The bandwidth limitation is set by the resolution capabilities of photolithography or electron beam lithography in defining very fine transducer finger pairs. The vertical limits are set by substrate size, uniformity of sound velocity over the substrate, the information handling power of lenses used in processing, etc. For the very long delay times shown at lower frequencies, closed paths or spiral paths around a substrate must be used.

Silicon technology has provided several types of devices that store electrical charge capacitatively and move it from site to site with a clock pulse. The quantity of charge can be varied continuously, so these devices can be operated in either digital or analog modes. For the purposes of this report the authors will not distinguish between junction devices (Ref. 14) (bucket brigades, BBD) and MOS surface charge devices ((CCD (Ref. 15), SCT (Ref. 16)). To avoid the multiplicity of names associated with the silicon devices, they will be collectively referred to here as clocked analog delay devices (CLAD). In shifting charge from site to site, some charge is left behind and the efficiency of the transfer degrades as the frequency increases. Consequently, the speed or bandwidth of the device is related to the number of sites, and this is a limitation on the transfer of information into or out of the device.

Reasonable limits for the input and output capabilities of CLAD devices are shown in Figure 14 by the two diagonal lines that were calculated for P and N channel MOS realizations. Bucket brigade devices can be fabricated by conventional techniques with capabilities comparable or slightly superior to the N channel MOS devices. Further developments in silicon technology with buried channels and very fine structures can be expected to increase CLAD bandwidths by about a factor of two. In the time delay-bandwidth region in which they function, CLAD devices have considerable advantage over SAW devices in being compatible with other silicon devices, in both signal level and fabrication procedures, and in being clocked devices which can store information for significant times until called for. A reasonable estimate of storage time is given by the horizontal line labeled "CLAD Memory Time." This value is considerably below the theoretical limit and is affected by differential charge leakage at the storage sites which must be controlled by processing techniques. CLAD devices may be used as matched filters and as memory elements. The dark circles show a reasonable set of goals for CLAD memory (Ref. 17).

The memory time of a $MgAl_2O_4$, spinel delay line is shown on Figure 14 for two different transducer geometries. The calculations are reported in
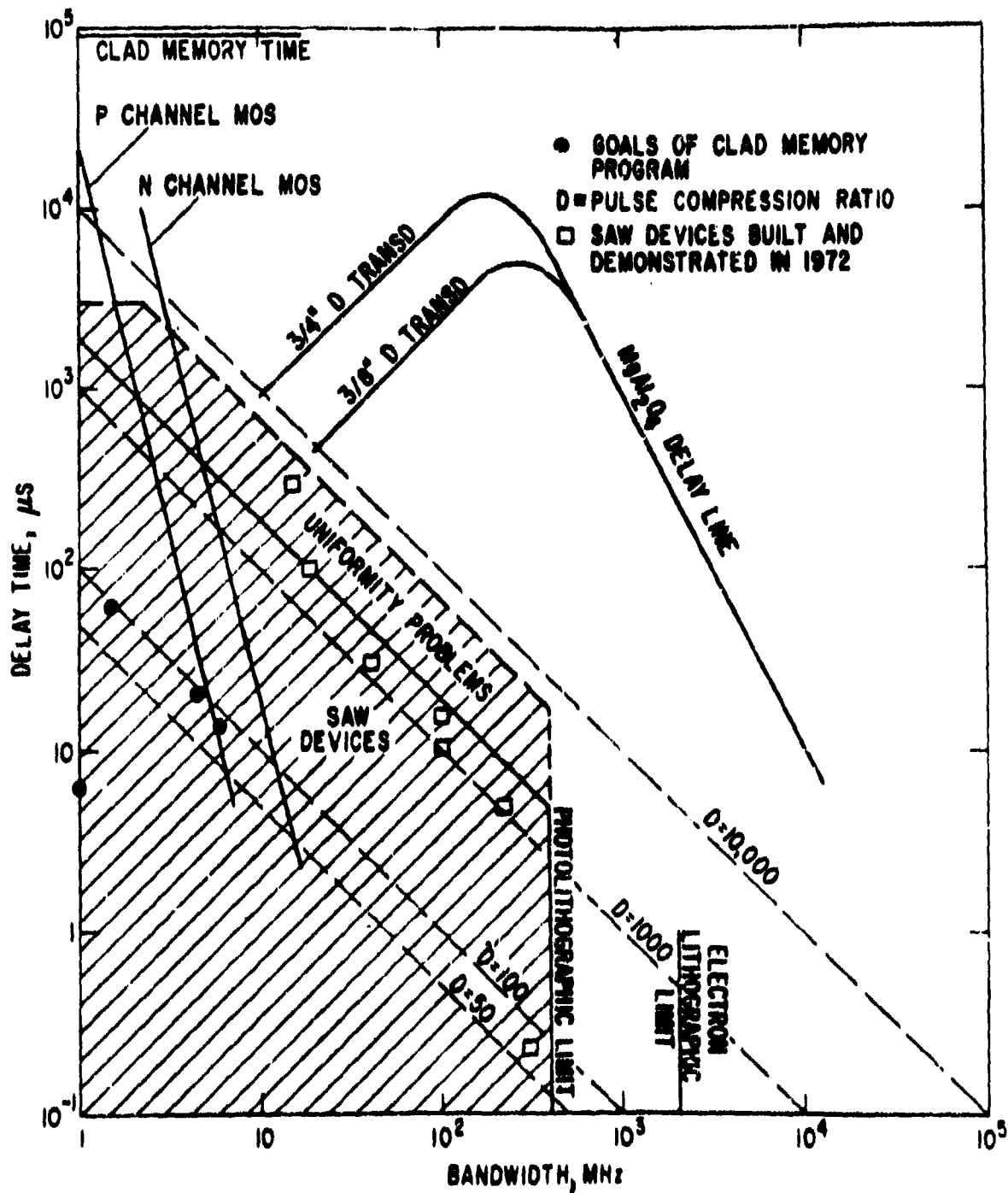
Figure 14. Delay Time Versus Bandwidth for Silicon Clocked Analog Delay (CLAD) Devices and for Bulk Acoustic Wave Devices

detail in this section of the report, under "Delay Line Design." Inspection of Figure 14 shows that CLAD devices should be considered for applications requiring matched filtering or memory with bandwidth requirements of about 10 MHz or less. Where greater bandwidths are required, SAW devices provide a unique technology for realizing matched filters. Bulk-wave delay lines are seen to be suitable as memory elements in this bandwidth region.

Another potentially useful memory device for bandwidths above 10 MHz is the wraparound surface acoustic wave delay line. This device has been limited to the cubic piezoelectric material $Bi_{12}GeO_{20}$ (BGO) up to the present, because of mode conversion in other piezoelectric materials as the surface acoustic wave propagates around the curved edges of the device. The intrinsic attenuation in BGO is greater than in $MgAl_2O_4$ and limits delay time for passive devices as shown in Figure 15.
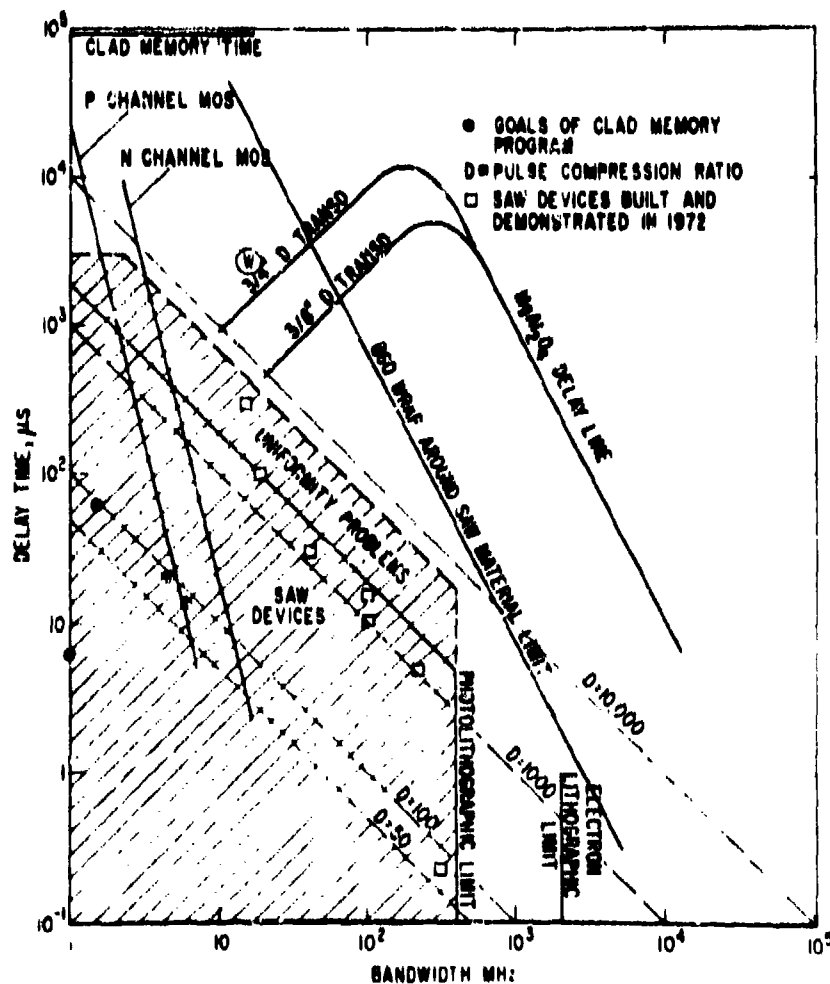
Figure 15. Delay Time Versus Bandwidth for Surface
Acoustic Wave Wraparound Passive Devices

It is possible to compensate for these losses by acoustic amplification, but only at the cost of introducing noise and dispersion. To the authors' knowledge the limitations of active SAW wraparound delay lines due to noise and dispersion have not been characterized for memory of coded signals. Similarly, the performance of bulk-wave acoustic delay lines as memory elements for coded signals is markedly affected by the impedance match between the delay medium bond and transducer. This problem is considered in detail below. The present status of the several types of devices just discussed is summarized in Table 5.

Table 5

COMPARISON OF MATCHED FILTER AND MEMORY DEVICES

Function	Device	Bandwidth (MHz)	Problems
Matched filter	CCD	≤ 10	--
Matched filter	SAW	> 10	--
Memory	CCD	≤ 10	Differential charge leakage
Memory	SAW	> 10	Noise buildup, dispersion
Memory	Bulk acoustic	> 10	Impedance matching

G. IMPEDANCE MATCHING AND THE MULTIPATH PROBLEM

Application of a memory element in a generalized system with coded signals is shown in Figure 16. A coded signal is generated and put on a trans-
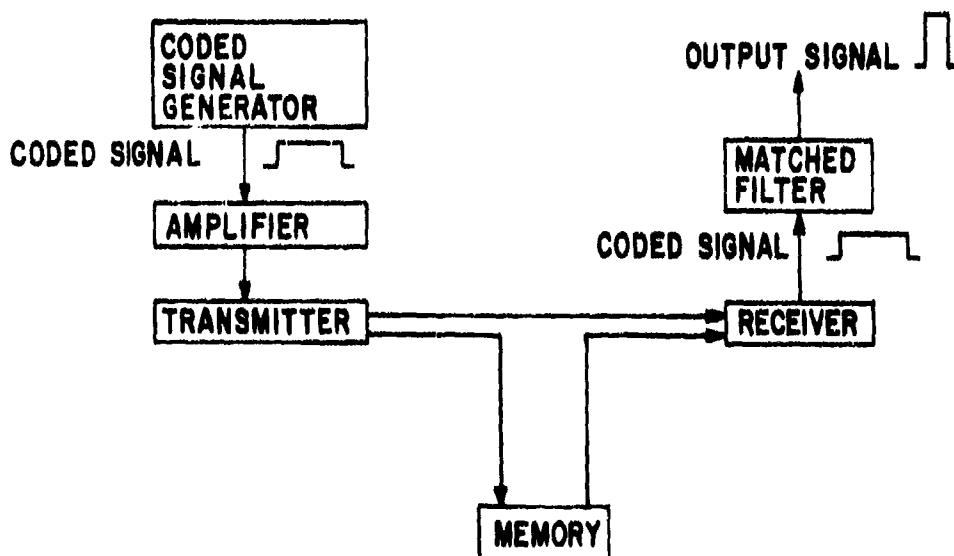
Figure 16. General System Using Coded Signals and Memory

The function of the memory element is to sample the coded signal, store it, and return it to the receiver with sufficiently low distortion so that the output signal from the matched filter is not appreciably distorted. The distortion allowable on the output signal is a system requirement which will vary from system to system. In this section the effect of the acoustic impedance mismatch between transducer and delay line is considered as a source of distortion, and a simple relationship is derived between the impedance mismatch and the distortion of the output signal for arbitrary coding. If the allowable distortion is known from system requirements, the required accuracy of acoustic matching can be calculated.
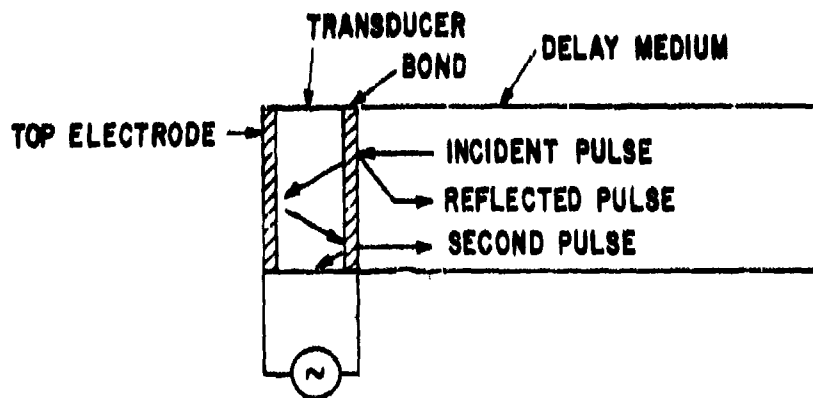
Figure 17. Transducer and Delay Medium Schematic

Whatever the coding of a signal waveform, it has a finite bandwidth and a center frequency f_n. The delay line, shown schematically in Figure 17, is designed to have a bandpass characteristic appropriate to the signal; this implies that the transducer thickness would be approximately 1/2 wavelength thick at f_0. Thus,

$$d = v_t/2f_0 \tag{26}$$

where d is the transducer thickness and v_t is the velocity of sound in the transducer material.

The delay line functions as a memory element by conversion of the electronic signal into a sound wave by the piezoelectric transducer. The sound pulse travels back and forth through the delay line many times. Each time that it reaches the transducer, a small fraction of the sound pulse is reconverted into electrical energy by the transducer to provide a replica of the original signal. If there is an acoustic impedance mismatch between the transducer, delay medium, top electrode, or the bond, a partial reflection occurs at that interface, as indicated in Figure 17. Because the top electrode and the bond a are thin, the most important impedance match is that between the transducer and the delay media. The portion of the signal which is transmitted into the transducer is delayed with respect to the directly reflected portion by a time, T:

$$T = 2d/v_t = 1/f_0 \qquad (27)$$

which is just the period of the signal center frequency. When an acoustic pulse reaches a mismatched transducer an infinite series of pulses is generated, each succeeding pulse delayed in time by an amount T. The first pulse is the reflected one. The second pulse traverses the transducer twice and is delayed by time T. The nth pulse has bounced back and forth within the transducer (n-1) times. If the acoustic impedances are nearly matched, then the second pulse is much larger than all the others because the reflection coefficient at the transducer-delay medium interface is very small. If the electrical output from the delay line is fed into a matched filter, the filter output will be an infinite series of the outputs for the original signal, each output delayed by time T. For sufficiently accurate impedance matching only a single output from the matched filter will be appreciable. Depending upon system requirements, it may be possible to allow the output from the matched filter to be broadened by several factors of T, and the impedance match required can be relaxed somewhat.

The acoustic impedances of the bond and the top electrode, and their attenuation coefficients, are also important. If the bond has a thickness that is an appreciable fraction of an acoustic wavelength, it will act as an impedance transformer between delay medium and transducer (Ref. 18) and will also contribute significantly to the delay time, T. These effects can be readily incorporated into the calculation which follows, but they have been omitted for simplicity and clarity, and to focus attention on the dominant fabrication constraint: the impedance match of the transducer to the delay medium.

The calculation of signal distortion by multiple reflection is carried out in the manner of the discussion given above. The distorted waveform from the delay line is not calculated directly, because its form will depend on the particular manner of coding as well as on the impedance mismatch. Rather, the signal amplitude is calculated for each possible time delay (time delay = 0, T, 2T, 3T ...). These amplitudes and delays give the response of the matched filter to the stored signal, since the response to the initial signal is known. The discussion above showed that a single acoustic pulse became an infinite series of pulses after one impingement on the transducer. On the next encounter with the transducer, each of these pulses becomes an infinite series. In Figure 18 the situation is illustrated for a sound pulse which has traveled through the delay line three times and has encountered the transducer three times. The quantity N gives the number of times that the pulse has traveled through the delay line and impinged on the transducer. The quantity M denotes the time delay, M x T, for a group of pulses with the same total delay. The quantity L accounts for the number of reflections at the transducer-delay media interface.

For a given time delay, or value of M, there is more than one way of generating that delay. The first received pulse of the infinite series arrives

40
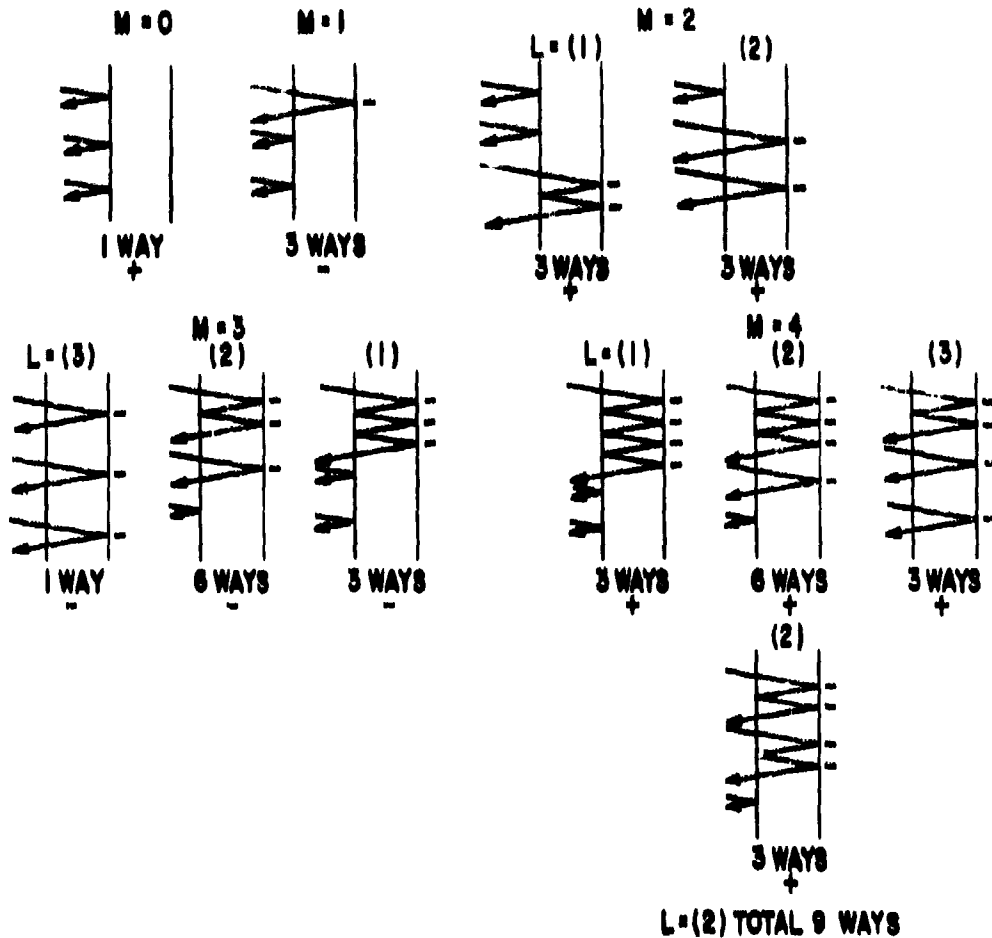
Figure 18. Pulses Derived from a Single Signal After Three
Trips Through the Delay Line

with no delay, M = 0, and corresponds to three reflections from the interface,
as shown. The next pulse is delayed by T, M = 1, and corresponds to two
reflections from the interface and one transmission through the transducer.
This can occur in three ways: on the first, second, or third pass through the
delay line. Its multiplicity is 3. The minus sign shows that the transducer-
air interface has reflected the wave once, causing a 180° phase shift. The
third pulse has a delay of 3T, M = 3, and corresponds to two passages through
the transducer. Note that this can happen in two ways: by two passages through
the transducer during one trip through the delay line, L = 1; or by one passage
through the transducer on each of two trips through the delay line, L = 2. Each
of these terms has a multiplicity of 3.

At a time delay of M = N = 3 one encounters what may be called the main
term; here impedances are nearly matched so that the reflection coefficient is

41

small. The main term is the L = M = N = 3 term, which consists of three passages through the transducer, one on each trip through the delay line. There is only one such term. The two other terms at a time delay of 3T correspond to three passages through the transducer for one trip through the delay line, L = 1; or for two passages through the transducer during one trip and one passage during another trip. The terms for successively longer delays involve more passages of the sound pulse back and forth within the transducer. For M = 4, time delay of 4T, the L = 2 case shows two different ways of getting the same time delay with the same number of reflections from the interface. For large numbers of trips through the delay line, N large, or for long time delays, large M, the drawing out of all diagrams and counting becomes tedious. The problem is considered mathematically below.

The transmission coefficient D_{ij} is defined (Ref. 19) as the ratio of the amplitude of the transmitted displacement wave in medium j to the amplitude of the incident displacement wave in medium i. The reflection coefficient V_{ij} is defined as the ratio of the amplitude of the reflected wave in medium j to that of the incident wave in medium j for a wave incident on the boundary with medium i. In terms of the impedances, Z, of the media

$$V_{ij} = \frac{Z_i - Z_j}{Z_i + Z_j} \tag{28}$$

$$V_{ij} = -V_{ji} \tag{29}$$

$$D_{ij} = \frac{2Z_i}{Z_i + Z_j} \tag{30}$$

$$D_{ji} = \frac{2Z_i}{Z_i + Z_j} \tag{31}$$

$$Z_j = \rho_j V_j \tag{32}$$

where ρ_j is the density. One notes that the transmission coefficients for the displacement waves can be greater than unity. Energy conservation may be verified by noting that the energy flux, P, is given by

$$P_j = \frac{1}{2} (\rho_j N_j) \omega^2 S_j^2 \tag{33}$$

where S is the displacement. The subscripts T and D are used to denote the transducer and the delay medium. A sound pulse incident on the transducer may be written as

$$S_D (t, z) = [u(t + z/v) - u(t - z/v + \Delta)] S_D^o (t, z) e^{j(\omega t - kz)} \tag{34}$$

where the function $S_D^o(t, z)$ includes the form of coding, such as Equation 17 or 21. The coordinates are chosen with z = 0 at the interface between the delay medium and transducer, and the expression $S_D^1 (t, z)$ is written for the

42

waves leaving this interface when S_D from Equation 34 is incident upon it once. (The transducer thickness is d.):

$$S_D^1(t,z) = \left\{ [u(0)-u(\Delta)] S_D^o(0)V_{TD} \right.$$

$$- [u(2d/v_t)-u(2d/v_t+\Delta)] D_{TD} D_{DT} S_D^o(-2d/v_t)e^{a jk_t d}$$

$$+ [u(4d/v_t)-u(4d/v_t+\Delta)] D_{TD} V_{DT} D_{DT} S_D^o(-4d/v_t)e^{4 jk_t d}$$

$$- [u(6d/v_t)-u(6d/v_t+\Delta)] D_{TD} V_{DT}^2 D_{DT}S_D^o(-6d/v_t)e^{6 jk_t d}$$

$$\left. + \ldots \right\} e^{j\omega t} \tag{35}$$

The alternation in sign accounts for the 190° phase shift at the transducer-air interface. A time shift operator U(M) is defined by

$$U(M)\ f(t) = f(t-2Md/v_t) \tag{36}$$

and an operator G(M)

$$G(M) = (-1)^M V_{DT}^M U(M) \tag{37}$$

From Equation 35:

$$S_D^2 = V_{TD}S_D + D_{TD}D_{DT}\sum_{M=1}^{\infty} (-1)^M V_{DT}^{M-1} U(M)S_D \tag{38}$$

$$S_D^1 = V_{TD}S_D + D_{TD}D_{DT}\sum_{M=1}^{\infty} G(M)S_D \tag{39}$$

or in terms of a reflection operator R,

$$S_D^1 = RS_D \tag{40}$$

$$R = V_{TD} + \frac{D_{TD}D_{DT}}{V_{DT}}\sum_{M=1}^{\infty} G(M) \tag{41}$$

Equation 40 expresses the fact that a single incident pulse is transformed into an infinite series of pulses when it strikes the delay medium-transducer interface. The usefulness of Equation 40 arises from an additive property of the operator G(N) and the ability to account for N encounters with the interface. Letting S_D^N be the infinite train of pulses after N encounters

$$S_D^N = R^N S_D \tag{42}$$

and applying the binomial theorem

$$R^N = \sum_{L=0}^{N} \frac{N!}{(N-L)!\,L!} V_{TD}^{N-L} \left[\frac{D_{TD}D_{DT}}{V_{DT}}\sum_{M=1}^{\infty} G(M)\right]^L \tag{43}$$

43

The operator $G(M)$ has the useful property

$$G(M_1)G(M_2) = G(M_1 + M_2) ,\qquad (44)$$

which can be used to reduce the product of L infinite summations to a single summation

$$\prod_L \sum_{M=1}^{\infty} G(M) = \sum_{M=1}^{\infty} P_M^L G(M) \qquad (45)$$

where P_M^L is the number of ways the number M can be constructed by adding together L positive integers not including zero. The P_M^L are binomial coefficients (Ref. 20)

$$P_M^L = \frac{(M-1)!}{(L-1)!\,(M-L)!} \qquad (46)$$

which gives upon substitution into Equations 43 and 45:

$$R^N = V_{TD}^N + \sum_{L=1}^{N}\sum_{M=L}^{\infty} \frac{N!}{(N-L)!\,L!}\ \frac{(M-1)!}{(L-1)!\,(M-L)!}\ (-1)^M V_{TD}^{N-L} D_{TD}^L D_{DT}^L V_{DT}^{M-L} \qquad (47)$$

It is noted that $V_{DT} = -V_{TD}$ and that the summations may be interchanged if N1 is denoted as the smaller of M or N:

$$R^N = V_{TD}^N + \sum_M U(M) \sum_{L=1}^{N1} \frac{N!}{(N-L)!\,L!}\ \frac{(M-1)!}{(L-1)!\,(M-L)}\ (-1)^M V_{TD}^{N-L} D_{TD}^L D_{DT}^L V_{TD}^{M-L} \qquad (48)$$

Equation 48 can be readily interpreted in terms of the diagrams of Figure 7, for the case of N = 3 trips through the delay line. Since U(M) is the operator which shifts time be a factor of $2M/V_T$, a given value of M describes the collection of terms for a time shift of $2M/V_T$ and that collection of terms is given by the finite summation within the curly brackets. The binomial coefficients give the correct number of ways that reflections and transmissions can occur. The quantity $(-1)^L$ accounts for phase change on reflection at the transducer-air interface. The attenuation and transmission coefficients properly account for changes in amplitude on transmission and reflection.

The advantage of Equation 48 is that is may be readily evaluated numerically for hundreds of trips through the delay line. Further, the results of Equation 48 are directly applicable to the output of a matched filter. If the exact form of the initial signal is specified, the results of Equation 48 can be used to construct the output waveform after N trips through the delay line. The terms of Equation 48 are written out below for N = 3, three trips through the delay line, and for the first four pulses of the infinite series.

44

$M = 0 \quad V_{TD}^3$

$L = \quad 1 \qquad\qquad\qquad 2 \qquad\qquad\qquad\qquad 3$

$M = 1 \quad -3V_{TD}^2 D_{TD} D_{DT}$

$M = 2 \quad + 3V_{DT} V_{TD}^2 D_{TD} D_{DT} \qquad + 3V_{TD} D_{TD}^2 D_{DT}^2$

$M = 3 \quad -3V_{DT}^2 V_{TD}^2 D_{TD} D_{DT} \qquad -6V_{DT} V_{TD} D_{TD}^2 D_{DT}^2 \qquad -D_{TD}^3 D_{DT}^3$

$M = 4 \quad + 3V_{DT}^3 V_{TD}^2 D_{TD} D_{DT} \qquad +9V_{DT}^2 V_{TD} D_{TD}^2 D_{DT}^2 \qquad + 3V_{DT} D_{TD}^3 D_{DT}^3$

Comparison of these expressions with Figure 18 shows the one-to-one correspondence between the diagrams and the terms of Equation 48.

.hen impedances are nearly matched, $V_{DT} = -V_{TD} << 1$ and D_{TD} and $D_{DT} \approx 1$. The term for which $L = M = N$ has been called the main term of the nearly matched case because it is the pulse which has been transmitted through the transducer once for each passage through the delay line. It is the only term completely independent of V_{TD} and V_{DT}, having the form $D_{TD}^N D_{DT}^N$. For small N it will be the dominant term in the series. However, as N becomes very large the multiplicative factorial expressions become large, because they account for the number of ways the other terms can occur. The ratio of the next largest term in the sequence of terms for $M = N$ to the main term is

$$\frac{NV_{TD}}{D_{TD}D_{DT}} \qquad\qquad (49)$$

These ratios suggest that if

$$NV_{TD} < 1 \qquad\qquad (50)$$

then the main term will dominate others in the train of pulses. The impedance mismatch, I, is twice the reflection coefficient:

$$I = \frac{2|Z_2 - Z_1|}{Z_2 + Z_1} = 2V_{TD} \qquad\qquad (51)$$

A useful criterion for dominance by the main term is that

$$NI = 1 \qquad\qquad (52)$$

or in words, a 1-percent impedance mismatch results in one dominant term in the pulse train and little distortion for one hundred or less trips through the delay line. In Figure 19, results are plotted for the case of N = 100 trips with a 1-percent impedance mismatch. The horizontal time axis is in units of the delay

time, T; because of transit through the transducer, $T = 2d/V_T$. Time is taken as zero for the main term, $L = M = N$. The sum of all terms for a given time delay, M value, is plotted vertically as an amplitude for that time delay. The incident signal is assumed to have unity amplitude. A verbal interpretation of Figure 19 follows in the next paragraph.

N = 100 TRIPS

1% IMPEDANCE MISMATCH, I = 0.01

TIME OF OUTPUT FROM THE DELAY LINE IN UNITS OF DELAY TIME, T, OF THE TRANSDUCER
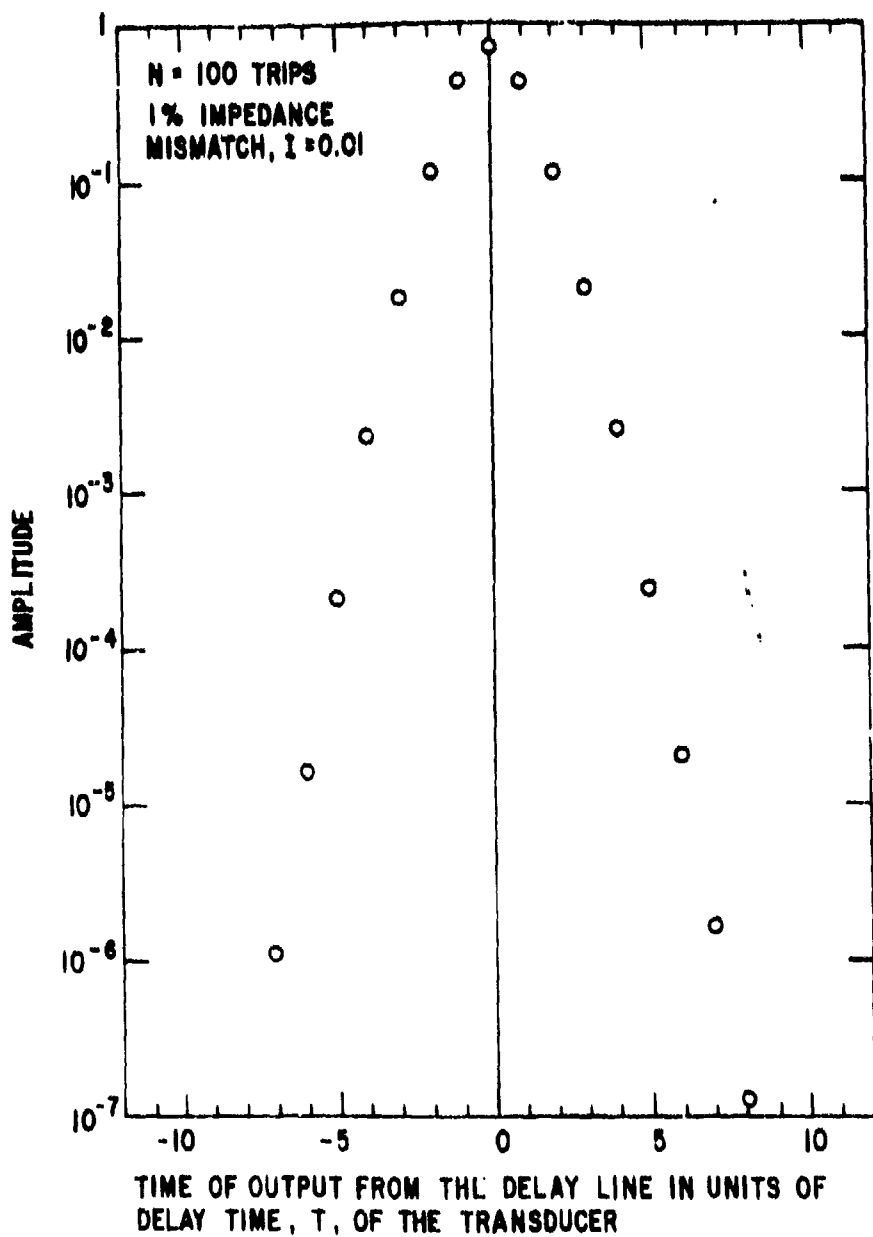
Figure 19. Amplitude Versus Time of Output for 100 Trips Through the Delay Line. Calculated for 1-Percent Mismatch of Impedance Between Transducer and Delay Medium

A coded signal of unity amplitude is stored in a delay line memory device with a 1-percent impedance mismatch between the delay medium and the transducer. Because of reflections at the interface of the transducer and delay medium, the single signal becomes an infinite train of duplicate signals, separated from one another by the transit time T through the transducer. The largest of these signals has an amplitude of 0.76. It is preceded and followed at a time interval T by signals of amplitude 0.44 and at a time interval of 2T by signals of amplitude 0.1; at a time interval 3T it is preceded by a signal of amplitude 0.019 and followed by a signal of amplitude 0. 020; and so on. Note that only the points at integral multiples of T can have any meaning. In subsequent graphs the points are joined with continuous curves to aid the eye in following from point to point, but only the points have any meaning.

In Figures 20 and 21, amplitude is plotted versus delay time, T, for signal trains that result from 100 trips through the delay line for impedance mismatches of 0.1, 1, 2, 3, 4, and 5 percent. One sees that for 0.1-percent and 1-percent mismatch, the M = N (time 0) signal is largest and the other signals decrease in amplitude monotonically with time difference. For a mismatch of 2 percent or greater, the M = N signal is not the largest and the amplitudes are appreciable, yet variable in magnitude, for an appreciable number of time delays. The criterion of Equation 52 which states NI = 1 for dominance of the M = N signal is verified. In addition, one can define a useful width parameter, W, as the number of delay times, T, encountered before the signal level drops by a factor of 3 and continues to decline monotonically. For small values of mismatch it is found empirically that

$$W = 3IN \tag{53}$$

Beyond this width the signals in the train drop in power by about 10 decibels per delay period T.

The form of Equation 52, NI = 1, suggests that the shape of the amplitude versus T curves should be dependent principally upon NI. As one varies N and I, keeping the product fixed, one would not expect the details of amplitude variation near T = 0 to be reproduced, but would expect the regions of the curves that decrease monotonically to reproduce. This is shown to be the case in a series of calculations for particular combinations of transducer and delay line materials.

The impedances and the mismatch of impedances for $LiNbO_3$ and for quartz are given in the matrix of Table 6. Lithium niobate is chosen as an example because of the available piezoelectrics it most closely matches the impedances of the low-loss delay media for shear modes. Quartz is used as an example because of its availability, frequent use, and poor impedance match. The mismatch to $LiNbO_3$ can be reduced if the level of effort entailed is warranted. The impedance can be lowered somewhat by carefully exploring rotated cuts, with due regard to the effective coupling coefficient and the generation of spurious modes. The impedance can be raised by growing mixed crystals with $LiTaO_3$.

47
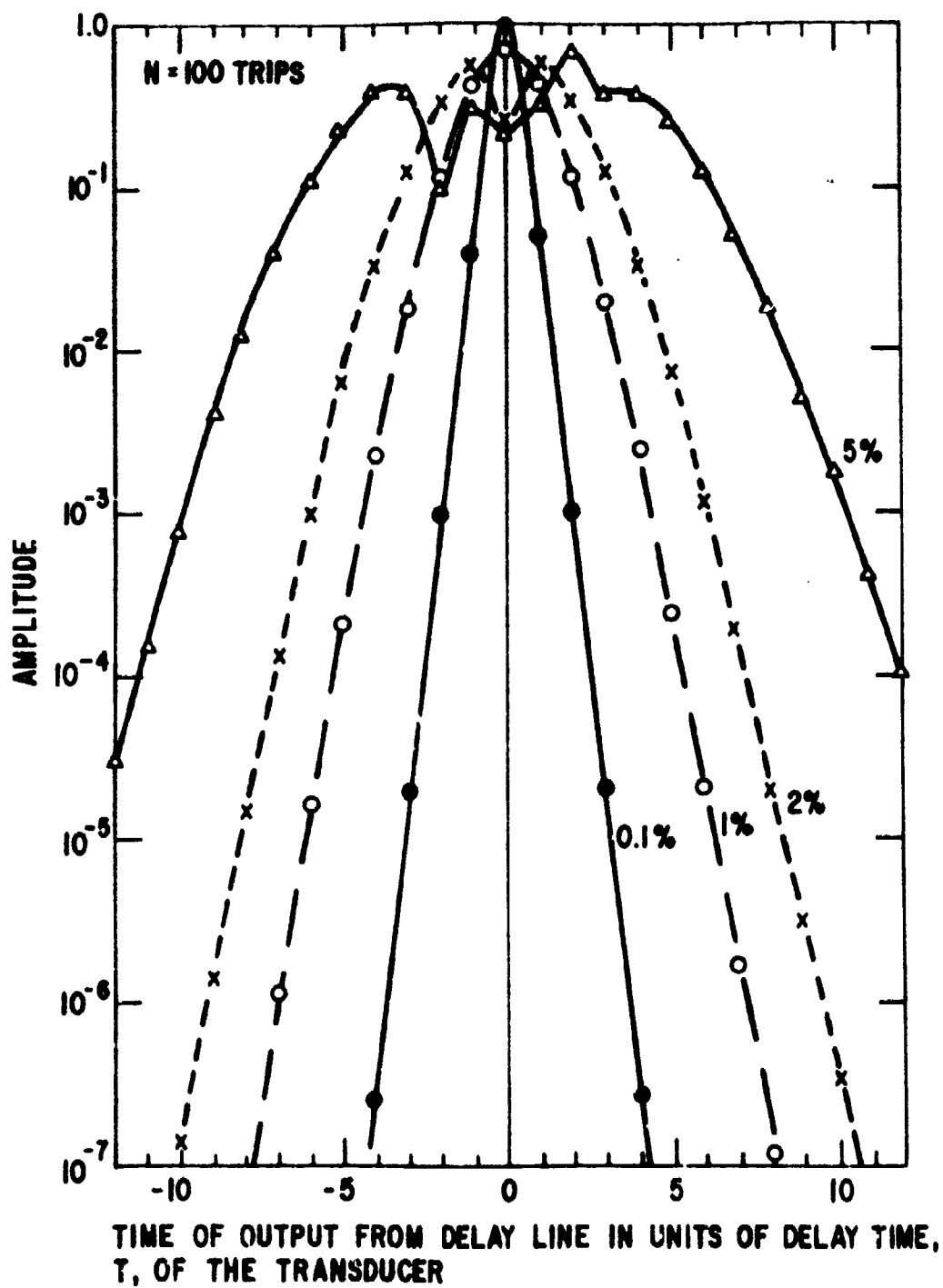
Figure 20. Amplitude Versus Time of Output for 100 Trips
with 0.1, 1, 2, and 5 Percent Impedance Mismatch

48
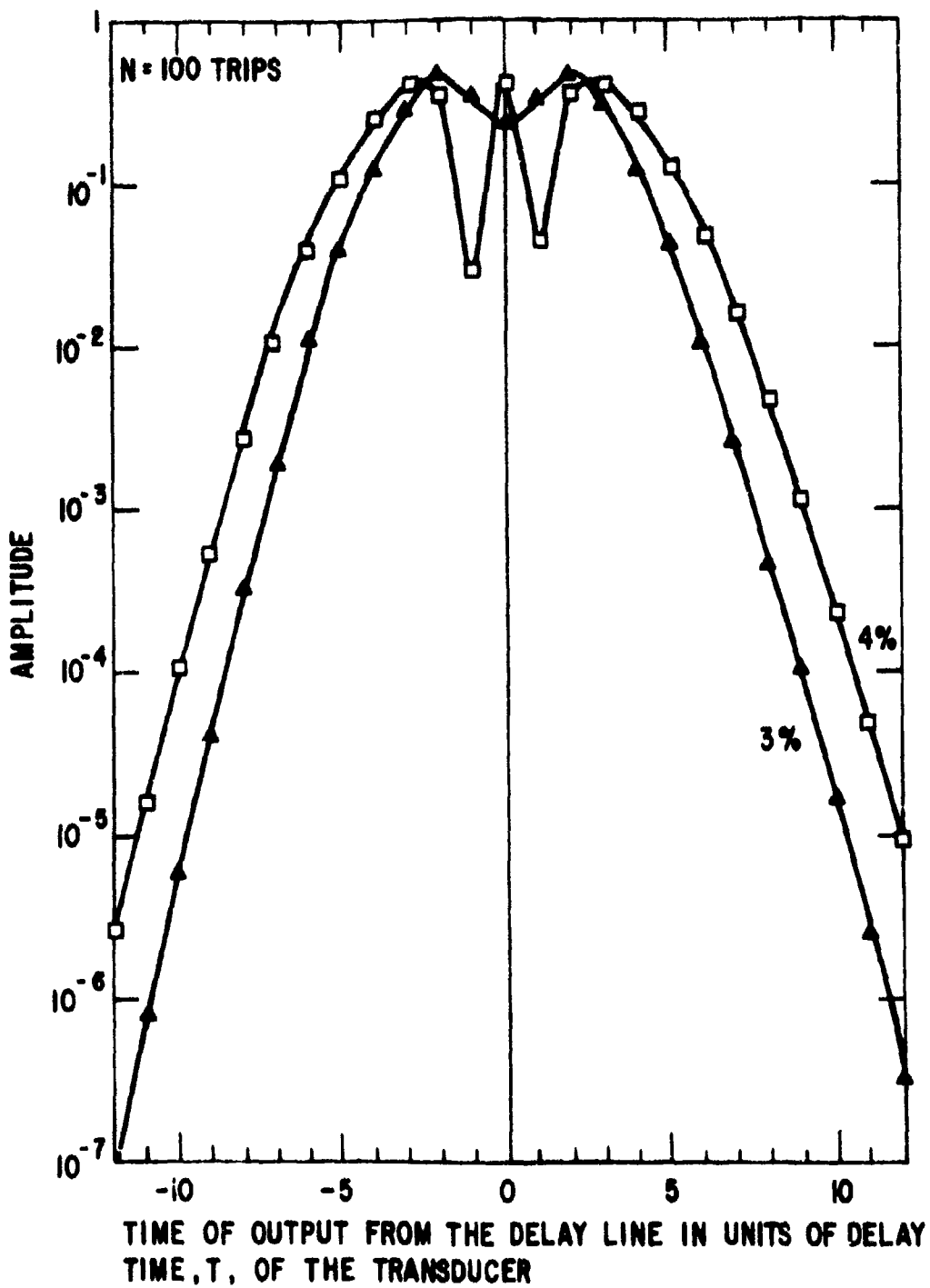
Figure 21.   Amplitude Versus Time of Output for 100 Trips
with 3 Percent and 4 Percent Impedance Mismatch

In Table 6 the acoustic impedances were taken from Tables 1 and 3. For $YB_{.6}$ the impedance value used was 20.2×10^6 gm/sec cm^2.

Figure 22 shows a plot of amplitude versus time for LiNbO$_3$ on MgAl$_2$O$_4$. The number of pulses has been chosen to provide NI products of 1, 2, and 3 for comparison with Figures 20 and 21. One finds close similarity in the shape of the curves for constant NI product, verifying the usefulness of Equations 52 and 53. Figure 23 shows similar results for LiNbO$_3$ on Y$_3$Al$_5$O$_{12}$; Note that

<div align="center">

Table 6

PERCENT IMPEDANCE MISMATCH
OF TRANSDUCERS AND DELAY LINES

</div>

Element	LiNbO$_3$, X-cut	SiO$_2$, Y-cut
MgAl$_2$O$_4$	3.4 %	70 %
Y$_3$Al$_5$O$_{12}$	1.3 %	78 %
YB$_{.6}$	11 %	67 %

<div align="center">
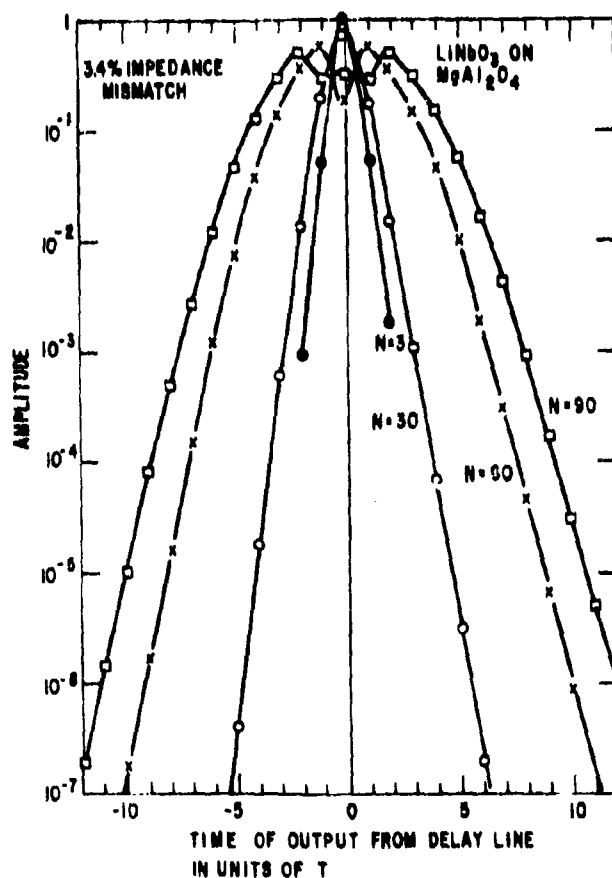
Figure 22. Amplitude Versus Time of Output for LiNbO$_3$ Transducer
on MgAl$_2$O$_4$ for 3, 30, 60, and 90 Trips

</div>
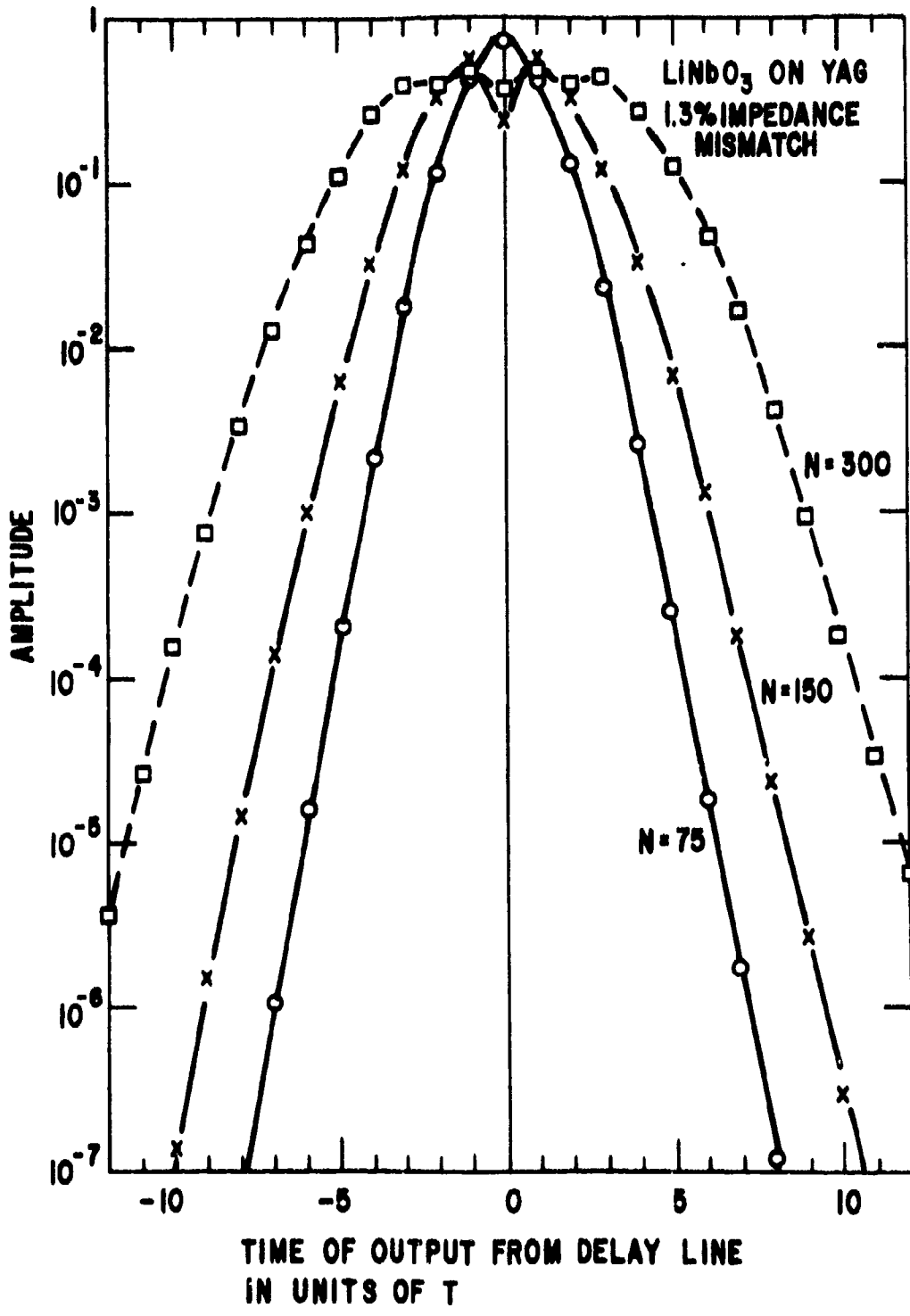
Figure 23. Amplitude Versus Time of Output for LiNbO₃ on YAG
for 75, 150, and 300 Trips

the close impedance match provides N = 75 trips before the condition NI = 1 is reached. In Figure 24 a similar plot is given for LiNbO₃ on YB₆₆. In this case the NI = 1 condition is reached for only nine trips of the signal through the delay line. In Figure 25 the cases of 2, 3, and 10 trips are shown for SiO₂ on MgAl₂O₄. In spite of the good insertion loss and bandpass characteristics of this combination, the poor impedance match makes it a poor choice for memory of coded signals for any number of trips through the delay line.
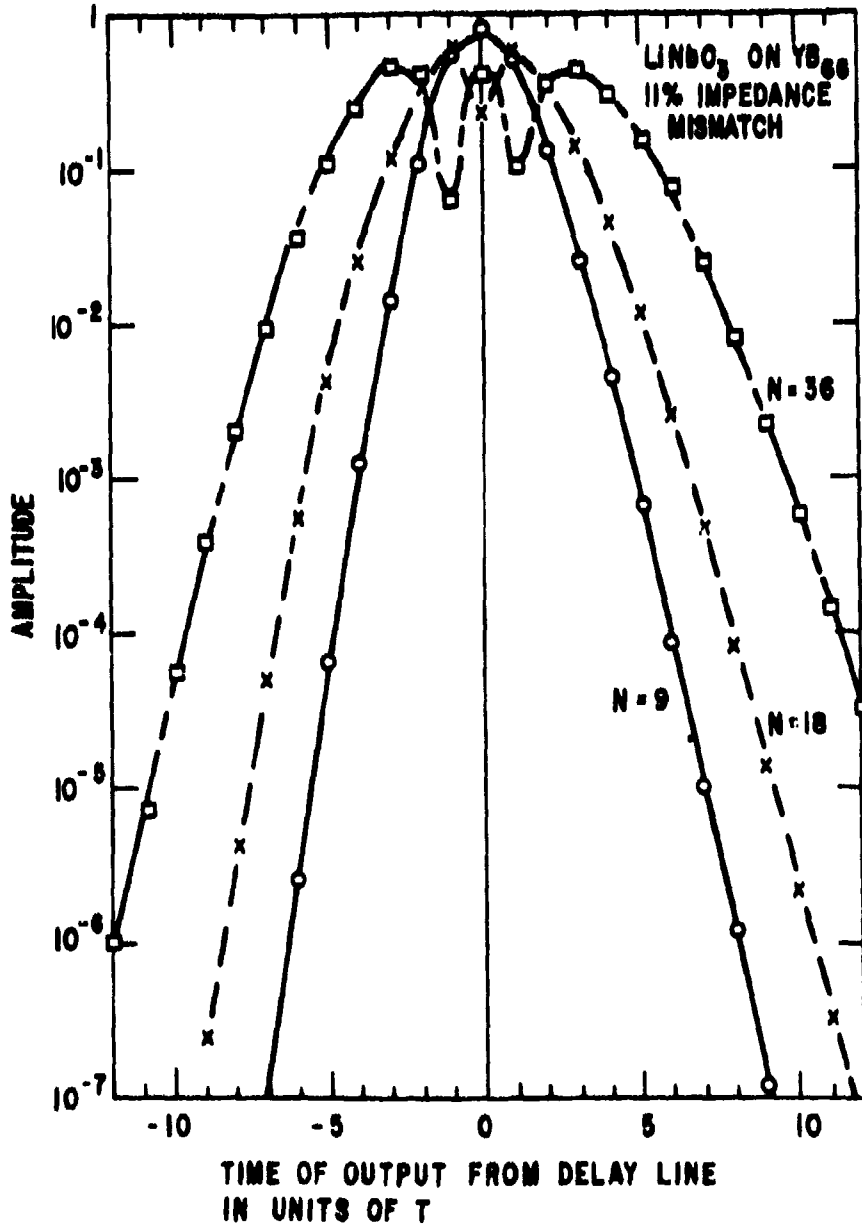
Figure 24. Amplitude Versus Time of Output for LiNbO₃ on YB₆₆ for 9, 18, and 36 Trips
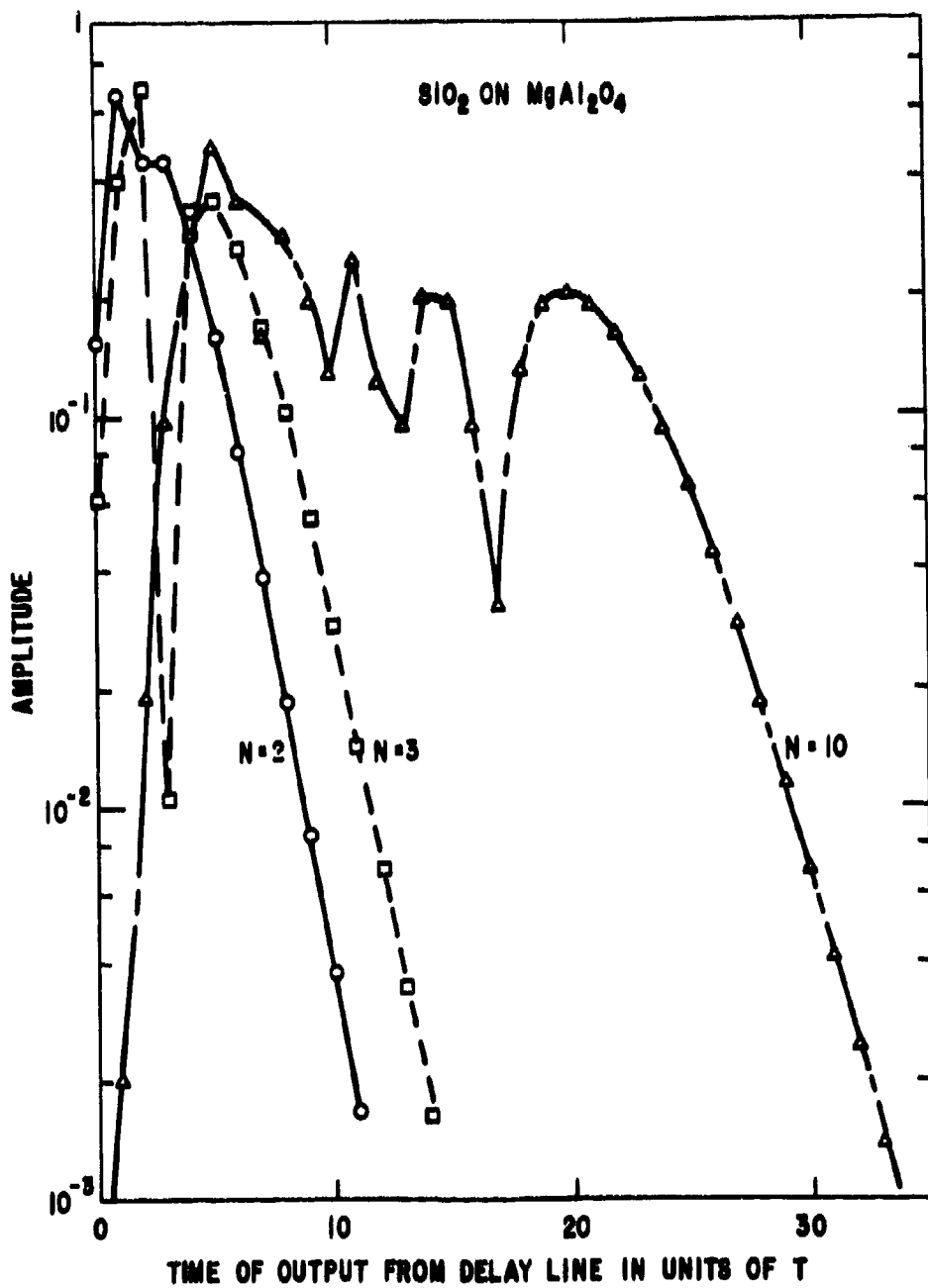
Figure 25.   Amplitude Versus Time of Output for SiO$_2$ on MgAl$_2$O$_4$
            for 2, 3, and 10 Trips

Summary and Conclusion

Impedance matching of transducer and delay media is important in order to minimize distortion of stored coded signals. An expression has been provided in Equation 48 for calculating the effects of the impedance mismatch in detail. Two simple criteria, Equations 52 and 53, are given for estimating the degree of impedance matching required to meet a system specification. The allowable distortion on the output of the matched filter must be specified for the system of interest if the degree of impedance matching is to be calculated for the memory element.

The constraints of impedance matching do not create problems in the insertion loss characteristics of the delay lines. The diameter of the transducers must be kept large in order to minimize diffraction losses and provide long delay times. The large area and high dielectric constant result in a very low electrical impedance for the transducer. In addition, the conversion efficiency of $LiNbO_3$ is too high for long memory times. Figure 26 shows calculated values of insertion loss versus frequency for a delay line of $MgAl_2O_4$
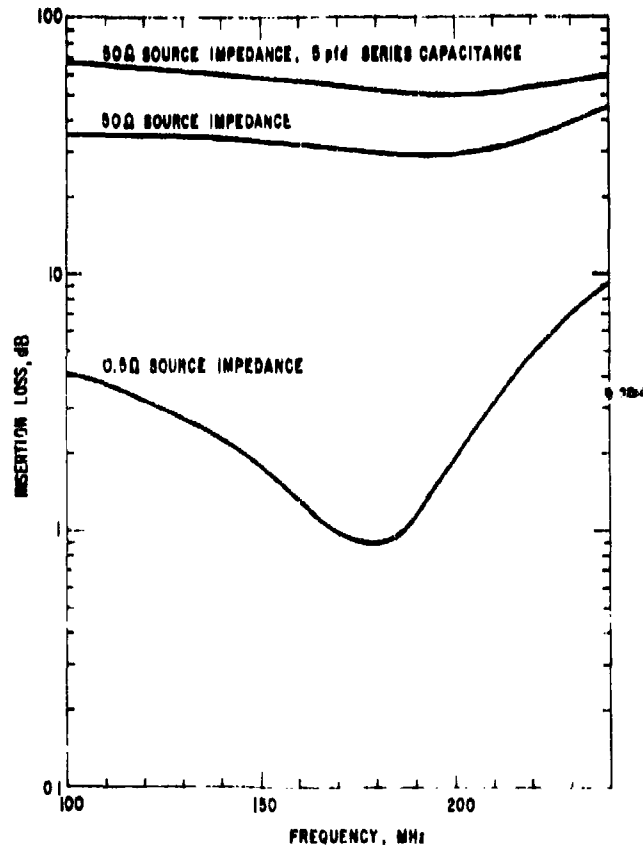
Figure 26. Insertion Loss Versus Frequency for $LiNbO_3$ on $MgAl_2O_4$ with Source Impedance and Series Capacitance Varied

with an X-cut LiNbO₃ transducer centered at 200 MHz bonded to it, with 1 μm of gold and 0.1-μm-thick gold top electrode. When driven from a low impedance, 0.5-ohm source this combination has a very low insertion loss, less than 1 decibel, and varies in insertion loss by less than 4 decibels over a 100-MHz bandwidth. When driven from a 50-ohm source the insertion loss variation with frequency does not change appreciably, but the minimum insertion loss is raised substantially, to 30 decibels.

Further control of the insertion loss can be attained by driving the transducer via a series capacitor. With 5 pfd of series capacitance the insertion loss is increased to about 50 decibels, without appreciable changes in the frequency dependence other than a slight increase in the frequency of minimum insertion loss. The use of series capacitance has been reported previously by Larson and Winslow (Ref. 2), who showed that a marked resonant effect on bandpass characteristics resulted. Their study involved X-cut LiNbO₃ bonded to rutile with indium. Unlike the present case, the transducer, bond, and delay line were badly matched acoustically. Resonance was observed when the delay line was mismatched both electrically and acoustically. The acoustic impedance matching required for memory of coded signals eliminates such resonant effects. Insertion loss characteristics may be tailored to needs by controlling the source impedance and by the addition of a series capacitance.

DELAY LINE FABRICATION

Fabrication of delay rods and transducer, deposition of metals for bonds and electrodes, bonding of the transducer to the delay line, and thinning of the bonded transducers have been explored experimentally. The selection of metals as bond and electrode materials is considered in this section. The relevant phenomena are indicated, a brief literature review and status of knowledge is given, and a practical system is described for simultaneously minimizing attenuation in the bond and matching impedances. A description is given of the equipment used and the general methods employed.

A. MATERIALS FOR METAL BONDS

There are several criteria to apply to metals which are to be used for bonds:

● Ease of thermocompression bonding

● Matching acoustic impedance

● Minimizing sound attenuation

Ease of forming a bond has been found (Ref. 21) to correlate with yield stress of the material. Thus the ductility of the crystal lattice is an important factor, and this decreases as one goes through the sequence FCC: BCC: HCP. This criterion points to the use of metals with the FCC copper structure.

The acoustic impedances of several of the materials of interest are listed in Table 7. The delay media and the transducer material have impedances in the range of 20.2 to 23.4 $\times 10^5$ g cm/sec. The metals listed have the desired

Table 7

SHEAR MODE IMPEDANCES

Material	$\bar{Z}$	Z_{111}	Z_{110}	Z_{100}	$\bar{Z}_{pp}$
Gold	24.0	22.4	24.8	20.7	18.6
Palladium	24.6	22.9	26.6	20.5	19.1
Silver	17.7	--	--	--	--
$MgAl_2O_4$	--	--	--	23.4	--
YAG	--	--	--	22.9	--
LiNbO$_3$	--	--	--	22.6	--
YB$_{66}$	--	-	--	20.2	--

Units of impedance values 10^5 gm/cm^2 sec.

FCC copper structure and form solid solutions over a large composition range. The columns labeled Z_{111}, Z_{110}, and Z_{100} contain impedances for shear waves propagating in the [111], [110], and [100] crystallographic directions, respectively. The column headed Z gives the value of impedance for a polycrystalline sample with random orientation of grains. From Table 7 one sees that the impedances of all of the oxide crystals can be met with alloys of the Pd-Au-Ag system if the alloy has a random grain structure.

In the work of Larson and Winslow (Ref. 2) with gold films, the films were found to have a [111] texture and an impedance of 22 percent less than the value for bulk gold. The exact causes of the discrepancy are not understood and may involve such factors as the extent of interdiffusion during ultrasonic welding, the density of the deposited metal, and the details of extracting the velocity and attenuation of sound in gold from the insertion loss data. The effect of a 22-percent impedance reduction $\bar{Z}$ is shown in the column labeled $\bar{Z}_{\bullet}$. One would expect a somewhat reduced impedance in comparing a deposited film with a single crystal. Whether a 22-percent reduction in impedance for a thin metal film is realistic and a limit to what can be achieved is under investigation. Even if this is the case, the Pd-Au system offers several advantages.

The deposition of an alloy makes it easier to obtain a film with random orientation of grains, with an increase in impedance as a result of a random texture, $\bar{Z}$, rather than a [111] film texture, Z_{111}. Because alloys of gold and palladium follow Vegard's law to within a few percent (Ref. 22), density varies nearly linearly with alloy composition. However, the torsion modulus does not vary linearly with composition (Ref. 23); as a result, the acoustic impedance of alloys is greater than that of either component, as shown in Table 8. Other elements may be added to the Pd-Au system. Additions of silver can be made over wide composition ranges to reduce impedance. Over restricted composition ranges, additions of platinum, rhodium, and iridium can be made, and the latter should be useful in increasing film impedance.

Table 8

SHEAR MODE IMPEDANCES OF Au-Pd ALLOYS

Atom Percent Palladium	$\bar{Z}$
0	24.0
8.86	24.6
17.0	25.0
31.6	26.6
41.2	27.2
49.9	27.8
100	24.6

Units of impedance values 10^5 gm/cm^2 sec.

58

The third criterion for the selection of a metal system to be used as a bond is minimization of sound attenuation in the bond. Attenuation in such metals arises from four causes: 1) scattering of sound by the crystal grains, 2) dislocation attenuation of the sound wave, 3) attenuation of the sound wave by electrons, and 4) attenuation of the sound wave by phonons. It is shown here that these effects are minimized by use of an alloy. Attenuation by scattering from crystal grains is small for the metal thicknesses contemplated, and is minimized by deposition procedures which can readily produce films of metal with grains much smaller than an acoustic wavelength. Attenuation by phonons is not an appreciable fraction of the attenuation in the delay medium. However, attenuation due to dislocations and to electrons can be appreciable.

Mason and Rosenberg have studied attenuation in aluminum (Ref. 24), cadmium and copper (Ref. 25), and lead (Ref. 26). They show that the attenuation can be separated into a portion, Γ_{f}, which is caused by electrons and varies quadratically with frequency, and a portion, Γ_{D}, which is caused by dislocations and follows a normalized loss curve. Typically, dislocation losses dominate at frequencies up to a few hundred MHz, and electron damping dominates in the GHz frequency range. The electron related attenuation, Γ_{f}, was shown to be proportional to

$$\Gamma_{\mathrm{f}} \sim \omega^2 \sigma / \rho V^3 \tag{54}$$

where

ω = angular frequency
σ = electrical conductivity
ρ = density
V = sound velocity

The electrical resistivity of gold-palladium alloys has been measured (Refs. 23-27), and values (Ref. 23) are quoted in Table 9.

Table 9

CONDUCTIVITY OF AU-PD ALLOYS AT 0° C

Atom Percent Palladium	10^6 mho/m
0	44.1
8.86	17.7
17.0	11.1
31.6	7.41
41.4	8.37
49.9	4.20
60.2	3.58
70.2	3.84
81.2	4.69
91.3	6.21
100	9.70

The extant data for shear wave attenuation in gold films is that of Larson and Winslow (Ref. 2) for films of [111] texture. They find a value of 1000 dB/cm at 1 GHz, and at that frequency the attenuation is expected to be dominated by interactions with electrons. From Table 9, then, it is apparent that Γ_e for Au-Pd alloys can be as low as 100 dB/cm. This factor of ten lowering of attenuation reduces to a negligible amount the contribution of the bond to total delay line attenuation. The contribution of a gold layer to total attenuation can be comparable to that of a low-loss delay medium such as $MgAl_2O_4$.

The attenuation due to dislocations, Γ_b, can be appreciable. The available experimental results (Refs. 24-26) separate these losses from electron damping and provide values for the dislocation drag coefficients in the metals studied. They do not provide useful means for predicting dislocation damping in other materials. However, Cain and Thompson (Ref. 28) have studied sound velocity in Cu-Al alloys. In that study they note that the dislocation attenuation in the alloys is substantially lower than in pure copper, as a result of pinning of dislocations. This result is expected from known properties of dislocations. One expects reduction in Γ_b by orders of magnitude in going from pure gold to Pd-Au. Data are not available for making a quantitative estimate of the effect of alloying on Γ_b.

The advantages of the Au-Pd-Ag system for acoustic bonds are summarized as follows. This system permits acoustic impedance matching to the low-loss crystals of interest. Metal films can be deposited with fine, randomly oriented grains. Attenuation due to electrons can be reduced to a tenth that of gold, and attenuation due to dislocations can be markedly reduced. Quantitative estimates of the latter are not available.

B. FABRICATION EQUIPMENT

Metal deposition is carried out by evaporation or sputtering. The apparatus used for diode or triode sputtering, shown in Figure 27, consists of two stainless steel stations and control circuitry. The vacuum stations use copper gaskets and graded metal-to-glass seals exclusively. Each station is pumped by a mercury diffusion pump, which is isolated from the station by two glass liquid nitrogen traps. The mechanical roughing and backing pump is isolated from both the diffusion pump and the system by a glass liquid nitrogen trap filled with copper. The stations routinely reach 10^{-7} torr prior to backfilling with gas for sputtering.

The bonding of a transducer to a delay rod has been carried out in a number of ways, such as the use of low-melting-point solders (Ref.29), cured varnishes (Ref. 30) or epoxies (Ref. 31), thermocompression welding (Ref. 2), and ultrasonic welding (Ref. 2). These methods have been reviewed and extended by Larson and Winslow (Ref. 2). Electric field assisted bonding (Refs. 32 and 33) may be applicable but has not been explored. Preliminary experiments with
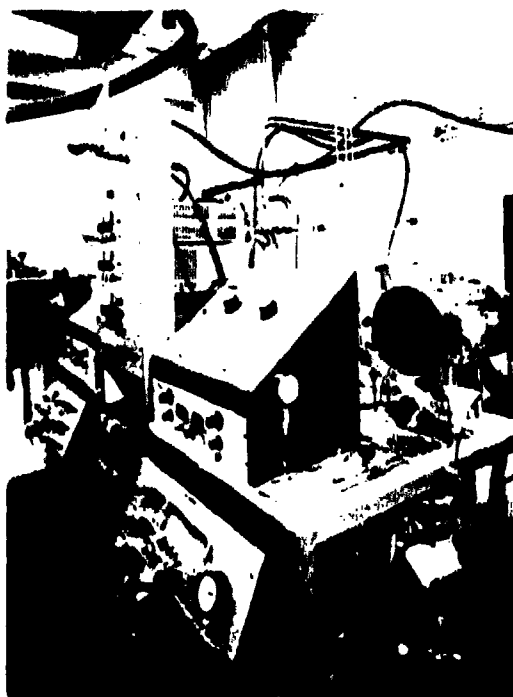
Figure 27. Sputtering System, D-C Diode or Triode Operation

ultrasonic bonding indicated that this method would not be practical for large-diameter transducers unless thick metal films, an appreciable fraction of an acoustic wavelength in thickness, were used. With thin films, excessive pressures were required to form a bond by the ultrasonic technique. Thermo-compression bonding also requires high pressures (Ref. 34) when performed in air. When carried out in vacuum, substantially lower pressures are adequate (Ref. 21).

Therefore a thermocompression bonding system has been built which operates inside a vacuum system. In this system the top surface of the delay line rod and what will eventually be the bottom surface of the lithium niobate transducer are held in a jig, in a coplanar position, underneath a metal evaporation source. The jig is held in a motor-driven rotating disk. The motor is shown in the upper portion of Figure 28. The jig is shown as two square holes just to the left of center in Figure 28; one square hole holds the rod, the other holds the transducer.

In the first position of the disk, a thin chromium film is evaporated onto both the rod and the transducer. The disk is then rotated to a second position in the bell jar, where a second thin metallic film, perhaps silver, is evaporated onto both the rod and the transducer. In the third position the transducer plate is inverted by means of a hinge built into the jig so that the metal-coated face of the transducer now lies on top of the delay line rod. It is also accurately centered over the rod.

61
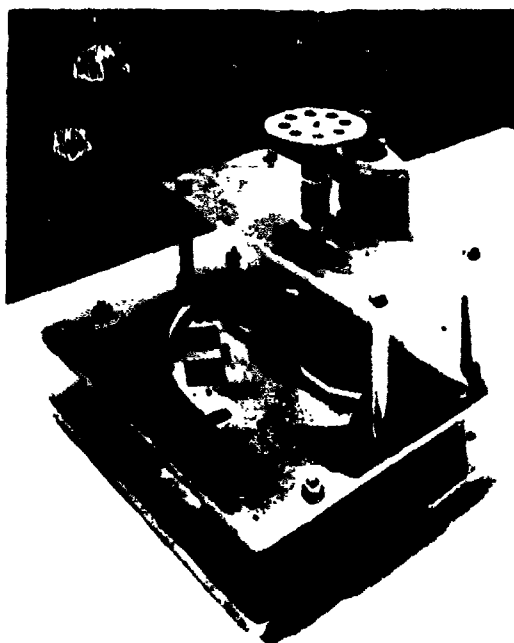
Figure 28. Substrate Carrier for Depositing Metals and Bonding
Transducers in Vacuum

In the fourth position the transducer-metal film-rod sandwich is placed
between the jaws of a vise which is operated by an hydraulic ram. This ram
is actuated from outside the vacuum chamber by a piston pump which pres-
surizes the oil inside a stainless steel line leading into the vacuum chamber
and then to the ram.

A collection of power feedthroughs, hydraulic cylinder, ram, and so forth
for use with the vacuum system is shown in Figure 29. Experiments have
shown that close alignment of the transducer, delay rod, and ram surfaces
are essential if forces are to be evenly distributed so that the transducer will
not fracture. This alignment requires both a rotation and translation of the
ends of the delay rod. Thin shims of teflon have been used successfully to
provide the required motion.

This present bonding is all done at room temperature. Once the sand-
wich has been pressurized and the metal bond is secure, the pressure is re-
leased and the transducer is ready for the next step. This step is thinning of
the transducer so that it will resonate at the appropriate frequency. This
thinning must be done after the bonding, because a transducer of the resonant
thickness would crack easily under the bonding pressure. The vacuum sta-
tion, as shown in Figure 30, is equipped for RF sputtering of insulators, and
it can be used in this mode for thinning of bonded transducers. The bonded
transducer can also be thinned by a mechanical process of grinding and polishing.
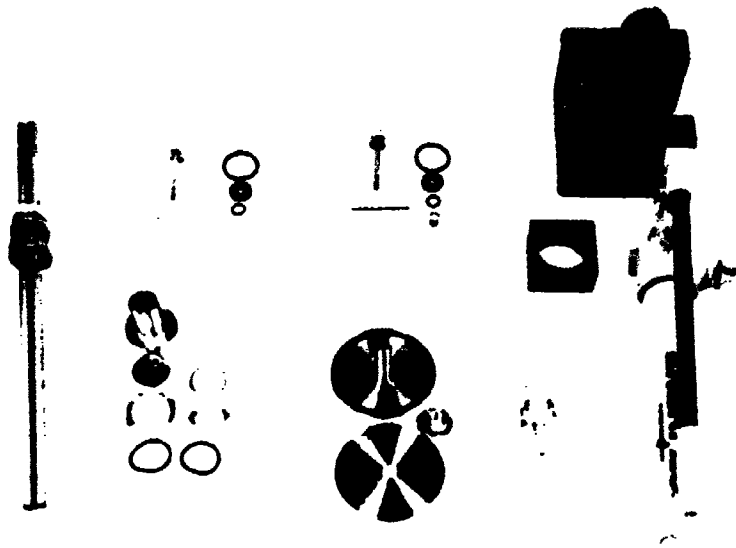
Figure 29. Parts for Vacuum-Bonding Station
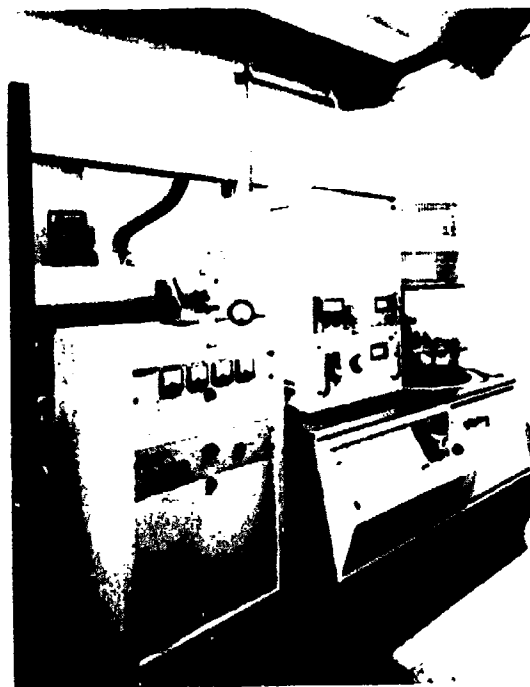
Figure 30. Vacuum Station for Bonding or RF Sputtering

A mechanical system for thinning transducers is being developed using techniques similar to those of Twyman (Ref. 35). In this apparatus, however, metal laps replace the pitch laps of Twyman. The machine is built from a precision computer disk memory drive unit and is shown in Figure 31. Diamond is embedded in the metal laps and a rotating sponge collects loose particles from the lap. Figure 31 also shows the box which houses the laps for different grades of diamond, one of the large polishing blocks, and a large-diameter optical flat used to simultaneously evaluate the condition of the lap and the sample. Aluminum laps have proven to be satisfactory for diamond of 3-μm size and above, but they induce scratching when used with finer grades of diamond. Copper laps have been prepared for use with 1-μm and 1/2-μm grades of diamond.
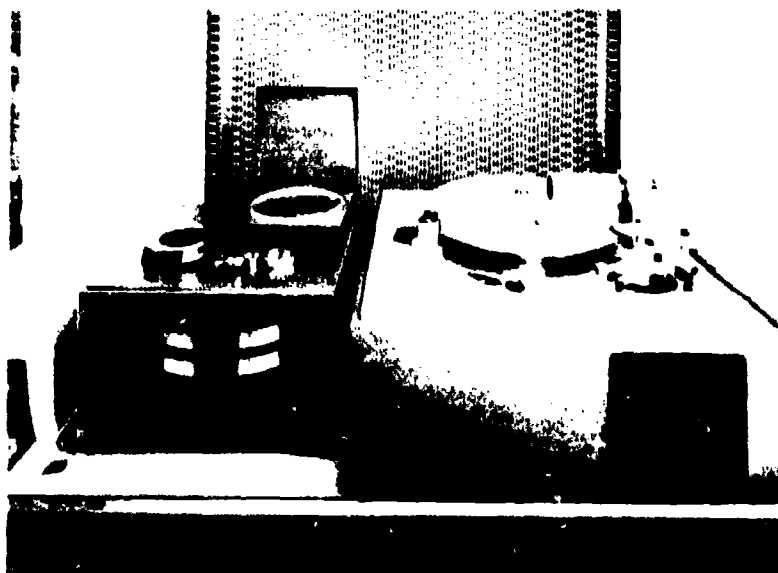
Figure 31. Polishing Machine

C. UNDOPED SPINEL CRYSTALS WITH LITHIUM NIOBATE TRANSDUCERS

The most promising material to date for fabrication of low-loss acoustic delay lines at a frequency of 200 to 300 MHz is spinel ($MgAl_2O_4$). The design of the transducer-bond-crystal sandwich for $MgAl_2O_4$ using a $LiNbO_3$ piezoelectric transducer has been described in Section 2 ("Delay Line Design"). A nearly optimum design is the use of an X-cut $LiNbO_3$ crystal with a thickness of 1/2 wavelength to generate shear waves at 200 MHz; this will be 12 microns thick. It is to be bonded to one end of a spinel crystal rod, which has a [100] axis along the length of the rod, by the use of a pure silver or gold bond. The metal bond thickness should be considerably less than 1/2 wavelength thick; this means preferably of the order of 0.5 micron thick.

64

Two boules of Czochralski grown spinel were purchased from Crystal Technology, of Mountain View, California. One was grown with a [111] axis and was 10 cm long and 3 cm in diameter. The other was grown along a [100] axis, and was 5 cm long and 3 cm in diameter. These boules were scanned with a visible light beam when immersed in an index-matching fluid in order to select regions with a minimum number of light scattering centers. A total of six separate crystal rods were cut from the boules, two from the [100] boule and four from the [111] boule. The rods were about 1 cm in diameter and 0.8 to 2.5 cm long; they were all cut with a [100] crystallographic direction along their length. These rods were centerless-ground and then sent to the Adolph Meller Company, in Providence, Rhode Island, where the end faces were carefully ground and polished to be optically flat and parallel.

Shear wave transducers of X-cut $LiNbO_3$ 0.95 cm in diameter and 125 μm thick were purchased from the Valpey-Fisher Corporation, in Hopkinton, Massachusetts. The procedure is to compression-bond these transducers to the spinel crystals in vacuum, using evaporated metal films on the two opposing faces. Once bonded, the exposed face of the transducer is to be ground and polished by removing about 113 μm of material, thus attaining the desired 1/2 wavelength thickness. This polished face will then be covered with an evaporated metal contact, to act as a second electrode. The special Twyman-type grinding and polishing machine was used to remove the requisite amount of $LiNbO_3$ and keep the polished face flat and parallel. This was installed in a laminar-airflow hood in order to keep room dust out of the system.

Some grinding experiments on fused quartz rods and plates were run with this machine. The grinding was done with 6-μm-diameter diamond powder embedded into the surface of an aluminum wheel. The wheel was 30 cm in diameter and 2.5 cm thick, and rotated at a speed of 30 rpm. At a vertical pressure of 2×10^5 dynes/cm^2 the quartz removal rate was 1.1 μm/min. Finer grinding was carried out with a similar copper wheel, using embedded 1-μm-diameter diamond powder. The cutting rate, at a pressure of 2×10^5 dynes/cm^2, was 0.12 μm/min. Somewhat similar grinding rates can be anticipated for $LiNbO_3$. The grinding rates were measured using comparison standards of metal gage blocks and a precision dial indicator made by the Federal Products Corporation (Providence, Rhode Island). The rates were found to be reproducible. One problem encountered in the reproducibility was to find a mounting wax for the spinel or quartz rods that would not cold-flow during the grinding and measuring operation, but that also had a low enough melting point to enable the rods to be mounted in the brass polishing jig. The best was found to be Jeweler's Special Wax made by the Princeton (Illinois) Sealing Wax Company.

D. METAL BONDING

The evaporator for the metal films in Figure 30 was evaluated with fused quartz test blanks. Chromium and then silver films were evaporated onto the quartz from tungsten wire filaments (Materials Research Corporation, Orangeburg, New York) in a vacuum of about 2×10^{-7} torr. The time and temperature were empirically adjusted so that in 15 minutes a 700Å-thick layer of chromium

was deposited. The sample was then rotated into the second section of the chamber, where 4000Å of silver were deposited in about 45 minutes time. The chromium layer thickness was measured, on a dummy substrate which was left unsilvered, by means of a Dektak™ profilometer. The silver layer thickness was measured by weighing a second dummy substrate, before and after evaporation, on a sensitive Mettler balance manufactured by Will Scientific, Inc., Rochester, New York.

After two fused quartz rods were coated with the double layer of metal film they were rotated to the third, and then the fourth, section of the vacuum chamber, where they were automatically positioned between the jaws of the hydraulic ram (Figure 29). The maximum pressure that could be tolerated by the 0.95-cm-diameter rods was about 2.2×10^9 dynes/cm^2 (32,000 lbs/in^2); at this pressure they invariably shattered. On smaller-diameter quartz rods pressure was occasionally run up to 3.6×10^9 dynes/cm^2 before shattering. As a rule, the compression bonding of quartz was attempted at about 2.0×10^9 dynes/cm^2. Of the three tries that were made, none was successful. The metal layers pulled away from the quartz, even though the quartz had been very carefully cleaned prior to the evaporation. The reasons for the lack of success are unclear. More work is needed to perfect this bonding technique.

™Trademark of the Sloan Technology Corporation, Santa Barbara, California.

Section 4

GROWTH AND CHARACTERIZATION OF YB$_{66}$ CRYSTALS

A. BACKGROUND

The Research and Development Center of the General Electric Company has supported efforts on understanding the theory of sound attenuation and on preparing, evaluating, and measuring the properties of crystals to develop useful microwave memory crystals and to test theory. This is borne out in the early reported work of Jacobsen (Ref. 36), Woodruff and Ehrenreich (Ref. 37), and other publications (Refs. 38 and 39).

Under U.S. Air Force Contract No. AF33(657)-8935, a systematic correlation (Ref. 38) was developed between microwave frequency sound attenuation in insulators and thermal properties of these cyrstals; particularly thermal conductivity and Debye temperature. This work made it possible to rank crystals in the order of their expected high-frequency acoustic attenuation using a parameter, designated R, which can be calculated from thermal properties such as thermal conductivity and Debye temperature. This ranking not only served to systematize available data but also afforded a means for predicting the acoustic loss of crystals whose acoustic properties have not been measured. Crystals which have low sound attenuation at microwave frequencies and room temperature were shown to be those with light mass atoms, complex crystal structures, high Debye temperatures, and low thermal conductivities. A basis was provided for:

- Selecting crystals for low sound attenuation at room temperature from thermal measurements.

- Selecting host crystals in which reduced acoustic attenuation, particularly near room temperature, might be achieved.

- Selectively doping or alloying the crystals to achieve a reduction of sound attenuation at room temperature.

Further support through U.S. Air Force Contract No. AF33(615)-2590 made it possible to refine the theory of microwave acoustic attenuation in crystals, to study the reduction of room-temperature sound attenuation by the presence of paramagnetic ions in spinel containing Fe^{3+}, to rank borides from thermal measurements, and to grow yttrium-aluminum garnet as a host crystal for further studies to reduce acoustic attenuation. Sapphire, yttrium-aluminum garnet, and magnesium aluminate spinel were identified as crystals with acoustic losses near the lower limit for oxides. Icosahedral boron compounds were identified as a system with potentially lower losses than the oxides, and YB$_{66}$ was selected as one of the best candidates among borides because of its unusual structure. Under U.S. Air Force Contract No. F33615-67-C-1399 (Ref. 40),

comparison of attenuation was made in $MgAl_2O_4$ spinel (Ref. 41) and in yttrium and rare earth garnets, and preliminary steps were taken to grow YB_{66} single crystals. Flux grown spinel, $MgAl_2O_4$ (Ref. 42) was shown to be the material with lowest acoustic attenuation at room temperature.

Further studies, under Contract No. F33615-69-C-1286 (Ref. 43) provided the first intercomparison of sound attenuation in very-low-loss materials grown by several different techniques. Comparisons were made among sapphire crystals grown by Verneuil, Czochralski, and chemical vapor deposition techniques, and $MgAl_2O_4$ spinel grown by flux evaporation and Czochralski techniques. Spinel, once again, was shown to be the lowest-loss material, but the Czochralski grown crystals available at that time were found to be unsatis-factory because of the high density of precipitates within them. The available flux grown crystals have been too small for many practical delay line require-ments. Recent developments in the growth of spinel as a substrate for silicon epitaxy have made it worthwhile to reevaluate Czochralski spinel as an acoustic delay line material.

Under Contract No. F33615-69-C-1286 (Ref. 43) methods were developed for synthesizing and growing single crystals of YB_{66} and the compound was shown to melt congruently. Attenuation measurements showed that a low-tem-perature relaxation process dominates the sound attenuation. No estimate of the thermal phonon related losses was possible because of the relaxation attenua-tion. The crystal stoichiometry, uniformity of composition in individual crystals, and purity were not under sufficient control to permit identification of the re-laxation mechanism. It was necessary to identify and eliminate the cause of the relaxation absorption so that the potential of YB_{66} as an acoustic material could be realized.

During the present contract the stoichiometry and purity of YB_{66} crystal has been examined. The compound has been shown to melt congruently at a composition near B/Y = 61.7. Small crystals of a number of compositions have been grown and characterized, including the congruently melting com-position. Precipitates of other Y-B phases have been identified in crystals of some compositions, and growth techniques have been adapted to eliminate them. The effort to grow larger crystals was warranted, and equipment modi-fications were made to scale up the length of the crystals grown. These results and characterization of the crystals are described in this section of the report.

In Section 2, the design study of delay lines showed that $MgAl_2O_4$ spinel was superior to other oxides as a delay line medium. To realize its potential it is necessary to (1) obtain large, high-quality boules, (2) provide shear mode transducers which can be manufactured reproducibly, and (3) to use electrodes with lower acoustic attenuation than the metals presently used. Since YB_{66} is potentially a lower-loss material than $MgAl_2O_4$, the three con-clusions above apply equally to YB_{66} once the relaxation losses are eliminated.

68

B. GROWTH METHODS

The synthesis and growth of single-crystal YB_{66} has been reported previously (Refs. 43-45). Since the techniques used are not widely applied they will be described here briefly to make the remainder of Section 4 more intelligible. Alterations of the growth procedures are described which will permit growth of crystals with improved uniformity with a composition very close to the congruent melting composition.

Synthesis

YB_{66} crystals are synthesized directly from the elements yttrium and boron. The reactivity of the components eliminates the use of heated ceramic or metal crucibles. Synthesis is complicated by the high heat of formation of an intermediate compound YB_4 which forms with explosive violence if the reaction rate is not limited by the synthesis technique. The material is synthesized in a water-cooled copper boat (Refs. 44 and 46). Heating is accomplished with RF induction, and coupling to the charge is initiated by preheating the charge to about 1000°C with a removable susceptor. Chemical interaction with the crucible is negligible (Refs. 44 and 47).

The exothermic formation of YB_4 is controlled by placing pieces of yttrium metal in appropriate quantity on blocks of boron, rather than by mixing the elements intimately. Upon heating, a molten pool of eutectic is formed. As the temperature is increased, YB_4 forms at the interface of the solid boron and the eutectic pool; its formation is readily observed from indandescence at the edge of the pool. In the geometry employed, the reaction rate is limited by diffusion of boron and yttrium and by the large heat flow to the water-cooled boat. Manual power adjustment is sufficient to control the reaction under these conditions.

Directionally Solidified Ingots

The reacted YB_{66} from the cold boat is polycrystalline, and it fractures on reheating. A pulling arrangement was added to the cold boat so that seeded ingots could be grown by the Czochralski method. These ingots are typically single-crystal but have appreciable mosaic structure due to the asymmetric temperature distribution of the cold metal boat system.

Pedestal Technique

Crystals for study are prepared by using the ingots pulled from the cold boat as pedestals (Refs. 45, 48, and 49). The ingots are supported from the lower end with a pyrolytic BN support. RF heating of the upper end of the ingot is initiated with a removable susceptor, the molten pool is seeded with a piece of single crystal, and the crystal is grown by passing the liquid region through the ingot. This procedure is equivalent to a single zone refining operation and has been advantageous in the studies of stoichiometry reported below.

The basic characteristics of the pedestal method can be understood by reference to Figure 32, a simple phase diagram for a two-component system which forms eutectics at compositions I and III and solidifies congruently -- liquid and solid have the same composition at composition II. The congruent melting composition need not correspond to ideal stoichiometry of the solid, though it is frequently close to the ideal composition. The structure of YB_{66} is sufficiently complex and the site occupation is partially statistical so that an ideal stoichiometry has never been previously defined. It has therefore been desirable to establish the congruent melting composition, to prepare
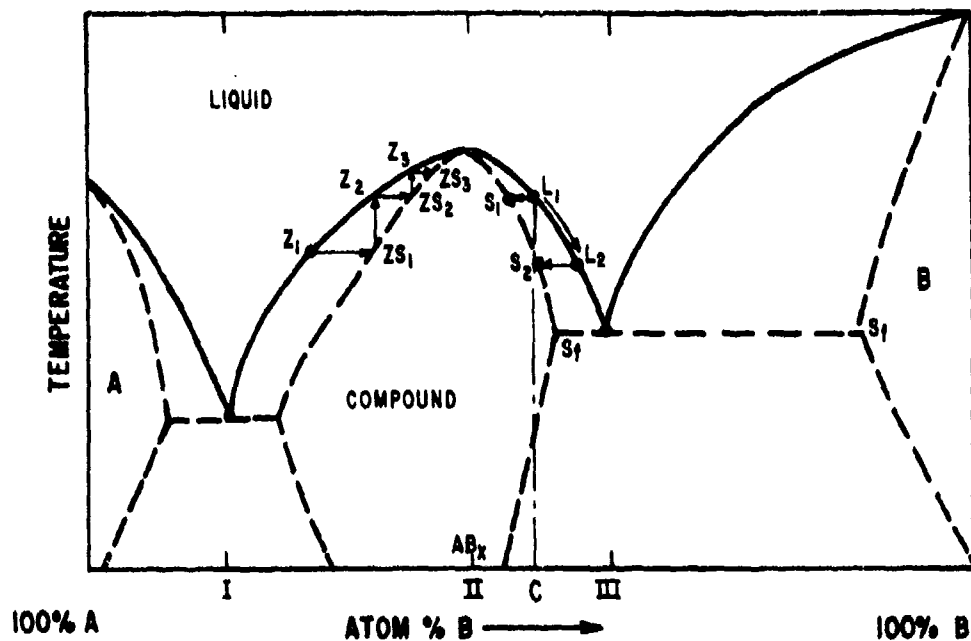
FOR YB_{66} $A \rightarrow YB_{12}$
                 $AB_x \rightarrow YB_{61.7}$
                 $B \rightarrow BORON$

Figure 32.   Binary Phase Diagram with Two Eutectics at I and III
              and a Congruently Melting Compound of Composition
              AB_x at II

crystals of uniform composition, and to establish the relation of the congruent melting composition to ideal stoichiometry and ultrasonic relaxation phenomena.

If one starts with a pedestal of composition (C) as shown on the ordinate of Figure 32, melting occurs at point L_1. However, solidified crystal forms at composition S_1 as the molten region passes through the rod. Since the solid being formed is richer in component A than is the pedestal being melted, the

liquid is depleted of component A as pedestal growth continues. At some later time the liquid will be at point L_2 and the solid at point S_2, the same composition as the pedestal. This condition will remain stable until the pedestal is exhausted and there is no more pedestal to melt. The very last material to freeze will be at the eutectic; this will be a mixture of the compound at S_f and constituent B at S_f.

A single solidification with the pedestal technique then leads to nonuniform crystals, unless one is using a pedestal of the congruent melting composition. This fact is extremely useful in establishing the congruent melting composition. Comparison of the first material to freeze with later freezing material gives an extremely sensitive test of the departure of the pedestal composition from the congruent melting composition. Metallographic examination of the final solid-ified portion shows unambiguously which eutectic has been reached.

Repetitive zone refining (multiple pedestal growth) produces a crystal of which a part can be very uniform and very nearly the congruent melting com-position. If one begins with a long pedestal of composition Z_1 (Figure 32) and performs multiple zone passes, the liquid composition at the upper end is of composition Z_1, Z_2, Z_3 at the start of the first, second, and third zone passes and the first material to freeze is of compositions ZS_1, ZS_2, and ZS_3. After a large number of zone passes, the upper end of the crystal will be near the congruent melting composition and the lower end will depart radically from this composition. If the crystal is made sufficiently long so that the upper 20 per-cent of the crystal is adequate in length for measurements, then that sample portion can be made very uniform and near the congruent melting composition by multiple pass zone refining. The pedestal apparatus in use is suitable for zone refining; one need only have a pedestal of the order of four to six inches in length.

Crystals of uniform composition other than the congruent melting com-position can be obtained by Czochralski growth of a small crystal from a large volume of melt, or by zone leveling a pedestal which, initially, was nonuni-form in composition.

Other Growth Techniques

Most other growth techniques either are not applicable to YB_{66} growth, because of the reactivity of the melt, or are not advantageous. One additional method is useful: Czochralski growth from a Hukin cold crucible (Ref. 50). This crucible will levitate a large volume of melt, and crystal growth takes place in a symmetric temperature distribution. Such a system should provide long pedestals for zone refining and zone leveling. It has not been used in this work because it requires a large volume of melt to function properly, and such a quantity of melt would have been excessively expensive. The Hukin crucible has not been used previously for materials which must be preheated to initiate coupling, and this function would have to be provided.

Production of Crystals

Crystal growth has been continuously improved by the use of charges of the congruently melting composition and yttrium of higher purity than previously available. The yttrium metal was distilled for use on this project in an ultra-high-vacuum system, by G. W. Demarko, General Electric Neutron Devices Department, through arrangements made with the help of R. L. Hickmott, (Wright-Patterson Air Force Base) and the U. S. Atomic Energy Commission. An analysis of the starting material and the distilled metal is given in Table 10. Vacuum fusion measurements were used for oxygen, nitrogen, and hydrogen. Other impurity concentrations were determined by spark source mass spectroscopy. A list of crystal growth runs is given in Table 11.

Table 10

IMPURITIES IN YTTRIUM METAL

Impurity	Weight Percent Starting Material (ppm)	Weight Percent in Distilled Yttrium (ppm)
C	4	4
O_2	532	174
N_2	46	2
H_2	30	16
Ta	780	47
Cu	550	13
Ni	4	18
Fe	24	12
Cr	5	2
Ti	180	49
Sc	110	$<$7
Ca	7	4
Cl	61	2
Si	27	23
Al	5	$<$3
F	$<$1	$<$1
B	$<$1	$<$1

Table 11

CRYSTAL GROWTH RUNS

Run	Composition B/Y	Apparatus
P_{69}	61.7/1	Cold boat
P_{70}	"	"
P_{71}	"	
P_{72}		Pedestal
$P_{...}$	"	"
P_{74}	"	"
P_{75}	"	Cold boat
$P_{..}$	"	"
$P_{...}$	"	"
$P_{...}$	"	"
$P_{...}$	"	"

The stoichiometric crystals grown from high purity yttrium were used in sound attenuation measurements to establish the diffraction losses and intrinsic losses in YB_{66} (see Section 6).

D. CRYSTAL CHEMISTRY AND INTERSTITIAL METAL ATOMS

There have been several papers in the literature on YB_{66} and related compounds. The data of Spear and Solovyev (Ref. 51) and of Schwetz et al. (Ref. 52) show that all of the rare earths from neodymium to lutetium (except europium) make YB_{66} phases. The larger rare earths (lathanium, cerium, and praseodymium) do not. The work of Carlsson and Lundstrom (Ref. 53) shows that scandium, manganese, iron, and other elements do not. These latter elements can be incorporated into the β-boron structure and cause a lattice expansion, but do not change the crystal structure.

It appears to take a certain minimum size interstitial atom to trigger the crystal structure change from the rhombohedral structure of β-boron to the cubic structure of YB_{66}. This minimum size is somewhere between that of scandium and lutetium, or between 1.63 and 1.72 angstroms. If 1.68 angstroms is taken as the minimum radius, then from Figure 3 of Reference 52 the minimum lattice constant of this phase is 23.370 angstroms. The maximum radius appears to be thorium at 1.81 angstrom, and the maximum lattice constant (Ref. 54) is 23.53 angstroms.

Assuming that all of these cubic crystals have the same number of boron atoms per unit cell of $N_a = 1632$, the average volume per boron atom ranges from 7.821 $(Å)^3$ to 7.983 $(Å)^3$. In β-boron with 105 boron atoms per unit cell, the volumes range (Ref. 53) from 7.814 $(Å)^3$ at pure β-boron to 7.969 $(Å)^3$ at manganese saturated β-boron. Thus the density of packing of boron atoms in the two structures is almost the same, and the ranges of existence are comparable. For comparison, the very dense α-boron phase (Ref. 55) has a volume per boron atom of 7.267 $(Å)^3$, which is noticeably less than for either β-boron or the YB_{66}-type crystals.

Whether a particular metal-boron composition will occur as the β-boron or the cubic YB_{66} structures is determined by the size of the interstitial metal atom. The β-boron range (Ref. 54) is from 1.63 angstrom radius at scandium down to or below 1.24 angstroms at nickel. To obtain the cubic crystal structure for ultrasonic delay line applications, it is necessary to put in the larger metal atoms -- yttrium, thorium, plutonium, or the rare earths.

E. CRYSTAL STOICHIOMETRY

Uniformity of composition and crystal stoichiometry are important in the acoustic applications of the material. The composition of the compound designated YB_{66} has been reported as YB_{100} (Ref. 56), YB_{70} (Ref. 57), and YB_{66} (Ref. 58). The latter results are the most accurate and are the result of an x-ray structure determination. The complexity of the structure and the statistical occupation of a number of the sites precluded an ideal stoichiometry from the structure data, and it was considered to be uncertain to within about 66 ± 2. (Ref. 59).

The specimen studied in the x-ray structure determination was grown by Seybolt (Ref. 56) and formed in a β-boron-YB_{66} eutectic. It must be considered to be rich in boron. The structure suggests that there may be an appreciable solubility of yttrium in the crystal. X-ray lattice parameter measurements showed a range of values from 23.446 ± 0.005 angstroms to 23.482 ± 0.003 angstroms, and the x-ray density (Ref. 58) 2.482 g/cm^3 differed appreciably from a pycnometric density of 2.568 ± 0.005 (Refs. 43 and 60).

The congruent melting point has been located by pedestal crystal growth, precise density comparison, and metallographic examination. (The utility of pedestal growth and metallography is explained above.) Crystals have also been examined by making precise x-ray lattice parameter determinations and analytical wet chemical analysis of composition. Only the density measurements had the requisite precision to lead to the congruent melting composition. Similar experience has been reported by other authors, (Refs. 61-63), who have had to rely upon parameters such as ferroelectric transition temperature, NMR line width, and density, which are very sensitive to small changes in stoichiometry.

A simple density apparatus, shown in Figure 33, was constructed to measure the relative density of samples sectioned from a crystal boule. A constant-temperature water bath was made by fitting a glass tank with an inner glass cylinder such that the areas inside and outside the inner cylinder were equal. With this arrangement a simple magnetic stirring motor and impeller provided rapid water circulation. Temperature control was provided by inserting a thermistor with millidegree sensitivity through the plastic foam top. The bath temperature was maintained constant by a proportional controller which drove a heating element made from a Ni-Cr heater (Amperex Electronic Corporation, Hauppauge, New York) with an Inconel jacket 0.059 inch outside diameter. Temperature was monitored with a mercury-in-glass thermometer calibrated in hundredths of a degree centigrade.

The sample tube was a test tube with a ground, tapered upper end. A tapered glass stopper was fitted to a capillary tube and inserted in the test tube. The test tube was loaded with the samples to be measured, filled with a thallium formate-water solution, and closed with the glass stopper. Density was measured by adjusting the temperature until samples floated at a specific height in the tube. The sample height, temperature, and height of the solution in the capillary were monitored with a cathetometer to eliminate parallax. The volume of the tube and capillary were calibrated by careful weighing and temperature scanning with distilled water.

Absolute densities were determined from the weight of solution added to the tube and capillary and from the observed volume. These values were consistent with those found for the solution density using a pycnometer bottle. Greater accuracy was obtained in the relative density of samples observed during a single run by calculating the density change of the fluid from the column height in the

74
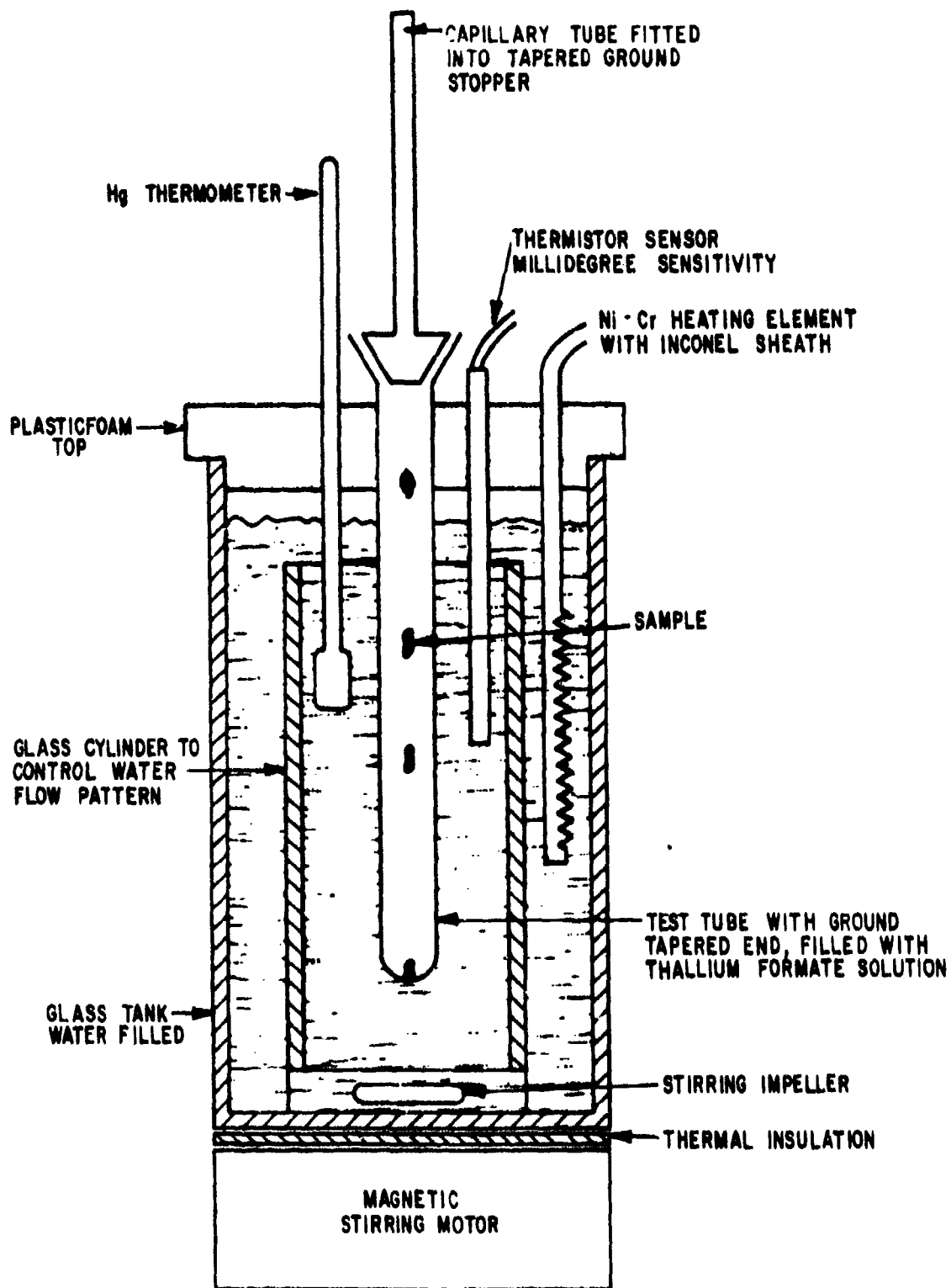
Figure 33. Precision Density Apparatus Schematic Diagram

capillary tube. It was necessary to carefully wet the samples with fluid and to expose them to ultrasonic agitation to ensure that no gas bubbles adhered to them and caused erroneous results. The absolute density values are accurate to approximately 0.2 percent and the relative value to 0.01 percent.

During the course of this study approximately twelve synthesis runs, 29 crystal growth runs, and 128 density determinations have been carried out. Selected data are summarized in Table 12 with x-ray lattice parameters and wet chemical analysis.

Inspection of Table 12 shows that the analytical measurements of composition are too inaccurate to assist in locating the congruent melting composition. There is little correspondence between the chemical formula calculated from these results and the starting composition of the melt used in the initial synthesis of the compound and listed in the first column, "Composition."

Table 12

DENSITY, X-RAY, CHEMICAL ANALYSIS RESULTS

Composition	Density	a_0	Analytical Composition Weight Percent Y and Equivalent Composition
YB_{20}	--	23.482 ± 0.003	--
YB_{40}	--	$23.471 + 0.004$	--
YB_{508}	2.6041	23.455 ± 0.005	--
YB_{50}	2.5782	--	--
YB_{57}	2.5751	$23.443 + 0.004$	--
YB_{56}	2.5776	--	--
YB_{57}	2.5730	$23.451 + 0.005$	--
YB_{60}	2.5706	--	--
YB_{60}	2.5737	--	--
YB_{61}	2.5747	--	--
YB_{61}	2.5712	--	--
$YB_{61.8}$	2.5700	--	--
$YB_{61.87}$	2.5685	$23.445 + 0.005$	--
YB_{62}	2.5664	--	--
YB_{62}	2.5709	23.442 ± 0.005	--
YB_{64}	2.5622	--	--
YB_{64}	2.5699	$23.448 + 0.005$	--
YB_{64910}	2.5676	--	--
YB_{66}	2.5576	$23.443 + 0.005$	--
YB_{67}	2.5686	$23.443 + 0.004$	--
YB_{100}	-	23.440 ± 0.006	--
YB_{66} +	2.5749	--	12.24 ± 0.1 $YB_{66.9}$
YB_{60} +	2.5782	--	12.13 ± 0.1 $YB_{60.}$
YB_{60} +	2.5736	--	12.18 ± 0.1 $YB_{69.3}$

Sample contained second phase YB_{12}.
Sample contained second phase β-boron.
+Two 200-mg samples sectioned along most of the length of the crystal and matched in density.

The densities of these samples correspond satisfactorily with the melt compositions. The x-ray lattice parameters show a definite increase for the samples richest in yttrium. However, the change in lattice parameter from the most boron-rich sample through the congruent melting composition is of the order of or smaller than the standard deviation of the measurements. A factor of six improvement in accuracy of the lattice parameter is required to make it comparable to the density data. Such an improvement would be advantageous in allowing one to assess the relative roles of lattice parameter change and composition change in affecting density.

The density data may be understood more completely by recalling the description of the pedestal growth method (page 69). The first material to freeze is closer to the congruent melting composition than the parent liquid; the composition of the melt during the synthesis process is listed in the first column of Table 12. The pedestal grown crystals were grown from melted pedestal, and that liquid is expected to be somewhat closer to the congruent melting composition than the synthesis melt was, because of segregation.

All of the samples labeled T (Table 12) were sectioned from the very top of the crystals. They are expected to show only a gradual increase in density as the quantity of yttrium in the melt increases and, correspondingly, the amount of yttrium in the crystal is increased. This dependence is shown by the solid circles in Figure 34. The samples labeled B (Table 12) were sectioned from the bottoms of the crystals. The pedestal growth process causes the very bottom of the crystal to reach the eutectic point on the same side of
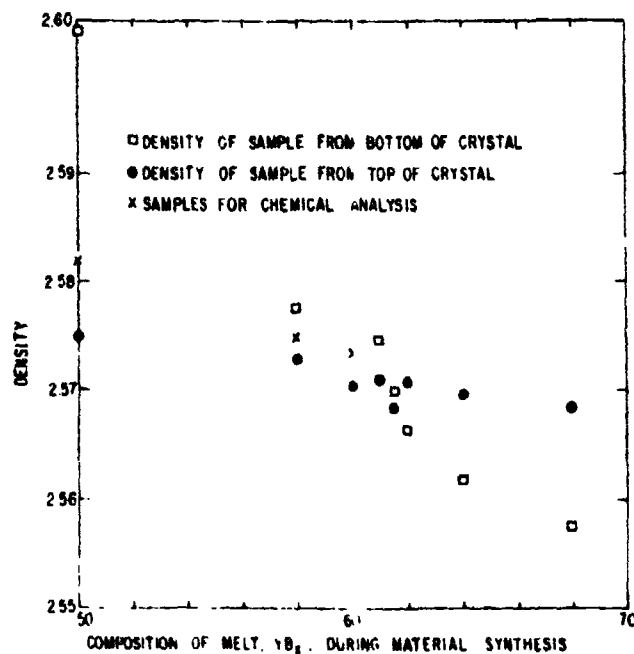
Figure 34. Sample Density Versus Composition of Melt During Synthesis

77

the congruent melting composition as the pedestal composition. If the pedestal
was boron-rich the bottom of the crystal should reach the boron-rich eutectic
and have a low density. If the pedestal was yttrium-rich it should reach the
YB_{12}-YB_{66} eutectic and have a high density. Exactly this behavior is shown
by the open squares in Figure 34. Bottom samples from melts very rich in
yttrium showed a second phase of YB_{12} and bottom samples from melts very
rich in boron showed β-boron as a second phase. Clearly the congruent melting
composition is near but slightly more boron-rich than $YB_{61.8}$.

The congruent melting composition can be estimated more accurately by
plotting symmetrically the bath temperature difference for floating top and
bottom samples versus the composition, as is done in Figure 35. The con-
gruent melting composition is estimated to be $YB_{61.75\pm0.1}$. The remaining un-
certainty in composition will strain the density method and may be influenced
by the segregation of impurities. The most reliable method of producing a
uniform crystal of CM composition is to apply multiple zone refining to a ped-
estal grown from a melt of composition 61.75. A crystal of composition 61.5
was grown with the intent of fabricating an acoustic sample for attenuation
measurement. Subsequent examination showed appreciable mosaic structure
to be present, so that the sample has been used instead for electrical resistivity
measurements.
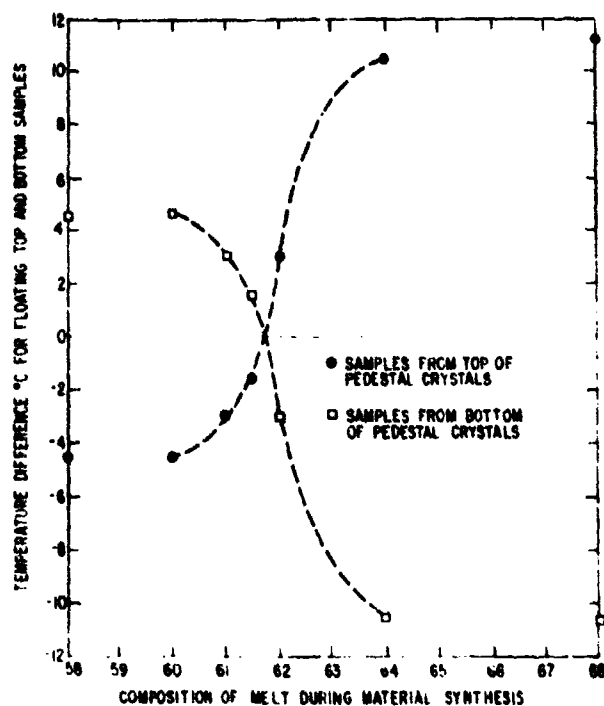
Figure 35. Temperature Difference for Floating Samples from the Top and
Bottom of a Crystal (Plotted Symmetrically) Versus the Com-
position of the Melt During Synthesis

78

Metallographic examination of the yttrium-rich samples initially produced a puzzle. A second phase was observed as expected, but its color (Ref. 45) suggested that it was YB_8 rather than YB_{12} as expected. Because the second phase grains were of micron and submicron size an electron beam microprobe was applied, with the results shown in Table 13. The precipitate is clearly YB_{12} in agreement with the phase diagram, and the subjective color identification was erroneous.

Table 13

ELECTRON BEAM MICROPROBE EXAMINATION
OF YTTRIUM-RICH SECOND PHASE

Ratio Y Counts/B Counts Standard Sample	Ratio Y Counts/B Counts Metallographic Sample
YB_{66} 0.373 ± 0.0045	Matrix 0.320 ± 0.0039
YB_{12} 2.012 ± 0.0205	Precipitate 2.344 ± 0.0248
YB_6 4.274 ± 0.0492	
Yttrium ratio	Counts ratio
66/12 = 5.5	7.4 metallographic sample
	5.4 standard
66/6 = 11	11.4 standard

F. DENSITY AND COMPOSITION – A MODEL

The progress in the growth of single crystals of YB_{66} enables one to draw some conclusions about the crystal structure. The congruent melting composition was found to be YB_n, with n = 61.75. Samples had a density of 2.568 ±0.005 g/cm^3 and an x-ray lattice parameter of a_0 = 23.445 ± 0.005 angstroms. The density can be calculated from

$$\rho = \frac{m_B \cdot N_B + m_Y \cdot N_Y}{(a_0)^3 \, N_A} \qquad (55)$$

where

m_B = atomic mass of boron

m_Y = atomic mass of yttrium

N_B = number of boron atoms in a unit cell

N_Y = number of yttrium atoms in a unit cell

N_A = Avogadros' number

This can be rewritten as

$$\rho = \frac{m_B N_B}{(a_0)^3 N_A} \left[1 + \frac{m_Y N_Y}{m_B N_B} \right] \qquad (56)$$

79

Using $N_B/N_Y = 61.75$ and the measured values of ρ and a_0, the calculated value of N_B is

$$N_B = 1628 \pm 4 \tag{57}$$

This value is higher than that given by Richards and Kasper (Refs. 58 and 59), who postulated

$$N_B = 1584 \pm 48$$

The difference can be explained if it is assumed for the present crystals, which are grown slowly and close to equilibrium conditions, that in a unit cell of volume $(a_0)^3$ there are 8 units of $(B_{12})_{13}$ icosahedra plus 8 units of configuration II in the channels (Ref. 58). These units have 48 boron atoms each. Thus $N_B = 8(156+48) = 1632$. This model avoids the necessity for putting units of both configuration I (with 36 atoms) and configuration II in the channels statistically.

Now the calculated density, with $N_B = 1632$ and $a_0 = 23.445$ angstroms, comes out to be (x-ray) $= 2.575$ g/cm^3, at $n = 61.75$, which is in good agreement with the measured value of 2.569 ± 0.005 g/mm^3. The next step is to compute N_Y:

$$N_Y = \frac{1632}{61.75} = 26.4 \tag{58}$$

Since there are 48 possible yttrium sites per unit cell, then only 55.0 percent of them are occupied at $n = 61.75$. If exactly half of them were occupied, the chemical formula would be YB_{68}. Therefore YB_{68} probably should represent the stoichiometric compound. The congruent melting point at 61.75 is slightly shifted away from this value of n.

If $N_B = 1632$ and the possible range of N_Y is $0 \le N_Y \le 48$, and if the boron lattice parameter is independent of the yttrium concentration in this range, then the range of densities versus N_Y would be

$$\rho = 2.2724 \, [1 + (N_Y/201.7)] \, \text{g/cm}^3 \tag{59}$$

The data on a_0 versus density (see Table 12) show that a_0 is essentially independent of yttrium concentration from densities of 2.558 to 2.575 g/cm^3. This density range converts to a range of $25.3 \le N_Y \le 26.9$ atoms in a unit cell. The model of Richards and Kasper states that the maximum value of N_Y is 24; that is, only 50 percent of the sites are filled. For $N_Y > 24$ the yttrium atoms in adjacent octants may begin to interfere with one another. The interference for $25 \le N_Y \le 27$ is assumed to have only a small effect on a_0 for the present purposes; this is justified in a later section.

The present model of YB_n shows that there is very little disorder in the boron lattice of $N_B = 1632$ atoms per cell. All of the variation seems to lie in N_Y.

The model of Richards and Kasper shows that for each yttrium atom present in a lattice site there is another equally possible vacant site located 2.55 angstroms away along a [100] direction. The Y radius in yttrium metal is 1.78 angstroms, comparable to the value found for Y in YB_{66}. Thus it is not possible for yttrium atoms to occupy both adjacent sites without some considerable local distortion and expansion of the boron lattice. This may be the reason for the increase in a_0 seen for N_Y approaching 48 in Table 12.

The two adjacent yttrium sites are separated by an octagonal ring, or window, of eight boron atoms. The radius of this window is 1.45 angstroms, slightly less than the radius of an yttrium atom (see Figure 36). Under stress,

BORON

$r_B = 0.93 \overset{\circ}{A}$

$r_Y = 1.78 \overset{\circ}{A}$
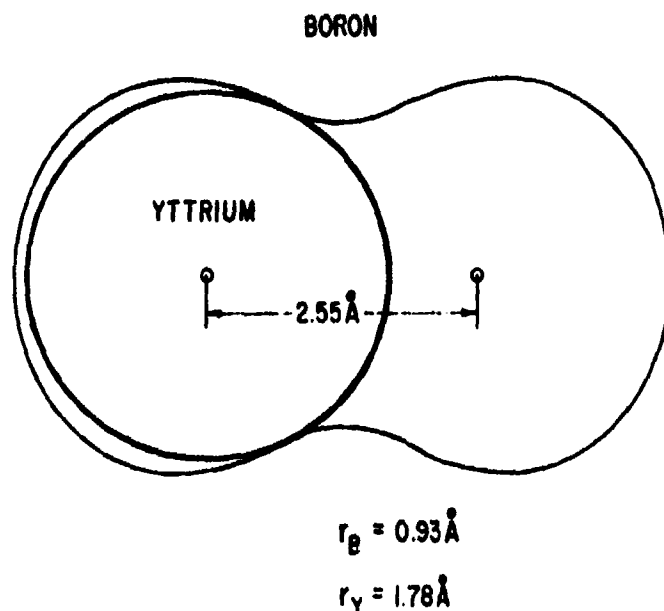
Figure 36. Cavity Occupied by an Yttrium Atom in YB_{66}. The Yttrium is Shown as a Sphere, the Boron as a Solid Mass; the Appropriate Neutral Atomic Radii were Used in this Construction

however, an yttrium atom might well move through this window in the [100] plane into its mirror-image vacant site. Such stress-induced motion may be responsible for some of the acoustic losses reported below.

If, as suggested, the motion of yttrium atoms within the dumbbell-shaped holes in the lattice is responsible for the high acoustic losses, then it might be possible to fill both sides of all of the dumbbells at $N_Y = 48$. The maximum a_0 of the cubic YB_{66} phase occurs (Ref. 54) for thorium where $a_0 = 23.53$ angstroms. The structural study (Ref. 54) of this crystal showed that the largest metal atom that could fit, two at a time into the dumbbell cavity would have a radius of 1.67 angstroms. Thus it might be possible to make $Lu_2B_{66} = LuB_{34}$. If one could choose two atoms where the average radius was 1.67 angstroms,

then a possibility of scandium plus lutetium would do. One might try to grow $ScLuB_{6e}$. In this manner it might be possible to grow a crystal with low acoustic losses. The losses in YB_{68} are too high to be useful.

G. SEGREGATION COEFFICIENT

The authors have shown that YB_n for n = 61.7 is a congruently melting compound with a melting point of about 2100°C. From Figure 32 it can be seen that, for a melt composition where B/Y > 61.7, B will be rejected into the melt from the growing solid crystal. If B/Y < 61.7, then the solid will be richer in boron than the melt. If one defines a segregation coefficient as the ratio

$$k_e = \frac{\text{deviation of boron concentration in solid from n = 61.7}}{\text{deviation of boron concentration in liquid from n = 61.7}}$$

then k_e is approximately 0.3, according to the data of Figures 34 and 37. This value is obtained from the following analysis.

Figure 37. Comparison of the B/Y Ratio in Crystal Boules Grown from the Melt to the Starting Composition of the Ingot. Samples Have Been Taken from Both Top and Bottom of the Boules; Congruent Melting Point is at B/Y = 61.75
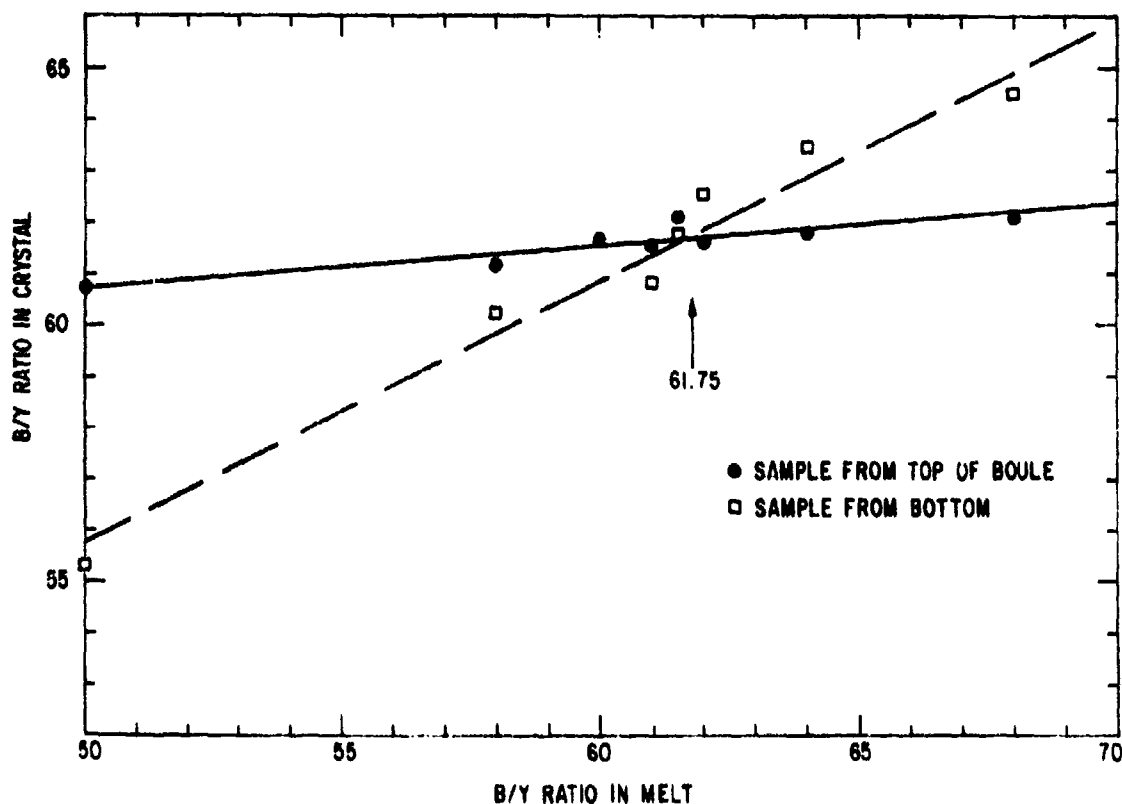
82

Assume that the lattice parameter of YB_n is independent of n near n - 61.7. This assumption is borne out by the data, as discussed previously. Assume that the crystal density variation is only caused by the variation in N_Y (see equation 59). Then the density gives a unique value for the B/Y ratio. Figure 37, which is a replot of Figure 34 using equation 59 to convert density to B/Y ratio, shows the results for crystals that have been regrown twice from melts of the stated composition. The top part of the boule grew first. After two growths the top part of the boule shows a deviation from the congruent melting composition of about 0.08 of that of the melt. For example, a melt of B/Y = 50 produces a crystal with B/Y = 60.7, or a deviation of 1.0 in B/Y. Thus $k^2 = 1.0/(61.7-50.0) = 0.085$. The square on k comes from two successive growth processes from the starting melt composition. Thus, $k \sim 0.3$.

With k this far from unity it was rather difficult to grow large, homogeneous crystals of YB_n at any composition other than n = 61.7. For example, if one desires to grow in a single growth step by a seeded pulling technique (as was used here) a crystal of YB_{48} (with N_Y = 24), the starting melt composition would have to have been about B/Y = 83.

The maximum yttrium concentration in any YB_{66} crystal grown from the melt would correspond (Ref. 43, p. 113) to a $YB_{66}-YB_{12}$ eutectic melt at B/Y = 30. With k = 0.3 the resultant crystal in one growth-step would have B/Y = 52 or N_Y = 31. Here only 65 percent of the yttrium sites would be filled. Testing to see if this predicted value of N_Y = 31 agrees with other experiments one sees from Table 12 that a melt of composition B/Y = 30 would have given a crystal with a_0 = 23.476 angstroms. If it is assumed that a Y_2B_{66} crystal would have a_0 = 23.55 angstroms (slightly larger than ThB_{66}), that YB_{66} has a_0 = 23.445 angstroms, and that a_0 increases linearly with Y content, then from a_0 = 23.476 angstroms one calculates N_Y = 31. The linear increase corresponds to assuming that for YB_n with $34 \leq n \leq 68$ one has

$$a_0 = (23.445 + 4.4 \times 10^{-3} N_Y) \text{ angstroms} \qquad (61)$$

The close agreement at N_Y = 31 is fortuitous, but the model makes some sense. The total length of a dumbbell of two yttrium atoms is 7.12 angstroms. The length of the cavity in ThB_{66} is 6.68 angstroms. Thus the a_0 of Y_2B_{66} should be just slightly greater than that of ThB_{66} at 23.53 angstroms.

H. ELASTIC CONSTANTS

The cubic crystal YB_{66} has three independent elastic constants. These have been measured by the pulse-echo technique. The sound velocity of longitudinal waves in the [100] direction gives $c_{11} = \rho V_l^2$ and the [100] shear wave velocity gives $c_{44} = \rho V_s^2$, where ρ is the crystal density of 2.568 g/cm³. The values of V_L and V_s (Ref. 43, p. 36) are $V_l = (1.21 \pm 0.05) \times 10^6$ cm/sec and $V_s = (0.79 \pm 0.02) \times 10^6$ cm/sec. The longitudinal velocity in a [111] axis rod labeled P-32P, which was 0.27 cm in diameter and 1.27 cm long, was mea-

sured at 60 MHz at 300°K. The velocity was 1.18×10^5 cm/sec. Using the equation 3 $\rho v^2 = c_{11} + 2c_{12} + 4c_{44}$, one calculates that $-0.13 \leq c_{12} \leq +0.85$ in units of 10^{12} dynes/cm².

Thus, for YB_{66}:

$$c_{11} = 3.80 \pm 0.3 \times 10^{12} \text{ dyne/cm}^2$$

$$c_{44} = 1.60 \pm 0.08 \times 10^{12} \text{ dyne/cm}^2$$

$$c_{12} = 0.4 \pm 0.5 \times 10^{12} \text{ dyne/cm}^2 \tag{62}$$

These values give for the elastic anisotropy constant, $A = 2c_{44}/(c_{11}-c_{12})$, a range of $A = 0.96 \pm 0.14$. Thus YB_{66} is nearly isotropic, since A is close to unity. The acoustic diffraction constant, b, (see equation 8), is related to A by

$$b = \frac{4}{3}\left(\frac{1-A}{A}\right) c_{44} \frac{(c_{11} + c_{44})}{c_{11}(c_{11}-c_{44})} = 1.38 \, [A^{-1}-1] \tag{63}$$

Thus the value of b for YB_{66} is

$$b = +0.05 \quad 0.19 \tag{64}$$

This means that the diffraction loss from the acoustic beam in YB_{66} may be small (see Figure 4). A better value of c_{12} is needed in order to calculate b with certainty.

I. DEBYE TEMPERATURE

From the known elastic constants at 0°K one can calculate the Debye temperature at absolute zero. Since the Debye temperature is in the range of 1000°K, the present approximation uses the room-temperature elastic constants. This approximation is supported by the observation that the shear wave velocity, which determines c_{44}, changes very little (Ref. 43, p. 36) between 300°K and 4°K. The calculated Debye temperature is thus

$$\theta_0 = 1300 \pm 50°K \tag{65}$$

Some preliminary specific heat capacity measurements on YB_{66} made at Stanford University (Ref. 64) are in general agreement with this value. Samples of YB_{66} and $YB_{61.7}$ both gave $\theta_0 = 1200°K$.

J. ACOUSTIC ATTENUATION

The only previous data (Ref. 43. p. 37) on the acoustic attenuation in YB_{66} were taken at 1.15 GHz for shear waves in a [100] direction between 2°K and 10°K. The attenuation was found to be quite large; and it was suggested (Ref. 43) that measurements be made at low frequencies. This has now been done, and the data are shown in Figures 38 through 40.
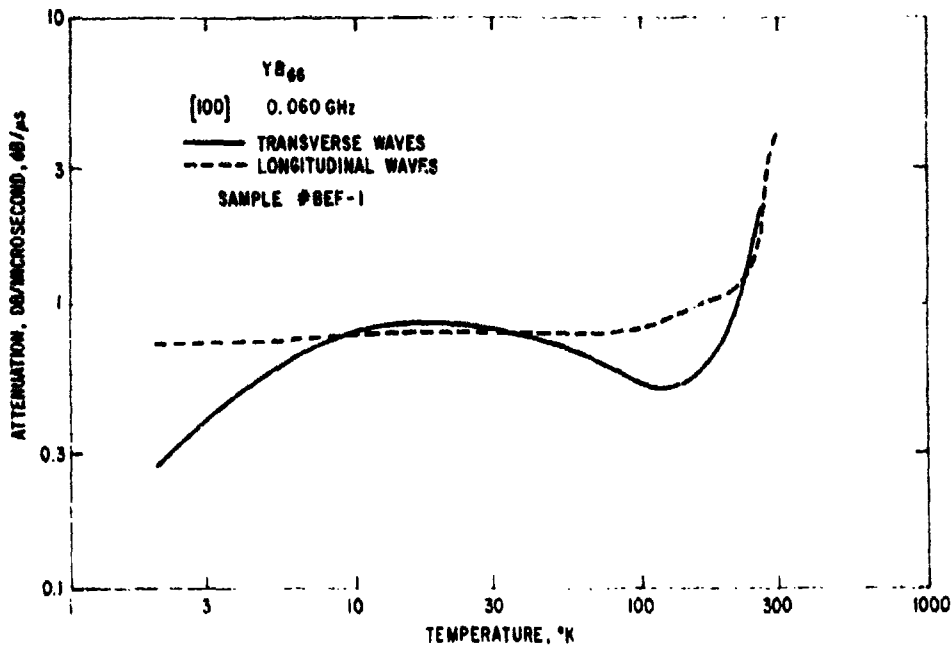
Figure 38. Acoustic Attenuation Versus Temperature at 0.060 GHz for a Melt-Grown Sample of YB_{66}; Direction of Propagation is [100]
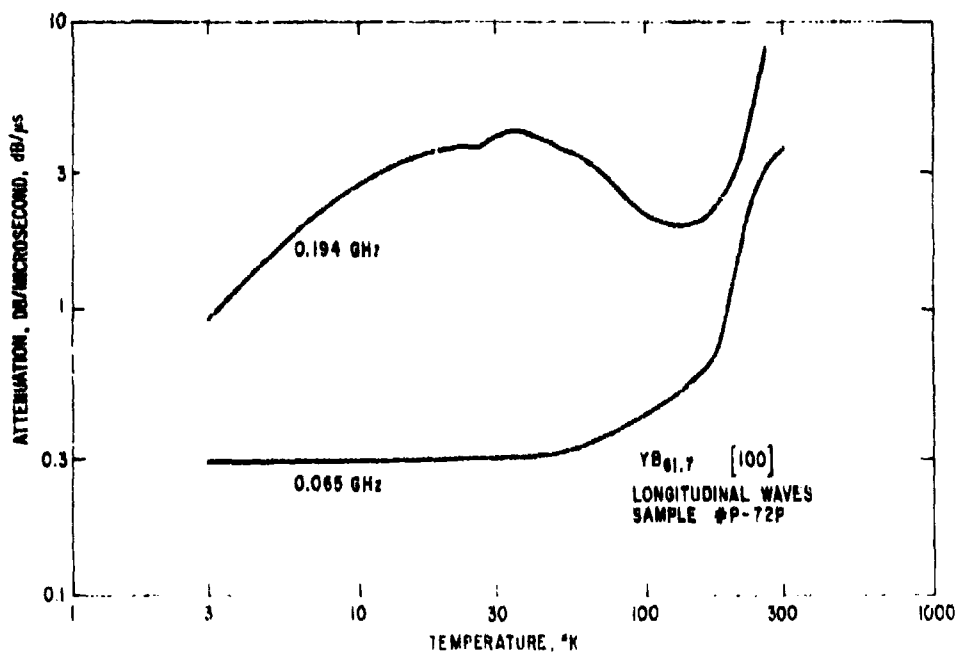
Figure 39. Acoustic Attenuation of Longitudinal Phonons Versus Temperature at 0.065 GHz and at its Third Harmonic for a Melt-Grown Sample of $YB_{61.7}$; Direction of Propagation is [100].
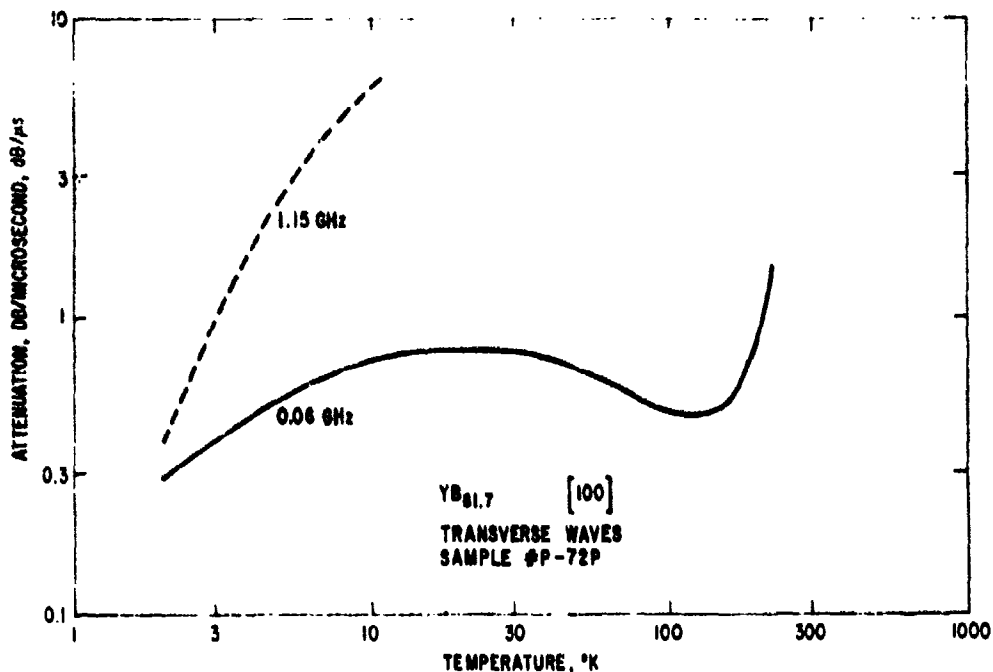
Figure 40. Acoustic Attenuation of Transverse Phonon Versus Temperature at 0.06 GHz in a Melt-Grown Sample of YB$_{61.7}$ (solid curve) and at 1.15 GHz in a Sample of YB$_{66}$ (dashed curve); Direction of Propagation is [100]

Equipment

Sound attenuation measurements using the pulse-echo technique and the exponential comparator have been described in a previous report (Ref. 65). In order to make sound attenuation measurements at lower frequencies and with narrow pulse widths the instrumentation was modified as shown in Figure 41. Narrow pulses were needed because the specimens were short and the acoustic velocities were high. Zero bias into the cascaded ring modulator cuts off the CW signal by approximately 80 decibels. Pulse widths as short as 0.1 μs can be generated by this technique and amplified up to the 10-watt level by the wideband power amplifier. The coaxial sample holder and the receiver part of the instrumentation are the same as were used previously.

The transducers were quartz with overtone-polished, gold plated faces, and their thickness was one-half acoustic wavelength at 65 MHz. Transducers of of X-cut quartz were used for longitudinal waves; AC-cut quartz was used for shear wave generation. Considerable difficulty was experienced in making reliable bonds between the quartz transducer and the boride sample. The bonds needed to operate from room temperature down to 2°K. This bonding problem is probably caused by the large difference in thermal expansion between quartz and the boride samples. Only two bonding materials were found, out of the many materials tried, which, with care, made reliable bonds. These were

86
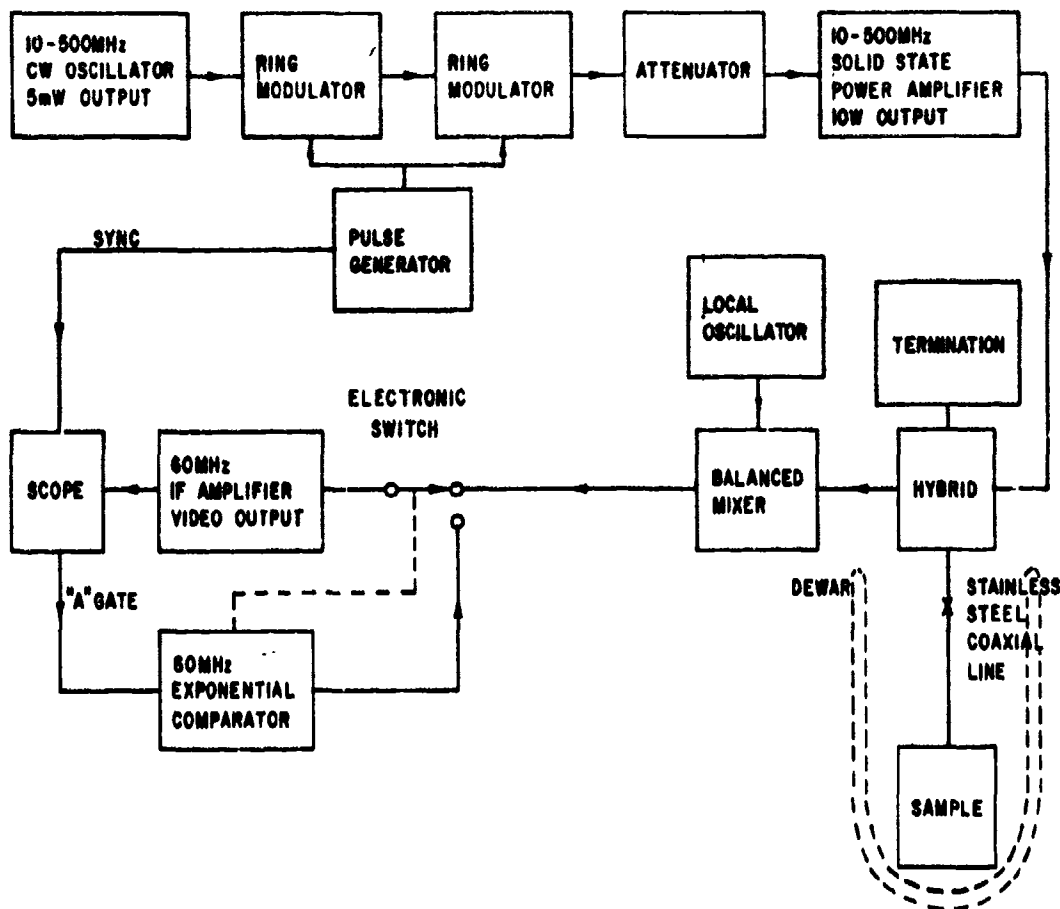
Figure 41. Block Diagram of Instrumentation Used for Low-Frequency
Narrow-Pulse-Width Acoustic Attenuation Measurements

NONAQ Stopcock Grease (Fisher Scientific Company, Fair Lawn, New Jersey)
and 200 silicon fluid (Dow Corning Corporation, Midland, Michigan), with a
viscosity of 20,000 centistokes.

In order to operate at the third harmonic of the quartz transducer it was
necessary to change the resonant circuit and the coupling of the transducer-
coaxial line system. The two methods used are shown in Figure 42. In Fig-
ure 42A the length of the stainless steel coaxial line is greater than 1/4 wave-
length at 65 MHz, so that the entire transmission line can be series-resonated
with variable capacitor C_1 and the coupling controlled by capacitor C_2. This
method worked well when the Arenberg pulse generator was used as a high
power source at 65 MHz. The circuit also resonates at the 3rd, 5th, 7th,
etc. harmonics without retuning, but the losses increase with frequency. In
addition, the 3rd harmonic source, having less output power, produced only
marginally detected echoes.
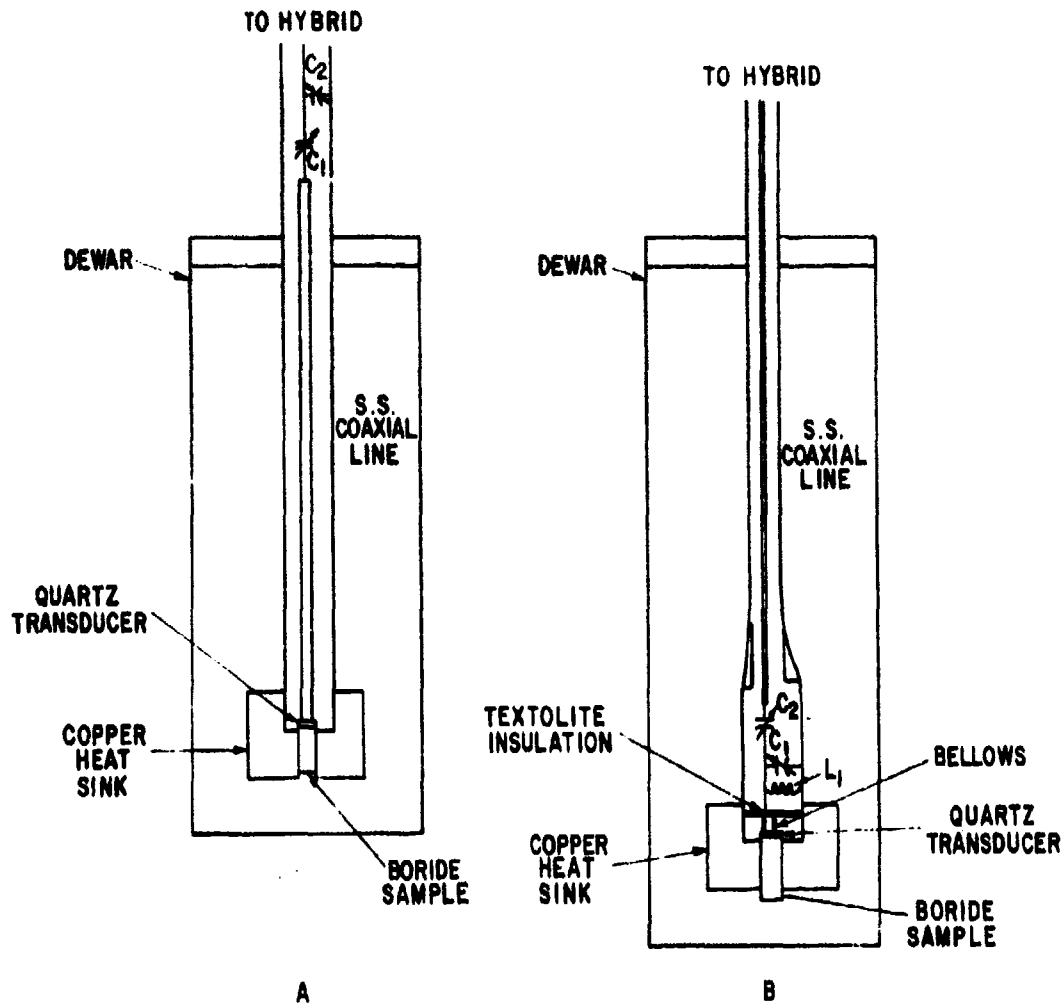
Figure 42. Cross-sectional View of the Two Methods Used to Resonate and Couple the Transducer-Coaxial Line System

Resonating the transducer with L_1 and C_1 and coupling with C_2 as shown in Figure 42B improved the conversion efficiency so that echoes were detected at 195 MHz. The tuning method shown in Figure 42B worked equally well at 65 or 195 MHz; however, it was necessary to change L_1 and C_1 when the frequency was changed. Neither of these tuning methods had the conversion efficiency of the reentrant cavity and ZnO transducer combination previously used at 1 GHz.

Results

The acoustic attenuation results are shown in Figures 38 through 40. The interpretation of these results is, at best, tentative. There are two features, however, which are present for all samples. There is an attenuation peak at

20 to 30°K that covers a large temperature range and rises in magnitude as the frequency increases; above 200°K the attenuation rises rapidly with increasing temperature, with no apparent plateau. It is conjectured that the 25°K peak is caused by some disorder in the lattice, perhaps by yttrium atoms moving between their two possible sites within the dumbbell-shaped cavity under the applied sonic stress. The rise in attenuation at temperatures above 200°K may be the intrinsic Akhieser loss. If so, the loss is much higher than in β-boron at these temperatures, as found by Young, Oliver, and Slack (Ref. 66); however, the temperature dependence is similar.

The comparison of samples of YB_{66} with $YB_{61.7}$ does not show any appreciable difference in acoustic loss. The primary difference in the samples is probably one of homogeneity of composition, the $YB_{61.7}$ samples being better because they were grown at the congruent melting point. However, as indicated in the discussion of the crystal chemistry given earlier in this section, the $YB_{61.7}$ is even further than YB_{66} from the stoichiometric composition of YB_{66}. Neither is very close to the possible low-loss composition at YB_{84} where all the Y lattice sites might be filled.

More work is needed for an understanding of the sources of acoustic loss in YB_{66}. Clearly it is not a good material for delay lines as it is now made. For any immediate applications β-boron or spinel would be better.

K. <u>ELECTRICAL PROPERTIES</u>

Electrical properties of crystal samples can be measured quickly, and they give useful information with regard to impurities and defects. Data for YB_{66} are shown in Figure 43, along with results for β-boron from Deitz and Hermann (Ref. 67) and for α-boron from F. H. Horn (Ref. 68). Four alloy contacts were made to the sample with platinum wires by heating the sample near the Pt-YB_{66} eutectic and then pulsing current through the contacts. The eutectic temperature of approximately 700°C limited the temperature to which measurements could be made.

The temperature dependence of the conductivity shows the material to be a semiconductor. The thermal activation energy calculated from the slope of the ρ versus $1/T$ curve is 0.88 eV. This value does not correlate well with optical transmission which begins near $3000 cm^{-1}$ or 0.36 eV. The resistivity data and the optical data may be controlled by the impurities present rather than the bandgap of the material. All samples were found to be p-type, independent of stoichiometry when tested for polarity of Seebeck EMF. Four point probe measurements of sample resistivity showed nearly identical resistivity at room temperature for all samples. Attempts were made to measure Hall mobility with six contact samples between 300°K and 100°K, but Hall voltages were undetectable. All of these results suggest impurity-dominated conduction and the desirability of preparing samples with impurity concentrations reduced by a factor of ten or more.
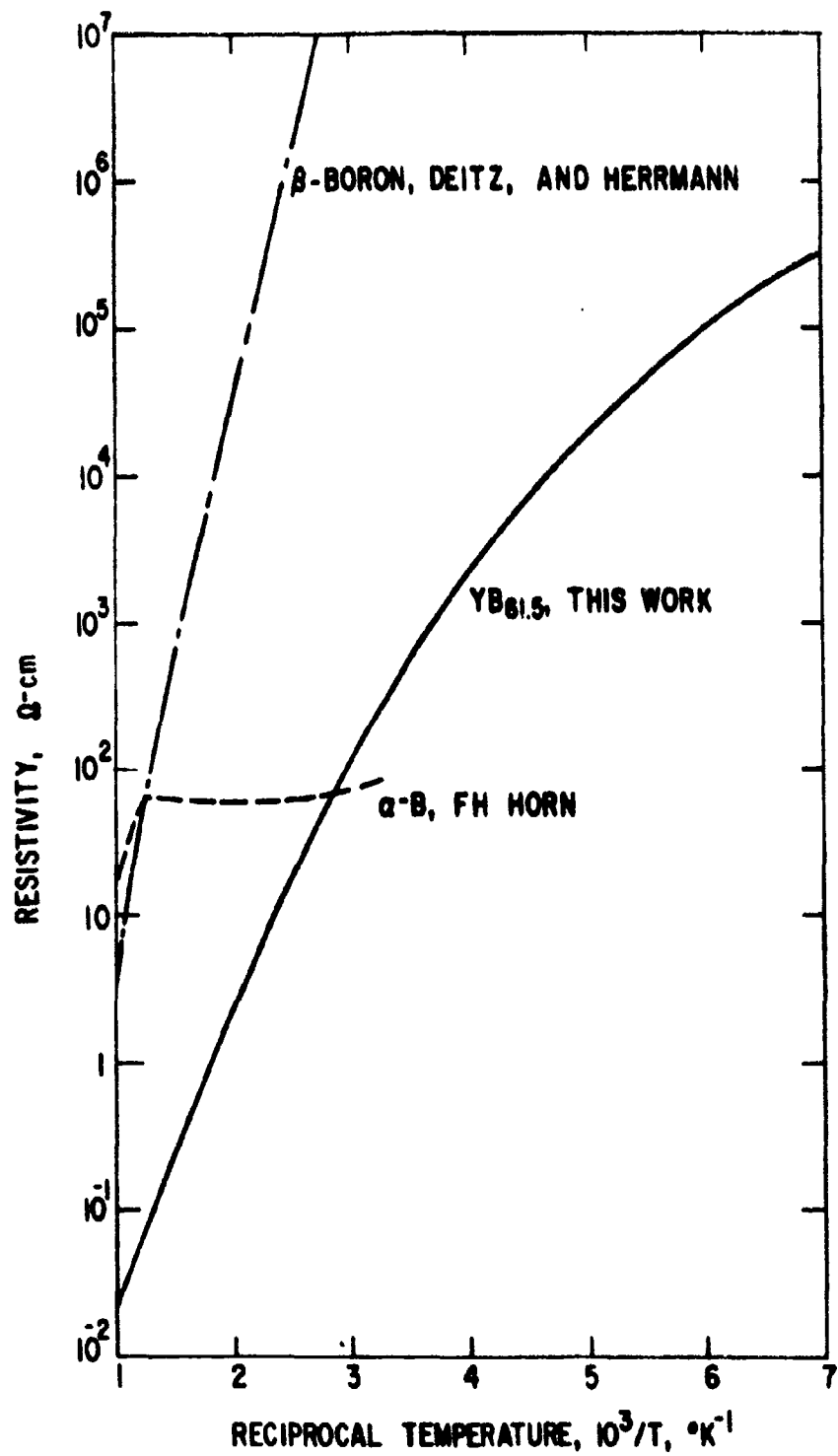
Figure 43. Electrical Resistivity Versus Reciprocal Temperature for $YB_{61.5}$, α-boron, and β-boron

90

L. PURITY

The purity of YB_{66} crystals has been described previously (Refs. 43 and 45), and the yttrium metal used was shown to be the principal source of impurities (see Table 10). Sample purity can be improved by a combination of zone refining and use of higher-purity yttrium metal. The zone refining methods which are desirable for obtaining uniform samples of the congruent melting composition will also remove impurities with segregation coefficients less than unity. Seg-regation coefficients for impurities in YB_{66} are unknown; approximate values will be a byproduct of the crystal growth by zone refining.

The purity of the yttrium metal used is very important. Purification of rare earth metals has been reviewed by Huffine and Williams (Ref. 69). Zone refining of yttrium has little effect on a number of the most prevalent impurities (Ref. 45), including oxygen, nitrogen, copper, nickel, iron, and titanium. Ex-periments in zone refining of YB_{66} will have to be conducted in order to learn whether any of these elements have favorable segregation coefficients in YB_{66}. Three techniques are applicable to the purification of yttrium metal: distillation under high vacuum, filtering through porous tungsten, and electrolysis. The most promising is distillation. Initial attempts to procure distilled yttrium from the metal suppliers proved disappointing; it was less pure (Ref. 45) than vacuum-melted metal. N.H. Parsons (Ref. 70) has reported quite good re-sults in distillation of erbium for the Atomic Energy Commission. Arrange-ments were made through the AEC to have a quantity of yttrium purified by this process and to have an impurity analysis provided of both the starting ma-terial and the distillation product (see Table 10).

Purification by filtering through porous tungsten removes some impurities and contributes others. It could not be intelligently applied to this problem un-til the effects of the other purification procedures are known for a number of impurities. Purification by electrolysis is a potentially valuable purification method and could be applied following distillation, provided the elemental anal-yses of other purification procedures show that it is warranted. As in the other procedures, the impurity segregation achieved (Refs. 69 and 71) is different for each impurity.

Section 5

IRON-DOPED SPINEL CRYSTALS

The possibility of using Fe^{2+} for doping of spinel crystals in order to reduce the acoustic attenuation at 300°K has been explained in a previous report (Ref. 43). One of the previous limitations on this possibility was the fact that only natural spinel crystals containing iron were available, and these crystals contained other, unwanted impurities as well. With the successful growth of spinel by flux techniques (Ref. 72) it has been possible to produce synthetic crystals containing only iron as an impurity. A number of these crystals were made available to us from RCA, through the Wright-Patterson Air Force Base and Mr. Robert Hickmott. Three crystals were selected for optical study, as listed in Table 14.

Table 14

SYNTHETIC IRON-DOPED SPINEL CRYSTALS

Crystal Label	Weight Percent Iron	Sample Thickness (mm)	α, cm^{-1}	Fe^{2+}/Fe_{tot}
RCA 1	0.15*	5.71	4.7	0.28
Novak	0.40**	3.15	8.1	0.18
RCA 5	1.34*	2.34	37.0	0.25

*Iron concentration as stated on crystals as received
**Iron concentration as measured by standard chemical methods

The optical absorption spectra of these crystals were measured over the wavenumber range 500 cm^{-1} < $\bar{\nu}$ ≤ 20,000cm^{-1} at 300°K. The broad absorption band characteristic (Refs. 17 and 18) of Fe^{2+} in tetrahedral sites was clearly seen. This band peaks at $\bar{\nu}$ = 5130 cm^{-1} and extends from about $\bar{\nu}$ = 3000 cm^{-1} to $\bar{\nu}$ = 6000 cm^{-1}. The optical absorption coefficient at the peak is given in column 4 of Table 14. From this value and the assumption that all of the iron in natural spinel sample R97 of Reference 72 occurs as Fe^{2+}, one can calculate the absolute Fe^{2+} concentration in tetrahedral sites in the synthetic spinels. This concentration turns out to be 18 to 28 percent of the total amount of iron in the sample as measured chemically.

The remainder of the iron may be present as metallic inclusions, Fe^{2+} in octahedral sites, or as Fe^{3+}. In view of the lack of control of the partial pressure of oxygen over the flux during growth (Ref. 42), it is not surprising that not all of the iron is Fe^{2+} ions that should be effective in reducing the microwave acoustic losses at 300°K, more control during growth is needed to assure this condition. In view of this problem with the iron content and the small size (0.6 cm maximum) of the crystals, no acoustic attenuation measurements were made on these samples.

Section 6

SOUND ATTENUATION AND DIFFRACTION LOSS

Sound attenuation measurements have been conducted on samples of YB_{66}, $MgAl_2O_4$, and Al_2O_3 from 4°K to 300°K. The thermal phonon losses have been evaluated previously (Ref. 43) for $MgAl_2O_4$, YAG, and Al_2O_3 at frequencies of 500 MHz and above. Similar measurements on YB_{66} at 500 MHz were unsuc-cessful except at very low temperatures (near 4°K). The present attenuation measurements were conducted at low frequency, 60 MHz, using bonded quartz transducers. This report gives experimental values for diffraction losses in all of these materials, so that one is no longer forced to rely on calculation (see Section 2).

The attenuation at 60 MHz for temperatures below about 100°K is dominated by diffraction losses. At higher temperatures, thermal phonon losses (Ref. 43) may enter. For example, in Figure 38, for YB_{66} using longitudinal waves the attenuation below 100°K is constant at 0.79 dB/μs, which is close to the cal-culated loss of 0.75 dB/μs. The very close agreement may be fortuitous in view of the uncertainty in b for YB_{66} (see Equation 64). The results of the com-pleted measurements for $MgAl_2O_4$, Al_2O_3, and YB_{66} are given in Table 15. The agreement between theory and experiment is good.

Table 15

SOUND ATTENUATION AND DIFFRACTION
LOSSES AT 60 MHz

| Sample	Mode	Velocity $\times 10^5$ cm/sec	Anisotropy b	Measured Attenuation (dB/μs)	Calculated Diffraction Loss (dB/μs)
$MgAl_2O_4$	Longitudinal [100]	8.56	-1.1	1.7	1.5
$MgAl_2O_4$ RRE 2	Shear [100]	6.63	+1.5	0.15	0.17
Al_2O_3 A13213	Longitudinal c-axis	11.1	+1.5	0.15	0.31
YB_{66}	Longitudinal [100]	12.2	+0.05	0.79	0.75

Section 7

CONCLUSIONS AND RECOMMENDATIONS

The following conclusions and related recommendations resulted from the studies reported here:

1. Magnesium aluminate spinel is shown to be the best commercially available material for acoustic delay lines, in both attenuation and beam steering characteristics. Substantial improvements in delay line performance can be achieved with spinel and appropriate transducers.

2. Appropriate transducers can be made with bonded quartz, or $LiNbO_3$, or deposited ZnO films. In all cases new electrode metals must be used. Design criteria reported include transducer characteristics, attenuation, diffraction, and beam steering.

3. A method has been developed to calculate the effect of acoustic impedance mismatch between an acoustic delay line and its transducers on the performance of a matched filter processing a stored, coded signal.

4. For long time memory of coded signals, an impedance mismatch greater than a few percent can lead to substantial distortion of the output from a matched filter. With the allowable distortion specified, the required degree of impedance matching can be calculated.

5. The metal system Au-Pd-Ag is identified for bonding transducers to delay lines. Its advantages include: the ability to match impedances, and the reduction of attenuation due to both electrons and dislocations.

6. The efforts on spinel directed toward making a shear wave transducer bond to single crystals at 300 MHz were only partially successful. No fundamental limitations were encountered, but much more work and attention to detail will be needed to perfect the metal-film transducer bonding technique.

7. The work on YB_{66} demonstrated that the anomalous acoustic attenuation in either $YB_{61.7}$ or YB_{66} is quite large at 60 MHz and above. The reasons for this loss are not clear, but one of them may be the presence of the dumbbell-shaped cavities that are present at the lattice sites of the yttrium atoms. These might be filled by using crystals such as LuB_{34}.

Another solution would be the use of pure β-rhombohedral boron, where no interstitial metal atoms are needed to stabilize the structure. Another possibility might be to use crystals of tetragonal boron which are stabilized by carbon or nitrogen atoms. Clearly a lot of work
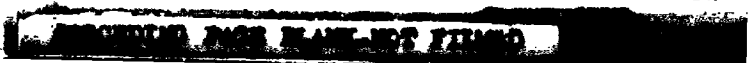
would still be involved to find a material better than spinel for room-temperature microwave acoustic delay lines.

8. Sound attenuation measurements at low temperatures and low frequencies have confirmed the previously calculated values of diffraction loss in $MgAl_2O_4$, Al_2O_3, and YB_{66} crystals.

Section 8

REFERENCES

1. T.M. Reeder and D.K. Winslow, "Characteristics of Microwave Acoustic Transducers for Volume Wave Excitation," IEEE Transactions on Microwave Theory and Techniques, Vol. MTT-17, November 1969, pp. 927-941.

2. J.D. Larson, III, and D.K. Winslow, "Ultrasonically Welded Piezoelectric Transducers," IEEE Transactions on Sonics and Ultrasonics, Vol. SU-18, July 1971, pp. 142-152.

3. J. de Klerk, "Thin-Film Piezoelectric Transducers Used as Generators and Detectors of Microwave Phonons, with Some Attenuation Measurements in SiO_2," Journal of Applied Physics, Vol. 37, November 1966, pp. 4522-4528.

4. H. Seki, A. Granato, and R. Truell, "Diffraction Effects in the Ultrasonic Field of a Piston Source and Their Importance in the Accurate Measurement of Attenuation," Journal of the Acoustical Society of America, Vol. 28, March 1956, pp. 230-238.

5. E.P. Papadakis, "Ultrasonic Diffraction Loss and Phase Change in Anisotropic Materials," Journal of the Acoustical Society of America, Vol. 40, October 1966, pp. 863-876.

6. E.P. Papadakis, "Diffraction of Ultrasound Radiating into an Elastically Anisotropic Medium," Journal of the Acoustical Society of America, Vol. 36, March 1964, pp. 414-422.

7. P.C. Waterman, "Orientation Dependence of Elastic Waves in Single Crystals," Physical Review, Vol. 113, March 1, 1959, pp. 1240-1253.

8. E.K. Sittig, A.W. Warner, and H.D. Cook, "Bonded Piezoelectric Transducers for Frequencies Beyond 100 MHz," Ultrasonics, Vol. 7, April 1969, pp. 108-112.

9. C.E. Cook and M. Bernfeld, Radar Signals, Academic Press, New York, N.Y., 1967.

10. R.S. Berkowitz, editor, Modern Radar, John Wiley and Sons, Inc., New York, N.Y., 1966.

11. P.M. Grant, et al, "Potential Applications of Acoustic Matched Filters to Air-Traffic Control Systems," IEEE Transactions on Microwave Theory and Techniques, Vol. MTT-21, April 1973, pp. 288-300.

12. D.T. Bell, Jr., J.D. Holmes, and R.V. Ridings, "Application of Acoustic Surface-Wave Technology to Spread Spectrum Communications," IEEE Transactions on Microwave Theory and Techniques, Vol. MTT-21, April 1973, pp. 263-271.

13. T.A. Martin, "The IMCON Pulse Compression Filter and Its Applications," IEEE Transactions on Microwave Theory and Techniques, Vol. MTT-21, April 1973, pp. 186-194.

14. F.L.J. Sangster and K. Teer, "Bucket-Brigade Electronics -- New Possibilities for Delay, Time-Axis Conversion, and Scanning," IEEE Journal of Solid State Circuits, Vol. SC-4, June 1969, pp. 131-136.

15. W.S. Boyle and G.E. Smith, "Charge Coupled Semiconductor Devices," Bell System Technical Journal, Vol. 49, April 1970, pp. 587-593.

16. W.E. Engeler, J.J. Tiemann, and R.D. Baertsch, "The Surface-Charge Transistor," IEEE Transactions on Electron Devices, Vol. ED-18, December 1971, pp. 1125-1136.

17. Statement of Work, Wright-Patterson Air Force Base Contract No. F33615-72-C-2203, General Electric Corporate Research and Development, Schenectady, N.Y., 1972. (Final report in progress.)

18. E.K. Sittig, "Effects of Bonding and Electrode Layers on the Transmission Parameters of Piezoelectric Transducers Used in Ultrasonic Digital Delay Lines," IEEE Transactions on Sonics and Ultrasonics, Vol. SU-16, January 1969, pp. 2-10.

19. L.M. Brekhovskikh, Waves in Layered Media, Academic Press, New York, N.Y., 1960.

20. Wm. Feller, An Introduction to Probability Theory and Its Applications, Vol. 1, John Wiley and Sons, Inc., New York, N.Y., 1950, p. 36.

21. Adhesion or Cold Welding of Materials in Space Environments, Special Technical Publication No. 431, American Society for Testing and Materials, Philadelphia, Pa., 1967.

22. A. Maeland and T.B. Flanagan, "Lattice Spacings of Gold-Palladium Alloys," Canadian Journal of Physics, Vol. 42, November 1964, pp. 2364-2366.

23. H. Rohl, "The Elastic Properties of the Solid Solution Series Au-Cu and Au-Pd and the Alloys of Cu_3Pt, Cu_3Pd, and CuPd," Annalen der Physik, Vol. 18, 1933, pp. 155-168.

24. W.P. Mason and A. Rosenberg, "Thermal and Electronic Attenuations and Dislocation Drag in the Hexagonal Crystal Cadmium," Journal of the American Acoustical Society, Vol. 45, February 1969, pp. 470-480.

25. W.P. Mason and A. Rosenberg, " Constants of a Trapped-Energy Electromechanical Transducer Made by Evaporating a Thin Layer of a Piezoelectric Crystal on Each Side of a Quartz Plate," Journal of the Acoustical Society of America, Vol. 46, March 1969, pp. 687-692.

26. W.P. Mason and A. Rosenberg, "Damping of Dislocations in Lead Single Crystals," Journal of Applied Physics, Vol. 38, March 15, 1967, pp. 1929-1936.

27. F.E. Carter, "The Platinum Metals and Their Alloys," Proceedings of the Institute of Metallurgy, Division of American Institute of Mining, Metallurgical, and Petroleum Engineers, Vol. 76, 1928, p. 759; Technical Publication No. 70, 1928, p. 24.

28. L.S. Cain and J.F. Thomas, Jr., "Elastic Constants of α-Phase Cu-Al Alloys," Physical Review B, December 15, 1971, pp. 4245-4255.

29. E.K. Sittig and H.D. Cook, "A Method for Preparing and Bonding Ultrasonic Transducers Used in High-Frequency Digital Delay Lines," Proceedings of the IEEE, Vol. 56, August 1968, pp. 1375-1376.

30. N.S. Shiren, "Ultrasonic Traveling-Wave Parametric Amplification," Procedings of the IEEE, Vol. 53, October 1965, pp. 1540-1546.

31. D. Beecham, "Sputter Machining of Piezoelectric Transducers," Journal of Applied Physics, Vol. 40, October 1969, pp. 4357-4361.

32. G. Wallis and D.I. Pomerantz, "Field Assisted Glass-Metal Sealing," Journal of Applied Physics, Vol. 40, September 1969, pp. 3946-3949.

33. M.P. Borom, "Electron-Microprobe Study of Field-Assisted Bonding of Glasses to Metals," Journal of the American Ceramic Society, Vol. 56, May 1973, pp. 254-257.

34. A. Butts and G.R. VanDuzee, "Cold Welding of Silver," Transactions of the Electrochemical Society, Vol. 74, 1938, pp. 327-339.

35. F. Twyman, Prism and Lens Making, Hilger and Watts., Ltd., London, England, 1943, p. 318.

36. E.H. Jacobsen, "Piezoelectric Production of Microwave Phonons," Physical Review Letters, Vol. 2, March 15, 1959, pp. 249-250.

37. T.O. Woodruff and H. Ehrenreich, "Absorption of Sound In Insulators," Physical Review, Vol. 123, September 1, 1961, pp. 1553-1559.

38. D.W. Oliver and G.A. Slack, "Ultrasonic Attenuation in Insulators at Room Temperature," Journal of Applied Physics, Vol. 37, March 15, 1966, pp. 1542-1548.

39. D.W. Oliver, J.D. Young, G.A. Slack, and F.S. Ham, Paper No. K-4, Ultrasonic Symposium, Cleveland, Ohio October 12-15, IEEE, New York, N.Y.

40. D.W. Oliver and J.D. Young, Microwave Memory Acoustic Crystals, Final Report No. S-68-1053 (AD-832184), Air Force Contract No. F33615-67-C-1399, General Electric Corporate Research and Development, Schenectady, N.Y., 1968.

41. M.F. Lewis and E. Patterson, "Microwave Phonon Attenuation in Magnesium Aluminate Spinel," Journal of Applied Physics, Vol. 39, June 1968, pp. 3420-3425.

42. C.C. Wang and S.H. McFarlane, III, "Growth and Characterization of Large Stoichiometric Magnesium Aluminate Spinel Single Crystals," Journal of Crystal Growth, Vol. 3-4, 1968, pp. 485-489.

43. D.W. Oliver, J.D. Young, and G.A. Slack, Research on Microwave Memory Acoustic Crystals, Final Report, U.S. Air Force Contract No. F33615-69-C-1286, General Electric Corporate Research and Development, Schenectady, New York, June 1971.

44. D.W. Oliver, G.D. Brower, and F.H. Horn, "Cold Metal Crucible System for Synthesis, Zone Refining, and Czochralski Crystal Growth of Refractory metals and Semiconductors," Journal of Crystal Growth, Vol. 12, No. 2, 1972, pp. 125-131.

45. D.W. Oliver and G.D. Brower, "Growth of Single Crystal YB_{68} from the Melt," Journal of Crystal Growth, Vol. 11, No. 3, 1971, pp. 185-190.

46. H.F. Sterling and R.W. Warren, "High-Temperature Melting Without Contamination in Cold Crucibles," Metallurgia, Vol. 67, June 1963, pp. 301-307.

47. T.B. Reed, "Arc Techniques for Materials Research," Materials Research Bulletin, Vol. 2, March 1967, pp. 349-367.

48. W.C. Dash, "Silicon Crystals Free of Dislocations," Journal of Applied Physics, Vol. 29, April 1958, pp. 736-737.

49. W.C. Dash, "Improvements on the Pedestal Method of Growing Silicon and Germanium Crystals," Journal of Applied Physics, Vol. 31, April 1960, pp. 736-737.

50. D. Hukin, unpublished.

51. K.E. Spear and G.I. Solovyev, "High Boron Content Rare-Earth Borides," Fifth Materials Research Symposium, Gaithersburg, Maryland, 1971, National Bureau of Standards, Special Publication No. 364, Government Printing Office, Washington, D.C., 1972, pp. 597-604.

52. K. Schwetz, P. Ettmayer, R. Kieffer, and A. Lipp, " Hectoboride Phases of the Lanthanides and Actinides," Journal of the Less-Common Metals, Vol. 26, No. 1, 1972, pp. 99-104 (in German).

53. J.O. Carlsson and T. Lundstrom, "Solution Hardening of β-Rhombohedral Boron," Journal of the Less-Common Metals, Vol. 22, No. 3, 1970, pp. 317-320.

54. R. Naslain, J. Etourneau, and J.S. Kasper, "α-Phase Crystal Structure of the Boron-Thorium System. New Boron of the YB_{68}-Type Structure," Journal of Solid State Chemistry, Vol. 3, No. 1, 1971, pp. 101-111 (in French).

55. B.F. Decker and J.S. Kasper, "The Crystal Structure of a Simple Rhombohedral Form of Boron," Acta Crystallographica, Vol. 12, 1959, pp. 503-506.

56. A.U. Seybolt, "An Exploration of High Boron Alloys," Transactions of the American Society for Metals, Vol. 52, 1960, pp. 971-989.

57. C.E. Ludin and D. Klodt, unpublished data, quoted by C.E. Ludin, The Rare Earths, (F.H. Spedding and A.H. Daane, eds.) John Wiley & Sons, Inc., New York, N.Y., 1961, pp. 247-248.

58. S.M. Richards and J.S. Kasper, "Crystal Structure of YB_{66}," Acta Crystallographica, Vol. 25, Pt. 2, 1969, pp. 237-251.

59. J.S. Kasper, private communication.

60. G.A. Slack, D.W. Oliver, and F.H. Horn, "Thermal Conductivity of Boron and Some Boron Compounds," Physical Review B, Vol. 4, September 15, 1971, pp. 1714-1720.

61. J.R. Carruthers and M. Grasso, "Phase Equilibria Relations in the Ternary System $BaO-SiO-Nb_2O_5$," Journal of the Electrochemical Society, Vol. 117, November 1970, pp. 1426-1430.

62. G.E. Peterson and J.R. Carruthers, "Niobium-93 NMR as a Sensitive and Accurate Probe of Stoichiometry in Lithium Niobate Crystals," Journal of Solid State Chemistry, Vol. 1, No. 1, 1969, pp. 98-99.

63. R.L. Barns and J.R. Carruthers, "Lithium Tantalate Single-Crystal Stoichiometry," Journal of Applied Crystallography, Vol. 3, Pt. 5, 1970, pp. 395-399.

64. Necmi Bilir, Microwave Laboratory Laboratory, Stanford University, California, private communication of December 19, 1973.

65. D.W. Oliver, G.A. Slack, and J.D. Young, Research on Microwave Memory Acoustic Crystals, Semiannual Technical Management Report No. S-69-1103, U.S. Air Force Contract No. F33615-69-C-1286, General Electric Corporate Research and Development, Schenectady, N.Y., June 1969.

66. J.D. Young, D.W. Oliver, and G.A. Slack, "Temperature and Frequency Dependence of Microwave Elastic Losses in β-Rhombohedral Boron for Longitudinal Waves Along the C Axis," Applied Physics Letters, Vol. 14, May 15, 1969, pp. 301-302.

67. W. Deitz and H. Herrmann, "Conductivity Hall Effect Optical Absorption and Band Gap of Very Pure Boron," Boron: Preparation, Properties and Applications, Vol. 2 (G.K. Gaule, ed.), Plenum Press, New York, N.Y., 1965, p. 107.

68. F.H. Horn, Boron, Synthesis, Structure and Properties (J.A. Kohn, W.F. Nye, and G.K. Gaule, eds.), Plenum Press, New York, N.Y., 1960, p. 70.

69. C.L. Huffine and J.M. Williams, "Refining and Purification of Rare Earth Metals," The Rare Earths (F.H. Spedding and A.H. Daane, eds.), John Wiley and Sons, Inc. New York, N.Y., 1961, p. 145.

70. N.H. Parsons, Production of Bulk Quantities of Ultrapure Erbium, Report No. GEPP-85, Atomic Energy Commission Contract No. AT-(29-2)-656,

General Electric Neutron Devices Department, St. Petersburg, Florida, March 10, 1971.

71. R.M. Al'Tovskii, D.S. Gornyi, A.A. Eremin, and A.S. Panov, Corrosion of Yttrium, AEC-tr-7176, Israel, Israel Program for Scientific Translations, Jerusalem, 1971.

72. G.A. Slack, "FeAl$_2$O$_4$: Growth and Some Thermal, Optical, and Magnetic Properties of Mixed Single Crystals," Physical Review, Vol. 134A, 1964, pp. A1268-A1280.

DISTRIBUTION LIST

	Quantity
Air Force Cambridge Research Laboratory L. G. Hanscom Field Bedford, Massachusetts 01730	
(ATTN: Paul Carr (L7M)	1
Air Force Systems Command (INA) Andrews Air Force Base Washington, D.C. 20331	1
Air University Library Maxwell Air Force Base Alabama 36112	1
Defense Documentation Center Cameron Station Alexandria, Virginia 22314	
(ATTN: DDC-TC)	12
Electronics Warfare Laboratory AMSEL-WL-MA White Sands Missile Range New Mexico 88002	1
Naval Research Laboratory Washington, D.C. 20390	
(ATTN: H. Gurney (Code 5650)	1
Naval Research Laboratory Washington, D.C 20390	
(ATTN: C.R. Kohler (Code 5643)	1
Headquarters, U.S. Air Force Pentagon Washington, D.C.	
(ATTN: AFRDPS-1 Lt-Col T.C. Ferguson	1
Headquarters, U.S. Air Force (SAFRD) Pentagon Washington, D.C.	1

Advisory Group on Electron Devices
201 Varick Street, 9th Floor
New York, N.Y.   10014   1

Aerospace Corporation
Library
P.O. Box 95085
Los Angeles, California   90045   1

Anderson Laboratories, Inc.
1280 Blue Hills Avenue
Bloomfield, Connecticut   06002
                                                           1
(ATTN: M. Kaufman)

Battelle Memorial Institute
505 King Avenue
Columbus, Ohio   43201   1

Datalight, Incorporated
77 Dudleytown Road
Bloomfield, Connecticut   06002
                                                           1
(ATTN: S. March)

David Sarnoff Research Center
Microwave Technology Group
Princeton, New Jersey   08540   1

General Dynamics
Pomona Division, Mail Zone 6-91
Pomona, California   91766
                                                           1
(ATTN: R.J. Sneed)

General Electric Company
Research and Development Center
P.O. Box 8
Schenectady, New York,   12301
                                                           1
(ATTN: J. Eschbach)

General Electric Company
Space Sciences Laboratory
Materials Research and Development Section
Philadelphia, Pennsylvania   19101   1

Honeywell, Incorporated
2314 Stanley Avenue
Dayton, Ohio   45405   1

Hughes Research Laboratories
3011 Malibu Canyon Road
Malibu, California 90265

(ATTN: P. D. Weglein)   1

Isomet Corporation
433 Commercial Avenue
Palisades Park, New Jersey 07650   1

Arthur D. Little, Incorporated
Acorn Park
Cambridge, Massachusetts 02140

(ATTN: W.P. Menashi)   1

Litton Industries
860 Industrial Road
San Carlos, California 94070   1

Litton Industries
Airton Division
200 East Hanover Avenue
Morris Plains, New Jersey 07950   1

Owens-Illinois
Engineering Research
1700 N. Westwood Avenue
Toledo, Ohio 43607   1

Raytheon Company
Research Division Library
Seyon Street
Waltham, Massachusetts 02154   1

Rockwell International
Electronics Group
3370 Miraloma Avenue
Anaheim, California 92803   1

Sanders Associates
Mail Stop 1-6253
95 Canal Street
Nashua, New Hampshire 03060   1

Sperry Rand Research Center
North Road
Sudbury, Massachusetts   01776

(ATTN: R.W. Damon)   1

Stanford Electronics Laboratory
Stanford, California   94305

(ATTN: M. Chodorow)   1

Stanford Research Institute
333 Ravenswood Avenue
Menlo Park, California   94025

(ATTN: A.J. Bahr)   1

Teledyne MEC
3165 Porter Drive
Palo Alto, California   94304

·(ATTN: F.A. Olson)   1

Tyco Laboratories, Bear Hill
16 Hickory Drive
Waltham, Massachusetts   02154

(ATTN: R.L. Bell)   1

University of Connecticut
Department of Physics
Storr, Connecticut   06268

(ATTN: P. Klemens)   1

Watkins-Johnson Company
3333 Hillview Avenue
Stanford Industrial Park
Palo Alto, California   94304   1

Westinghouse Research and Development Center
Beulah Road
Pittsburgh, Pennsylvania   15235

(ATTN: J. De Klerk)   1